TRACER MIGRATION IN CRYSTALLINE ROCK - APPLICATION TO GEOLOGICAL BARRIERS OF NUCLEAR WASTE STORAGE

BY
JUKKA KUVA

Academic Dissertation
for the Degree of
Doctor of Philosophy

*To be presented, by permission of the
Faculty of Mathematics and Natural Sciences
of the University of Jyväskylä,
for public examination in Auditorium FYS-1 of the
University of Jyväskylä on January 20th, 2016
at 12 o'clock noon*

Jyväskylä, Finland
December 2015

Preface

You can do a lot in a lifetime / If you don't burn out too fast / You can make the most of the distance / First you need endurance / First you've got to last

– Neil Peart, *Marathon*

Abstract

This work deals with transport of radionuclides in the geosphere. The subject is investigated through characterisation of water conducting fractures, determining of rock transport properties and development of new methods for characterising geological samples. Here, as is often the case, radionuclide transport is investigated indirectly by characterising the structures, where the transport takes place, and directly by measuring transport properties in the gas phase.

First water conducting fractures of three different types and the rock matrix surrounding them were analysed through rock samples from Olkiluoto. The analysis was done using X-ray tomography, the ^{14}C-PMMA autoradiography technique and petrographical methods. The rock properties around the fractures were found to be highly heterogeneous, but some combining features were found. This experiment also showed the strength of combining different analysis methods.

Second, a method for converting local porosities obtained through the ^{14}C-PMMA autoradiography technique to fracture apertures was developed by analysing the radiation emitted from the ^{14}C-PMMA filled fracture by Monte Carlo simulations and comparing them to fracture apertures. A connection was found and the method was validated by manufacturing artificial glass plate samples with fractures of known apertures, and analysing the autoradiographic images obtained from them. The method needs further development before it can be used on real rock samples, but it was shown to be extremely promising in the studies conducted.

Last, the transport properties of Olkiluoto rock samples were measured directly using argon pycnometry and through diffusion, permeability and advection - matrix diffusion measurements in the gas phase. The gas phase methods exclude sorption and other chemical and water-based processes and thus only give information about diffusion. They are, however, over 10 000 times faster, making them excellent for planning of water phase experiments and giving preliminary results. Gas phase methods are also very powerful tools when investigating the long term transport behaviour, as it would take far too long to run water phase experiments to the late part of the breakthrough curves. Correlations between porosity, diffusion coefficient and permeability were investigated and found to exist only between the latter two parameters. The mathematical model and measurement setup for advection - matrix diffusion measurements were vastly improved during these studies and are now effective tools for such a measurement.

Overall this work managed to produce usable parameters for the safety assessment of the upcoming nuclear repository. The methods used were found to be suitable for the experiments, and they were developed further during the experiments.

Author   Jukka Kuva
Department of Physics
University of Jyväskylä
Finland

Supervisors   Doctor Mikko Voutilainen
Department of Chemistry
University of Helsinki
Finland

Professor Jussi Timonen
Department of Physics
University of Jyväskylä
Finland

Reviewers   Doctor Yukio Tachi
Japan Atomic Energy Agency
Japan

Professor Jyrki Räisänen
Department of Physics
University of Helsinki
Finland

Opponent   Professor Vladimir Cvetkovic
Land and Water Resources Engineering
KTH Royal Institute of Technology
Sweden

List of Publications

I Kuva, J., Siitari-Kauppi, M., Lindberg, A., Aaltonen, I., Turpeinen, T., Myllys, M. and Timonen, J.: *Microstructure, porosity and mineralogy around fractures in Olkiluoto bedrock*, Engineering Geology **139-140**, 28-37 (2012)

II Sardini, P., Kuva, J., Siitari-Kauppi, M., Hellmuth, K.-H.: *A simplified simulation approach for estimating crack aperture using ^{14}C-PMMA method*, Journal of Coupled Systems and Multiscale Dynamics **2(4)**, 244-255 (2014)

III Kuva, J., Voutilainen, M., Kekäläinen, P., Siitari-Kauppi, M., Timonen, J. and Koskinen, L.: *Gas phase measurements of porosity, diffusion coefficient and permeability in rock samples from Olkiluoto bedrock, Finland*, Transport in Porous Media **107(1)**, 187-204 (2015)

IV Kuva, J., Hellmuth, K.-H., Sardini, P., Siitari-Kauppi, M.: *Verification of a simulation approach for estimating crack aperture using ^{14}C-PMMA method*, Journal of Coupled Systems and Multiscale Dynamics **3(4)**, (2015)

V Kuva, J., Voutilainen, M., Kekäläinen, P., Siitari-Kauppi, M., Sammaljärvi, J., Timonen, J. and Koskinen, L.: *Gas phase measurements of matrix diffusion in rock samples from Olkiluoto bedrock, Finland*, submitted for publication (2015)

The author performed the tomographic imaging and the related analysis for the article I. He also participated in the analysis of the autoradiographic data and polarized microscopy and wrote the first draft of the article.

The author performed some of the Monte Carlo simulations and actively participated in the development of the related analysis method for articles II and IV. He conducted the experiments and related analysis in the method validation and wrote the final draft of article II and both first and final drafts of article IV.

The author performed all the gas phase measurements for articles III and V and participated in the analysis of the results. He wrote the first drafts for both articles.

Contents

1 Introduction

Nuclear power has been in use for a long enough time that dealing with the waste it produces is becoming a current issue in many countries. In many countries the repositories are already being built or at least actively planned [1–3]. While some countries have decided to deposit their high level waste in clay [4], Finland and Sweden among others have chosen crystalline rock as the host medium for the repository [5–8]. The used nuclear fuel will be vitrified and protected by several protective layers, but as the timescales required for deposition are hundreds of thousands of years, the possibility that the barriers break down has to be taken into account. Because the amount of final deposition canisters will be in the thousands, the possibility of a manufacturing defect needs to be taken into account too [9]. Both aforementioned cases may cause release of radionuclides from the repository, and it is vital to estimate how fast and far they will migrate in the geosphere and what kind of effects will they have in the biosphere. The long time scale means at least one glaciation has to be taken into account [10], making the safety assessment even more complicated [11–13]. One studied scenario includes glacial water flooding the repository and changing its chemical conditions [9].

The most important migration pathways for radionuclides in the geosphere are water conducting fractures which facilitate fast transport in the bedrock, and the surrounding rock matrix, which retards this transport. To model the migration in the fracture network, lots of knowledge about fractures and the surrounding rock is needed. One important, yet often overlooked characteristic is the aperture distribution of the fractures. It can be used, in connection with several other pore network properties (connectivity, tortuosity, constrictivity, etc.) to study rock permeability and other transport properties [14–16] as well as rock alteration and soil formation [17].As fracture apertures in rock commonly range from less than 100 nm to hundreds of μm [18], finding a suitable method which has a good enough resolution and can be used on a wide range of scales is not easy. Confocal laser microscopy can be used to investigate fracture networks, even in 3-d [19], but the field of view is quite small (often a few hundreds of μm). Scanning electron microscopy is also a flexible tool, but because of its limited field of view it is not suitable for larger samples [20]. Computed X-ray tomography [21, 22] can be used to obtain 3-d maps of the pore network, even for large samples, but the resolution of the method is not sufficient for smaller fractures, especially in large samples [23, 24]. It is thus often necessary to use several methods to get knowledge in all required scales.

One possible solution to this problem is the ^{14}C-PMMA autoradiography technique [25–28], which can quickly and easily produce 2-d porosity maps of hand scale samples. Although the resolution of the method is only about 20 μm [29], the method offers information from pores of even nanometer scale [30] and a promising method has been developed to transform porosities obtained by the ^{14}C-PMMA autoradiography technique into fracture apertures, as shown in the articles of Appendices II and IV. The method itself involves impregnation of sample pore space with a radioactive monomer which is then polymerised, and the sample is then exposed to an autoradiographic film along with standards of known activities. The resulting gray-scale image can thus be converted into a local porosity map.

In a broader sense, from e.g. a modelling perspective, characterising the fractures near a repository would be extremely useful. In the Olkiluoto area the fractures can be roughly divided into three

categories: calcite filled fractures, clay filled fractures and slickensided fractures [31]. These fractures are, or used to be, water conducting and characterising the rock matrix around the fractures can give valuable information about the phenomena happening in them, such as rock alteration. As shown in the article in Appendix I, the rock around water conducting fractures has been characterised with several methods, such as computed X-ray tomography and the ^{14}C-PMMA autoradiography technique. When average parameters around each fracture type are determined, the models evaluating the repository safety [32] can be improved. This has been done in the current safety assessment for the repository [9], which uses parameters determined in this work when modelling the transport of a radionuclide release in the fractures.

X-ray tomography [33], which was invented already in the 1930s [34] and computerised in the early 1970s [35] was first used for medical imaging [36, 37], but has since been widely used to study geological materials [38–40]. Use of tomography for geological materials has led to applications in several fields of science [39, 41–51]. The method involves taking several X-ray images of a sample from different angles, which can then be reconstructed into a 3-d image of the sample using a modified form of the inverse Radon transform [52]. Recently these reconstructions have become so accurate that they have been used to determine material parameters, such as porosity, pore size distribution, grain size distribution, specific surface area, connectivity and tortuosity [53–57]. These parameters characterise the structure and transport properties of porous materials, but unfortunately the resolution of the method is not good enough for a detailed analysis of submicrometer features of centimeter scale geological samples. X-ray tomography can however be combined with complementary methods, such as the ^{14}C-PMMA autoradiography technique, to achieve unique information about properties of geological samples [58, 59].

Naturally the most basic transport properties, porosity, diffusion coefficient and permeability, can be measured directly with controlled laboratory measurements. This can be done in the gas phase [60–64], where the measurements are fast but chemistry and water based interactions are ignored, or in the water phase [65–68], where the measurements take much longer, but give results which are more accurate considering the final repository. The water phase measurements can be conducted faster if an electric field is used, which also gives information about formation factor [69]. Gas phase measurements are not only faster, but also often easier to analyse accurately and can be easily reproduced. They also give information about the long term transport behaviour which is not feasible to obtain with water phase measurements. A correlation between the basic transport properties would be useful, as it could remove the need for some time consuming measurements. The correlation between porosity and diffusion coefficient [70–73] and between diffusion coefficient and permeability [57, 63, 74, 75] has been studied and it has been found, but these correlations have been strongly material and case dependent and a general correlation is yet to be found.

Results and parameters even more relevant to the safety case can be obtained through experiments which simulate flow of radionuclides in a water conducting fracture, so called advection - matrix diffusion experiments, where advective tracer flow in a flow channel is retarded by diffusion of the tracer into the surrounding rock matrix. This differs from through diffusion experiments, where the tracer diffuses through a sample and its breakthrough curve is measured. It would be most advantageous to do these measurements in situ, especially as it has been shown that porosity, diffusion coefficient and sorption coefficient can differ greatly in laboratory and in situ measurements [76–79]. Some in situ matrix diffusion experiments are indeed being conducted [80, 81] in the REPRO (rock matrix Retention PROperties) project niche [82] in ONKALO, Olkiluoto, a research facility in the tunnel leading to the future Finnish final repository. These measurements are however expensive and time consuming, and therefore similar measurements have been done in laboratory in the gas [61, 62, 64] as well as water [65, 83, 84] phase. Matrix diffusion measurements in natural fractures have also been conducted [85, 86]. Matrix diffusion experiments require complex mathematical models to interpret them [87–89], and can also be simulated with methods like finite difference [90], lattice

Boltzmann [91] and Monte Carlo [92]. All of these experiments can be used to aid and complement the important in situ measurements. This kind of experiments also serve to increase the knowledge of radionuclide transport in fractures and the retarding effect of matrix diffusion, and thus help to improve the safety analysis of the spent nuclear fuel repository.

The main objective of this Thesis was to better the understanding of radionuclide transport in the geosphere, to develop new methods for characterisation of geological samples and to produce usable results and parameters for the safety assessment of the final repository for nuclear waste. To this end: 1. Rock samples from Olkiluoto containing water conducting fractures of three different types were analysed via X-ray tomography, the ^{14}C-PMMA autoradiography technique and polarised microscopy to find common characteristics for the fracture types. 2. A method to convert local porosities obtained by the ^{14}C-PMMA autoradiography technique into fracture apertures was developed and verified via artificial samples with fractures of known apertures. 3. Porosity, through diffusion and permeability measurements were conducted in the gas phase for several rock samples from Olkiluoto to produce transport modelling parameters, and the results were combined with previously measured transport property data to look for a correlation between the properties. 4. Advection - matrix diffusion measurements were conducted in the gas phase for long rock samples from Olkiluoto to aid the in situ measurements and to develop and verify the mathematical models currently being used to interpret such measurements.

2 Final disposal of spent nuclear fuel

Nuclear power produces a fairly low amount of waste in comparison with other large-scale forms of energy production, and the produced waste is relatively easy to handle. It is however very long lived and needs to be dealt with accordingly. When the nuclear fuel is no longer usable in a general modern reactor, it still has lots of capacity left, so it can be either reprocessed and used to produce further energy or deposited until it is harmless [93]. Geological deposition in a deep bedrock was already brought up in the 1950s [94], and Finland has also decided to deposit the nuclear waste from nuclear reactors of Fortum and TVO (Teollisuuden Voima Oy) deep in the crystalline bedrock [8, 9]. Finland is a pioneer in this field and the repository will in all probability be the first in the world when it starts operation. The repository will be located in the Olkiluoto area close to two currently operating nuclear power plants, about 400 m underground. The repository will be based on the Swedish KBS-3 (KärnBränsleSäkerhet, nuclear fuel safety) multi-barrier design [95] and has two main functions. It should provide a stable environment for the waste canisters and limit radionuclide release rate in case of a leaking waste canister. Performance of a final repository system suitable for granitic crystalline rock has been studied already for a few decades [95–104]. Similar systems have been studied in Sweden [95, 100, 102], Switzerland [103], France [99], Canada [101], Japan [104], USA [105] and Germany [106].

The KBS-3 multi-barrier system, shown in fig. 2.1 is based on four separate barriers: the canister, the bentonite buffer, the bentonite backfill and the surrounding bedrock. The repository is designed to contain the nuclear waste in the waste canisters for hundreds of thousands of years and limit radionuclide release rates in case of a leak [98].

The **canisters** are based on an inner cast iron insert, which will provide mechanical stability against movement of the surrounding bedrock, and an outer copper layer, which will provide resistance against corrosion. Under the expected evolution of conditions in the repository, the canister should remain intact for at least 100 000 years [107–109]. There have been claims of much quicker corrosion [110], but these results are considered controversial [111]. The canisters are likely to be deposited in vertical holes in the repository tunnels and each canister will contain about 2 tons of high level nuclear waste. In the present plans there will be about 4500 of these canisters in the Olkiluoto repository. The fuel is vitrified inside the canister, meaning that even if the canister is filled with water, only part of the radionuclide inventory is released instantly, and the rest is released through degradation of the fuel matrix and metal parts [112, 113].

The canisters will be surrounded by a **buffer** made of bentonite, a clay that swells when it gets in contact with water. The bentonite buffer protects the canister from minor rock movements and prevents a groundwater flow in the immediate vicinity of the canister. The hydraulic conductivity of bentonite has been shown to be very low (less than 10^{-13} m/s) [114–116], which ensures that radionuclide transport near the canister can only happen by diffusion. The buffer completely surrounds the canister in the deposition hole, effectively isolating it from the bedrock.

The deposition tunnels will be filled with a **backfill** consisting of bentonite and crushed rock. This is done to prevent a considerable groundwater flow in the tunnels and to ensure the bentonite buffer stays in the deposition hole [117]. The hydraulic conductivity of the backfill depends on the bentonite
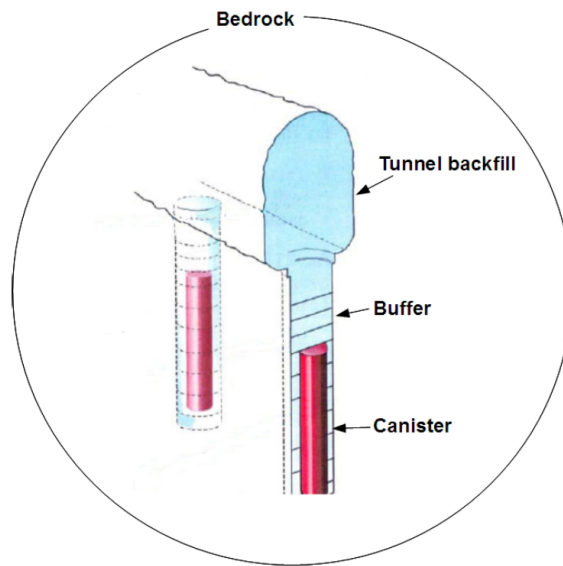
Figure 2.1: The transport barriers of the KBS-3 disposal concept. The canister contains the waste and provides a shelter for mechanical stress and corrosion. The buffer protects the canister and along with the backfill prevents any leaked radionuclides from reaching the bedrock, which in turn retards the radionuclides before they reach the biosphere. [32]

content, but the repository design is based on a hydraulic conductivity of 10^{-10} m/s under the expected conditions [118]. The backfill also provides mechanical stability for the deposition tunnels.

The **crystalline bedrock** provides suitable and predictable conditions for the repository and acts as the final barrier against radionuclide transport to the biosphere. The bedrock has a block structure, which dissipates stress along the fracture zones and the rock between fracture zones is geologically stable [119]. Even major hydraulic disturbances on the surface caused by the glacial cycle should be strongly attenuated inside the rock mass surrounded by the major fracture zones [120]. The groundwater from the repository depth has also been investigated and the geochemistry indicates slow movement and exchange of solutes of the groundwater [119, 121]. The bedrock should thus be able to limit both the inflow of harmful substances and the outflow of radionuclides from a possible leak. The main retarding factors of the bedrock are matrix diffusion of radionuclides from a water flowing fracture to the stagnant water in the rock matrix pores and sorption to the mineral surfaces. Uranium has a very low solubility in the predicted chemical conditions of the repository, which also acts as a retarding factor. The properties of the bedrock will be looked at more closely in the rest of this Thesis.

Several **performance assessments** [9, 96–98] have been done of the Finnish repository, which have to consider time scales of hundreds of thousands of years and several release scenarios and paths. One key scenario in the assessments is a defective waste canister leaking radionuclides to the groundwater. Canister may be initially defective because of a manufacturing error and corrosion creates a small hole, through which the release of radionuclides can take place. This would not be a problem in itself, as diffusion through the bentonite buffer and the crystalline bedrock is slow enough that both can be considered almost impermeable [122–124], making the transport directly through the bentonite buffer and the background rock extremely slow and negligible considering the safety assessment. The conservative safety case thus presumes that there is a water flowing fracture that

intersects the deposition hole at the location of the hole in the canister, providing a more effective transfer route. In this scenario the peak release rate was calculated to be few tens of kBq annually [9]. Another important scenario is glacial water flooding the repository tunnels in the melting period of a glaciation. This could change the chemical conditions in the repository and affect both the bentonite buffer and the vitrified nuclear waste. This work will now concentrate on acquiring parameters for safety analyses such as the ones described above.

3   Rock structure characterisation methods

Fractures and other rock features are often quite small, upwards from tens of nm, but the length scales in the safety assessment of a spent nuclear fuel repository can be from meters to kilometers. This scale difference means that several different techniques and methods need to be combined to get accurate results. This chapter will review two important methods used in this work that can complement each other, the ^{14}C-PMMA autoradiography technique and computed X-ray tomography. The ^{14}C-PMMA autoradiography technique was used in the articles found in Appendices I, II, IV and V and computed X-ray tomography was used in the article found in Appendix I.

3.1   The ^{14}C-PMMA autoradiography technique

The ^{14}C-PMMA autoradiography technique is used to acquire 2-d porosity distributions of connected pores in centimeter-scale rock samples. The investigated sample is impregnated in vacuum with ^{14}C labeled methylmethacrylate (MMA), a low atomic weight, low viscosity monomer that can effectively infiltrate the connected porosity of the sample. Heat or radiation is then used to polymerise the MMA into polymethylmethacrylate (PMMA). Autoradiography, film or digital, can then be used to track local activities, which can be converted to optical densities and further into local porosities through various image-processing techniques.

To ensure proper MMA infiltration during impregnation, the samples are first dried, usually to a constant weight, by a combination of a coarse vacuum and temperature ranging from 50 °C to 120 °C. This is done to remove water from the pores and can take from a few days to a few months depending on the sample. For impregnation the sample needs to be in a vacuum chamber, often the same in which it was dried. The chamber is first filled with gaseous ^{14}C-MMA and then with it in liquid form. The pores are infiltrated through capillary forces, first the largest and then the smallest pores. Many factors, such as sample size, total porosity, pore connectivity, pore tortuosity and constrictivity, affect the impregnation time required to fill most pores. The impregnation time typically varies from a few days to a month. [25–28]

In order to polymerise the MMA (into PMMA) and thus render it solid and immobile within the pore matrix, gamma radiation can be used. A dose of 50–80 kGy is typically enough for centimetre-scale rock samples, but 100 kGy is needed for clays [29]. Polymerisation using heating and/or a chemical initiator is also increasingly common, as it eliminates the need for a strong gamma source [125–127]. If the sample is transparent, polymerisation by UV-light is also possible [128].

When the pore space of the sample is full of ^{14}C-PMMA, the β-particles emitted by ^{14}C are detected with autoradiography. Before imaging the sample is cut and the investigated surface is polished to ensure a tight contact between the sample and the film. The polished surface is then placed on an autoradiographic X-ray film when using the film autoradiography or a phosphor plate when using

the digital autoradiography. In this work only the film autoradiography was used.

In the film autoradiography the sample is placed on a film which contains silver halogenide crystals. When β-radiation hits such a crystal, it causes silver ions to reduce into metallic silver aggregates on the film, which show as dark spots. The more ^{14}C-PMMA a region of the sample contains, the darker the corresponding area on the film appears. As the radiation comes only from the pore network of the sample, the blackening of the film is proportional to local porosity. A typical resolution for the film autoradiography is around 20 μm, caused by the range of β particles in the film [29]. The autoradiographs are digitised using a table scanner or a CCD camera. The resolution used here finally determines the resolution of the digital autoradiographic image, but can not be better than the 20 μm mentioned.

In the digital autoradiography the sample is placed on a phosphor plate, which contains a photo-stimulable phosphor layer with BaFBr:Eu^{2+} crystals between an (optional) protective layer and a plastic support layer. β-radiation can then excite the ground state Eu^{2+} to a metastable Eu^{3+} state. When the phosphor plate is scanned, it is exposed to red laser light, which converts the Eu^{3+} state back to the Eu^{2+} ground state and releases a 390 nm blue light photon, which is then detected with a photomultiplier tube [129]. The resolution used in this process determines the final resolution of the digital autoradiograph, which at its best can be close to that of film autoradiography [16]. While the resolution of digital autoradiography is often slightly worse than that of the film autoradiography, it has many advantages such as reusability of the phosphor plates (Eu^{2+} excitation is reversible), better linearity and better sensitivity, which allows for shorter exposure times [16].

Now the mathematical basis for converting the film blackening seen in the digital autoradiographs into local activities and eventually porosities is explained [25, 29]. If the pore sizes are small relative to the range of β-absorption, or at least well below the used pixel size, the dilution assumption is valid, meaning that the tracer is virtually diluted by the rock matrix as most of the β-radiation has been attenuated in the matrix on its way to the film. This makes the porosity determination more reliable. Wide fractures which are near or over the used pixel size are usually excluded from the quantitative porosity determination to decrease the error caused by the "dilution assumption" not being valid.

If the gray-scale values in the digital autoradiograph are considered to be intensities I, they can be converted to optical densities (OD) using the Beer-Lambert law [130]:

$$OD = -log\left(\frac{I}{I_0}\right), \tag{3.1}$$

where I_0 is the background intensity, which is taken as an average over several background points. To convert optical densities into local activities, a calibration function is needed. To this end the sample is always exposed with a calibration series of ^{14}C-PMMA standards with known activities (A). Using the intensities of these standards, one can obtain an exponential calibration function

$$OD = OD_{max} - OD_0 e^{-kA}, \tag{3.2}$$

where OD_{max}, OD_0 and k are fitting parameters. For the activity one can now find

$$A = -\frac{1}{k}ln\left(\frac{OD_{max} - OD}{OD_0}\right), \tag{3.3}$$

which can then be used for converting the gray-scale values (intensities) into local activities, pixel by pixel.

These activities can not however be converted directly to porosities, because this does not take into account the absorption of β-particles in the material they were traversing through. Since the

absorption rate is material dependent and different for the rock matrix and the PMMA itself, a β-correction factor is needed. As a rough approximation, the absorption of radiation is linearly dependent on density, and thus the β-correction factor can be considered as a ratio of the density of the sample (ρ_s) and the density of PMMA (ρ_0). If the sample is considered to be a two component system, its density depending on its porosity ϵ, the density of rock ρ_r and the density of PMMA. Thus a density corrected β-correction factor could be found such that

$$\beta = \frac{\rho_s}{\rho_0} = \frac{\epsilon\rho_0 + (1-\epsilon)\,\rho_r}{\rho_0}. \tag{3.4}$$

Now the local activities could be converted to local porosities. It could be assumed that ^{14}C-PMMA is diluted by porous rock and the majority of β-radiation is absorbed by it. The local porosity can be acquired as the ratio of the β-corrected local activity (A) and the activity of the pure ^{14}C-PMMA-resin (A_0), so that

$$\epsilon = \beta\frac{A}{A_0} = \frac{\frac{\rho_r}{\rho_0}}{1 + \left(\frac{\rho_r}{\rho_0} - 1\right)\cdot\frac{A}{A_0}}\cdot\frac{A}{A_0}. \tag{3.5}$$

Having acquired the local porosity of each pixel through Eqs (3.1) – (3.5), one can now determine the total porosity of the investigated area as an average of the local porosities as given by

$$\epsilon_{tot} = \frac{\sum\limits_{n=0}^{N} A_n\epsilon_n}{\sum\limits_{n=0}^{N} A_n} = \frac{\sum\limits_{n=0}^{N} \epsilon_n}{N}, \tag{3.6}$$

where N is the number of pixels, A_n the area of pixel n and ϵ_n the porosity of pixel n.

3.2   X-ray tomography

X-ray tomography is an imaging method that produces three dimensional images of the sample non-intrusively. It is based on detecting the difference in X-ray attenuation between different parts inside the sample. The sample is rotated with small, constant increments around its axis and a 2-d X-ray projection image, or a 'shadowgram', is taken at each step. The total rotation in a measurement is usually 180 or 360 degrees, but can also be somewhere in between. These shadowgrams, of which a few hundred to 2000 are usually taken, can then be computationally reconstructed into a 3-d attenuation map. As the X-ray attenuation coefficient of a material is generally proportional to the elemental composition and density of the material, the obtained image can be considered as a 3-d density map of the sample. Most common minerals have so much variance in their chemical composition and density that they cannot always be distinguished from each other, but several components, consisting of one or more minerals, can usually be distinguished from each other in a rock sample, such as in the article of Appendix I.

The X-ray tomographic images of this work were made with a SkyScan 1172 table top scanner and an Xradia MicroXCT-400 device, shown in fig. 3.1. Both devices are based on a conventional X-ray tube. X-rays coming through the sample are converted to visible light with a scintillator plate and then captured with a 2-d CCD detector. Reconstruction into a 3-d image is then done using the Feldkamp algorithm [131] which is common with conical-beam devices. In the SkyScan device the voxel size can be varied from 0.9 to 30 µm with a maximum sample diameter of 68 mm. In the Xradia device the voxel size can be varied from 0.3 to 7 µm with a maximum sample diameter of 20 to 100 mm, respectively.

Figure 3.1: The X-ray tomography devices used in the work, SkyScan 1172 (left panel) and Xradia MicroXCT-400 (right panel).

Noise is often an issue in tomographic images. Lots of noise reduction can be done in the device during the scanning to reduce need for image processing. The device based noise reduction is done in different ways with different devices. For example with the SkyScan 1172 device noise can be reduced by taking several shadowgrams from each angle and using an average of these shadowgrams. The more shadowgrams are used for averaging, the better the image quality will be. Using a smaller rotation increment can also reduce noise. With the Xradia MicroXCT-400 the noise reduction is done by using longer exposure times. In both cases noise reduction increases the measurement time, so a compromise must be made between the amount of noise reduced and the amount of time spent.

Considerable noise reduction can also be made in the reconstructed images. The simplest method, which sometimes works, is simple averaging. A small window of e.g. 2x2x2 voxels is moved over the image and the average gray-scale value inside the window is assigned to all pixels inside the window. This method is very fast, but it softens the boundaries between different materials and can even destroy some smaller features from the image. This is why a variance-weighted mean filter (VaWe) was used in the images shown in this work. The principle of VaWe is to use the local variance of the gray-scale values of the pixels in the considered window to determine the level of filtering. If the local variance (σ_L^2) is equal to the normal variance of noise (σ_η^2), filtering is the same as by normal averaging. If there is an interface in the window ($\sigma_L^2 > \sigma_\eta^2$) normal averaging would blur this interface. Therefore instead of using the average value of pixels, VaWe filtering is defined such that

$$u(x,y,z) = u^0(x,y,z) - \frac{\sigma_\eta^2}{\sigma_L^2} \left[u^0(x,y,z) - m_L \right], \tag{3.7}$$

where u is the filtered gray-scale value, u^0 is the original gray-scale value and m_L is the average gray-scale value in the window. In practice σ_η^2 is determined from a featureless area in the noisy image and the filtered pixel is inside a $nxnxn$ window, where n is a tunable parameter. This way if the local variance is high, the gray-scale value of a pixel remains almost unchanged. More smoothing can be obtained by running the algorithm several times. Comparison of averaging and VaWe is shown in fig. 3.2.
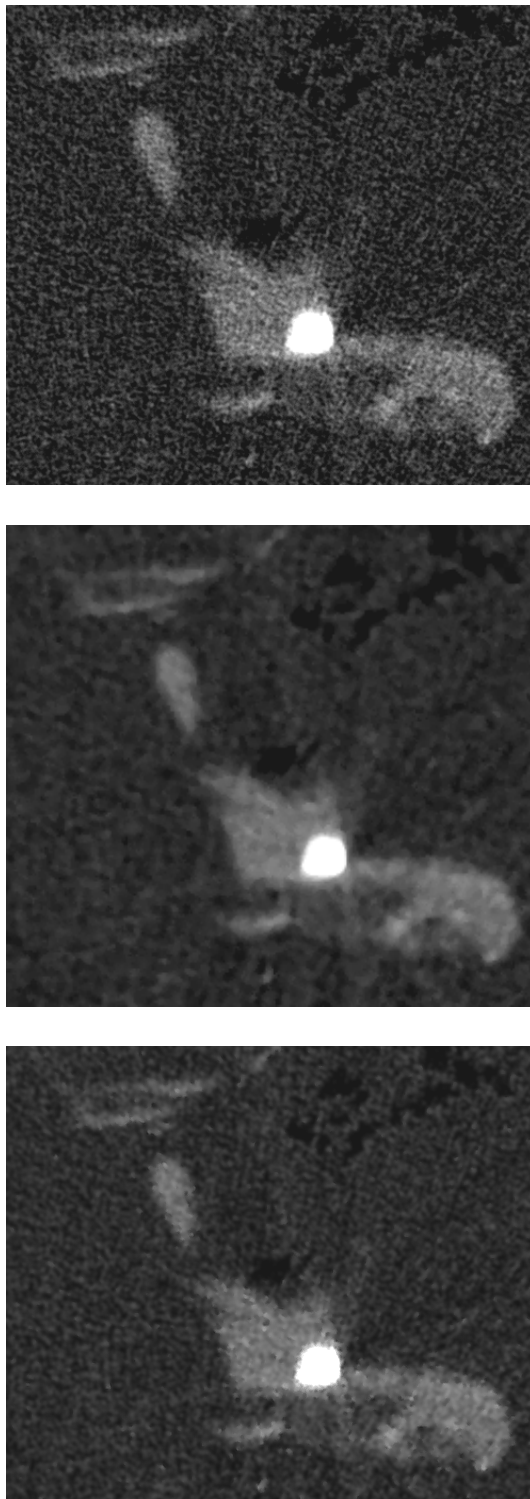
Figure 3.2: A cross-section of a tomographic image of a rock sample (top panel) filtered by normal averaging (middle panel) and the variable weight (VaWe) filter (bottom panel). Image width is 1.5 mm.

4 Rock structure characterization

Possible radionuclide transport in the geosphere can happen through advection in fractures or through diffusion through the rock matrix. Of the two, advection in water-flowing fractures is the faster and more prominent form of transport. It was thus useful to develop methods for characterising the fractures and the rock surrounding them in laboratory conditions. A method was developed to investigate fracture apertures for empty fractures all the way to micrometer scale. While this has been possible before with various optical and electron microscopy techniques, this method would allow automatic determination of several fractures at once from a centimeter scale sample, making the process much faster and statistically more relevant. For fractures that had already been filled, combining patterns in their properties were determined and the alteration and the porosity changes in the rock around them were studied.

4.1 Determining fracture apertures using the ^{14}C-PMMA technique

The ^{14}C-PMMA technique can be used for other things than determining porosity maps as well. Knowing the fracture aperture distribution for a certain rock type would be very useful for estimating transport properties of the rock [14, 15, 132]. Determining the aperture distribution is however not trivial. One big challenge is the fact that the size of the apertures can vary through several orders of magnitude [18]. A method was thus created that can convert activities in a ^{14}C-PMMA autoradiograph into fracture apertures. A theoretical model was first created through analytical calculations and Monte Carlo - simulations, which was then verified and corrected through experiments. The model and its verification are described in more detail in the articles found from Appendices II and IV.

Analytical model for a thin fracture

Let us begin with an analytical model for a thin (2-d) fracture, for which an expression for the probability of activation P and activation density ρ of a single point source S, located in a solid at a depth L, with a single beta particle emission length T_{max} in the solid, as shown in fig. 4.1 is first needed. The probability of activation P of the autoradiographic film is now

$$P = \frac{\Omega}{4\pi},\tag{4.1}$$

where Ω is the solid angle defined by the surface of the spherical calotte above the film surface. P can also be written as

$$P = \frac{1}{2}\left(1 - cos\left(\phi\right)\right) = \frac{1}{2}\left(1 - \frac{L}{T_{max}}\right),\tag{4.2}$$
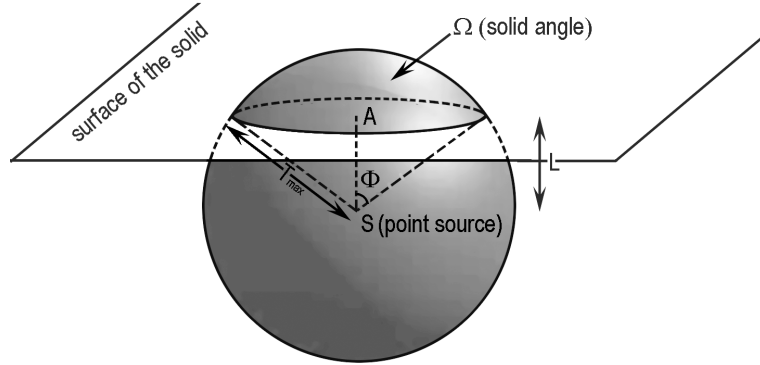
Figure 4.1: Beta particles emitted from a single point source S, located in a solid at depth L directly under point A with a single emission length T_{max}. Ω is the solid angle determined by the solid surface and ϕ the corresponding planar angle.
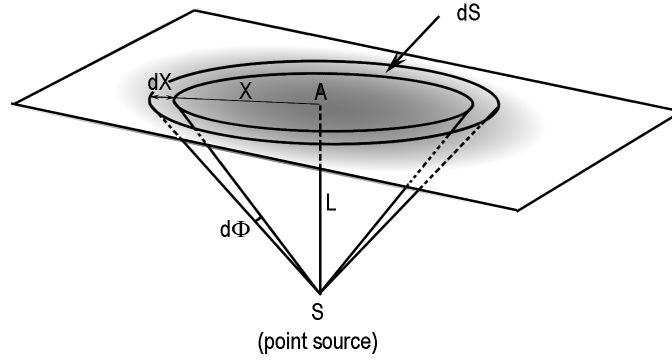
Figure 4.2: Schematic for differential handling of point source S at depth L. The angle $d\phi$ determines a strip of thickness dX located at distance X from point A. The area of the strip is dS.

where ϕ is the half-aperture angle of the intercepted cone. To now obtain $\rho(\phi)$, a circular layer of thickness dX on the film, defined by the angle $d\phi$ (see fig. 4.2) is examined. The density of emission in the circle with radius X is given by

$$\rho(\phi) = K\frac{dP}{dS},\tag{4.3}$$

where K is a constant. dP can be written as

$$dP = \frac{\partial P}{\partial \phi}d\phi = \frac{1}{2}\frac{\partial\left(1-cos\phi\right)}{\partial\phi}d\phi = \frac{1}{2}sin\phi d\phi.\tag{4.4}$$

and as can be seen from fig. 4.2, dS can be written as

$$dS = 2\pi \cdot X \cdot dX = 2\pi \cdot (Ltan\phi) \cdot \left(\frac{L}{cos^2\phi}d\phi\right) = 2\pi L^2\left(\frac{sin\phi}{cos^3\phi}\right)d\phi.\tag{4.5}$$

By combining Eqs (4.4) and (4.5) one can now get

$$\rho(\phi) = \frac{K cos^3 \phi}{4\pi L^2},$$

(4.6)

which can also be written as a function of distance from the profile center A

$$\rho(X) = \frac{K}{4\pi^2} \frac{L}{(L^2 + X^2)^{\frac{3}{2}}},$$

(4.7)

which cuts off to 0 at $X \geq \sqrt{T_{max}^2 - L^2}$. If an infinite line of point sources parallel to the surface at depth L is now considered, the case is equivalent to a point source in two dimensions. Now one can write as a function of ϕ

$$\rho(\phi) = K' \frac{cos^2 \phi}{\pi L},$$

(4.8)

where K' is a constant, or as a function of X

$$\rho(X) = \frac{K'}{\pi} \frac{L}{L^2 + X^2}$$

(4.9)

with the same cutoff point as Eq. (4.7). If finally a plane of point sources perpendicular to the film surface is considerd, it is analogous with a line perpendicular to the surface in 2-d, and the density profile on the film surface is given by

$$\overline{\rho} = \int_0^{\sqrt{T_{max}^2 - x^2}} \frac{L}{L^2 + x^2} dL,$$

(4.10)

which gives

$$\overline{\rho} = K ln \left(\frac{T_{max}}{x} \right).$$

(4.11)

So far only a constant beta emission length T_{max} has been considered, but the energies and therefore emission lengths of beta particles emitted by ^{14}C are not constant, but are distributed according to a probability density function (pdf) $f_E(e)$ with a maximum energy of 156.743 keV [133]. The energies can be converted to ranges using the Kanaya-Okayama (KO) relations [134], which are in agreement with experiments in the range 10–1000 keV:

$$\rho T = 5.025 \cdot 10^{-12} \cdot \frac{A E_0^{\frac{5}{3}}}{\lambda_s Z^{\frac{8}{9}}},$$

(4.12)

where ρ is the apparent density of the target, T is the maximum range of electrons in the target, A and Z are the average molar mass and atomic number of the target, respectively, and E_0 is the initial energy of the electrons (eV). λ_s is a constant, which is known to be 0.182 for E_0 in the range 10–1000 keV. Using this and separating the terms related to the target and the electron energy, one can write

$$T = 2.761 \cdot 10^{-11} \cdot \underbrace{\frac{A}{\rho Z^{\frac{8}{9}}}}_{\text{solid}} \cdot \underbrace{E_0^{\frac{5}{3}}}_{\text{electrons}}.$$

(4.13)

It needs to be noted that the KO-equations only give the maximum range of an electron, so the ranges are still being slightly overestimated. For the Monte Carlo simulations the energy E of electrons that have traversed a distance x in the solid is still needed, and is given by [134]

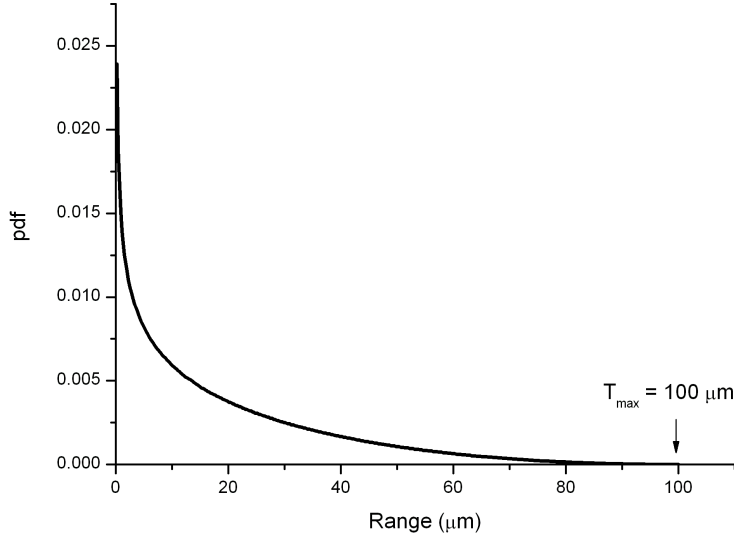$$E = \left(1 - \frac{x}{T} \right)^{\frac{3}{5}} E_0.$$

(4.14)

Figure 4.3: Probability distribution function (pdf) for ranges of β^- particles emitted by ^{14}C. The maximum range is normalised to 100 μm.

Eq. (4.12) can now be used to convert the energy-pdf $f_E(e)$ to a range-pdf $f_T(t)$ by using the $E_0^{\frac{5}{3}}$ dependency. The properties of the solid can be ignored if the T_{max} of the pdf is normalised to an arbitrary distance, like 100 μm (see fig. 4.3). One can then determine the maximum range for any given material and rescale the pdf to that maximum. Using this range-pdf a more accurate probability of activation P than given by a single T_{max} in Eq. (4.2) can now be calculated. It is given by

$$P = \frac{1}{2} \sum_{t=0}^{T_{max}} f_T(t) \cdot \left(1 - \frac{L}{t}\right), \tag{4.15}$$

only for $t \geq L$. The probability of activation obtained from Eq. (4.15) is shown in fig. 4.4. Now to get a good analytical baseline for the simulations the range-pdf needs to be used for the emission density of a planar source. The emission density of Eq. (4.11) now becomes

$$\rho(x) = K \cdot \sum_{t=0}^{T_{max}} f_T(t) \cdot ln\left(\frac{t}{x}\right), t \geq x, \tag{4.16}$$

where K is an integration constant. This emission density, shown in fig. 4.5 is much narrower than the originally acquired emission density for a single length T_{max}, since the pdf has a low probability for high-energy particles.

Monte Carlo simulations

So far an ideal planar fracture in a homogeneous medium has been discussed, but in the nature that is never the case. Even if you consider the host rock to be homogeneous, it has a different physical and chemical composition than the PMMA the β^- particle has to traverse through before reaching the surrounding rock. A schematic of a simplified natural case is shown in fig. 4.6. Even this simple case
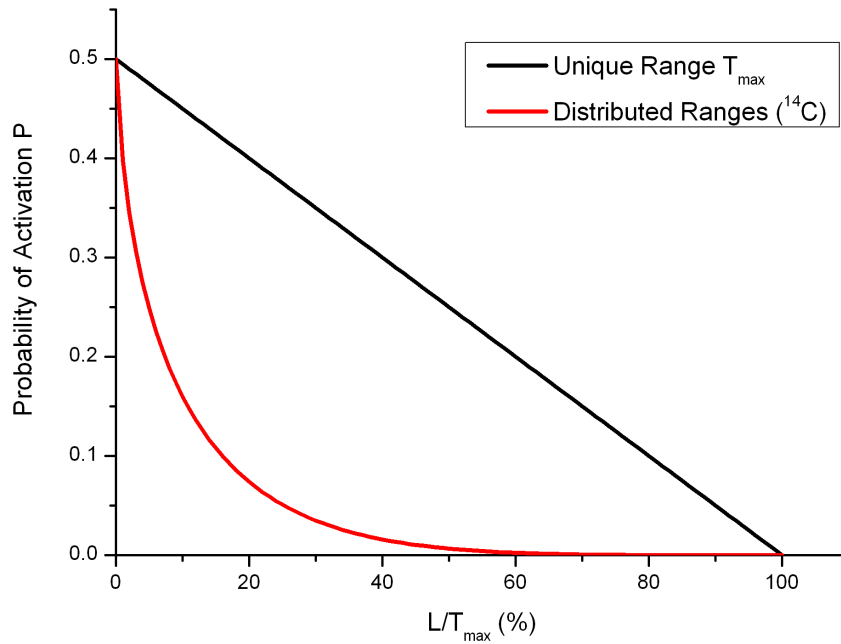
Figure 4.4: Probability of activation for a point source at depth L in the solid for the unique range model and ranges distributed by the ^{14}C - pdf.
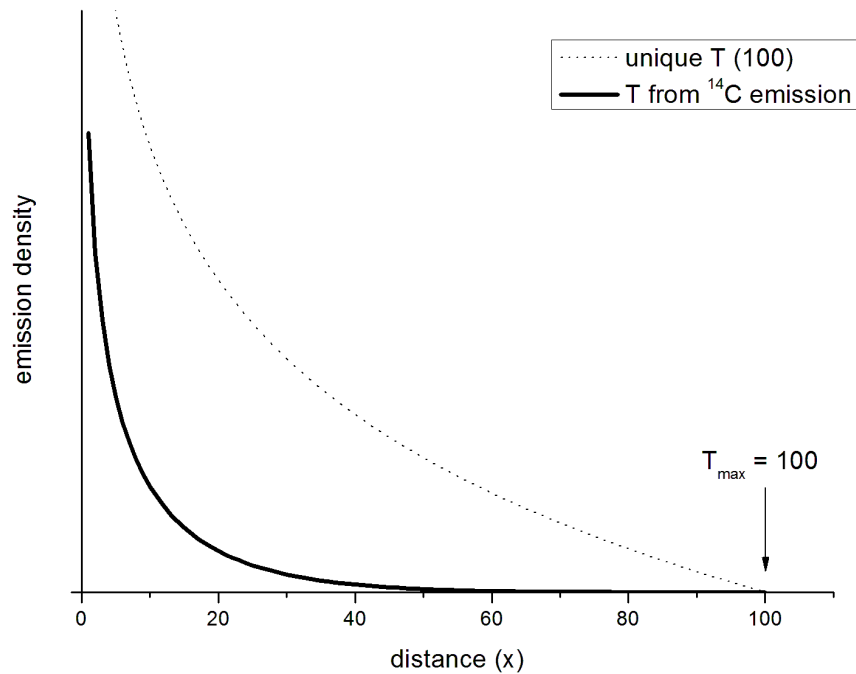

Figure 4.5: Emission density for a planar source perpendicular to the surface for a single emission range and ranges according to the ^{14}C range-pdf. Maximum range is set to 100μm for both cases.
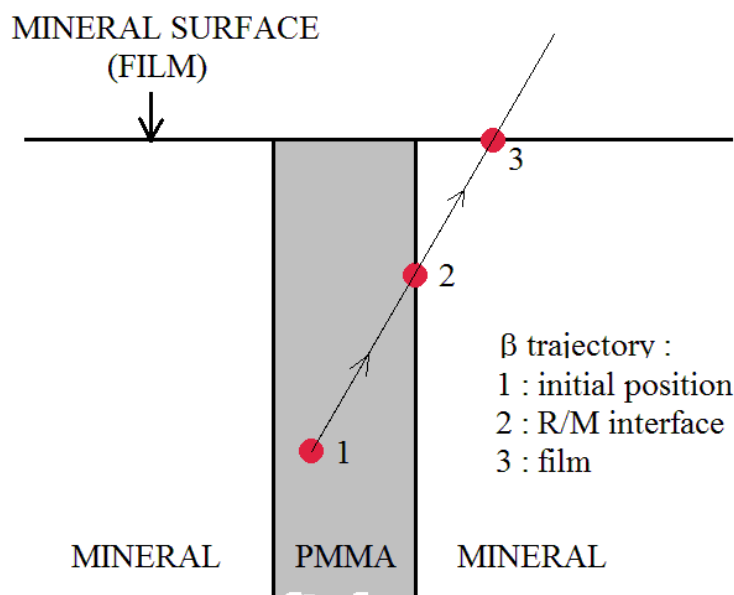
Figure 4.6: A simplified natural scenario where a β^- particle is emitted from the fracture (1) and traverses over the pmma/quartz interface (2) to reach the autoradiographic film (3) on the surface.

is very difficult to solve analytically, as the particle can take several different paths to the surface. This is why Monte Carlo (MC) simulations were used instead.

The MC simulations were performed in 2-d for a fracture perpendicular to the film, filled with PMMA and surrounded by a quartz matrix. The fracture area was divided into equally spaced point sources and a desired number of β^- particles was emitted from each source. For each electron an angle between 0 and π up from the horizontal level and a path length according to $f_T(t)$ of ^{14}C was chosen at random. The path of the electron was approximated with a straight line to simplify the simulation, as the focus was more on gaining information and understanding on the shapes of the activity profiles seen on film rather than refining the simulation as close to reality as possible.

There were now three separate cases concerning the electron paths. In the first case the electron path went only through PMMA, in which case it sufficed to check if the emission range was greater than the distance to the film along the emission path. If so, the emission density at the intersecting point was increased by one. Another simple case was that of an electron emitted from the PMMA/quartz interface that only traversed in quartz. This case was treated just like the first one, except the emission range was checked in quartz instead of PMMA. The slightly more complicated case was the one depicted in fig. 4.6, where the electron traversed in both PMMA and quartz. In this case it was first checked if the electron reaches the PMMA/quartz interface and if it does, how much energy does it have left at the interface according to Eq. (4.14). This energy was then used to calculate a new range in quartz, which was checked against the remaining distance to the film. The emission density was again increased by one if the electron reached the surface. This means the interaction between the film and the electrons was also ignored, which caused some uncertainty to the simulation. The activities were finally normalised by the theoretical activity of the ^{14}C-PMMA resin (A_0). The code was implemented on Visual Basic sheets under MS Excel^{TM}. It was statistically enough to use 2–3 million particles for calculating one fracture profile. One calculation of this size was completed in less than 10 seconds.

Activity profiles obtained by the MC simulations are shown in fig. 4.7. Three distinct profile shapes could be seen here. First, the shapes of the activity profiles from thin fractures (aperture ≤ 4 μm) were almost exactly the same as the analytical solution (fig. 4.7 b). For thin fractures the emission density increased as the fracture aperture increased, which is equivalent to activity increasing within an ideal planar source. Second, for intermediate fractures (4 μm $\leq$ aperture ≤ 200 μm) the profile started to widen and the normalised activity ($\frac{A}{A_0}$, where A_0 is the activity of the resin) increased towards 1. Third, for thick fractures (aperture ≥ 300 μm) the profile started to resemble a box function with a maximum normalised activity of 1 and widened as the fracture aperture increased. It was now clear that the original goal of one analysis method that transforms activity profile into fracture aperture would not be possible. Thin fractures would be processed using normalised activity at the fracture center and thick fractures using the width of the profile. Some kind of combination of the two methods would be used for the intermediate fractures.

The Full Width at Half Maximum (FWHM) of the profiles was measured to better quantify the change in profile shape. FWHM is also a property that is measurable from a real autoradiograph. The FWHM values are shown in fig. 4.8. This confirmed the visual assessment that the shape remains the same for thin fractures. For thick fractures the FWHM was equal to the fracture aperture and already for apertures larger than 20 μm the FWHM was very close to the real aperture.

When analysing thin fractures in real autoradiographs with this method, one needs to take into account the fact that in a digitised autoradiograph the pixels are very rarely equidistant to the fracture center, as shown by fig. 4.9. Thus the activity seen at fracture center is not constant even if the fracture aperture is, but rather a function of distance to the real center. Thus one needs to investigate moving averages of the profiles, with pixel size S as the kernel size and distance from the fracture center varied from 0 to $\frac{S}{2}$. The resulting curves are shown in fig. 4.10.

Now it could be seen that the average $\frac{A}{A_0}$ for thin fractures formed a line on a log-log scale and could be described with a power law function. All curves naturally saturated to $A = A_0$, but this happened later for bigger pixel sizes. This was to be expected, as the bigger the pixel, the wider the fracture can be to be thin compared to pixel size. A power law fitted to the early part of the curve gave

$$\frac{A}{A_0} = a^{1.04} \cdot e^{-0.616 \cdot S^{\frac{1}{3}} - 2.469}, \tag{4.17}$$

where a is the fracture aperture and S is the pixel size. Since the exponent of a is roughly 1, the curve was also linear in linear coordinates, which was also expected since thin cracks act like a plane crack with a varying activity. Now that a method for converting activities of thin fractures into fracture apertures had been proposed, a method for thick apertures was still needed. There segmentation by boundary could be used, meaning that if, for a given pixel, the normalized activity $\frac{A}{A_0}$ was below a threshold value T, the pixel would be considered belonging to the fracture. It was shown in fig. 4.8 that FWHM, e.g. $T = 0.5$, works well for fractures with apertures above 100 μm. It is, however, inaccurate for apertures smaller than 100 μm. Therefore, to improve boundary segmentation for intermediate fractures, several threshold values $T \leq 0.5$ were evaluated from the simulated profiles. This is shown in fig. 4.11, where a_T is the aperture obtained by segmentation. It can be seen that at small apertures the lower values of T overestimate the aperture and this effect diminishes as T approaches 0.5. Thus choosing a low T is as inaccurate as choosing a too high T. A threshold value between 0.25–0.35 is a good compromise, as it minimises the overestimation of a_T, while simultaneously being able to estimate apertures near 20 μm. $T = 0.3$ was found to be a suitable value. With that value, maximum $\frac{a_T}{a}$ is reached at a=40 μm when $\frac{a_T}{a} = 1.125$. For apertures from 20 μm to 100 μm the average $\frac{a_T}{a}$ is 1.095 and for apertures over 100 μm it is only 1.021. These slight overestimations are offset by the spatial discretisations caused by using a discrete pixel size. For example using a 20 μm pixel size, all apertures where 20 μm $\leq a_T < 40$ μm are detected as a single pixel, i.e. 20 μm.
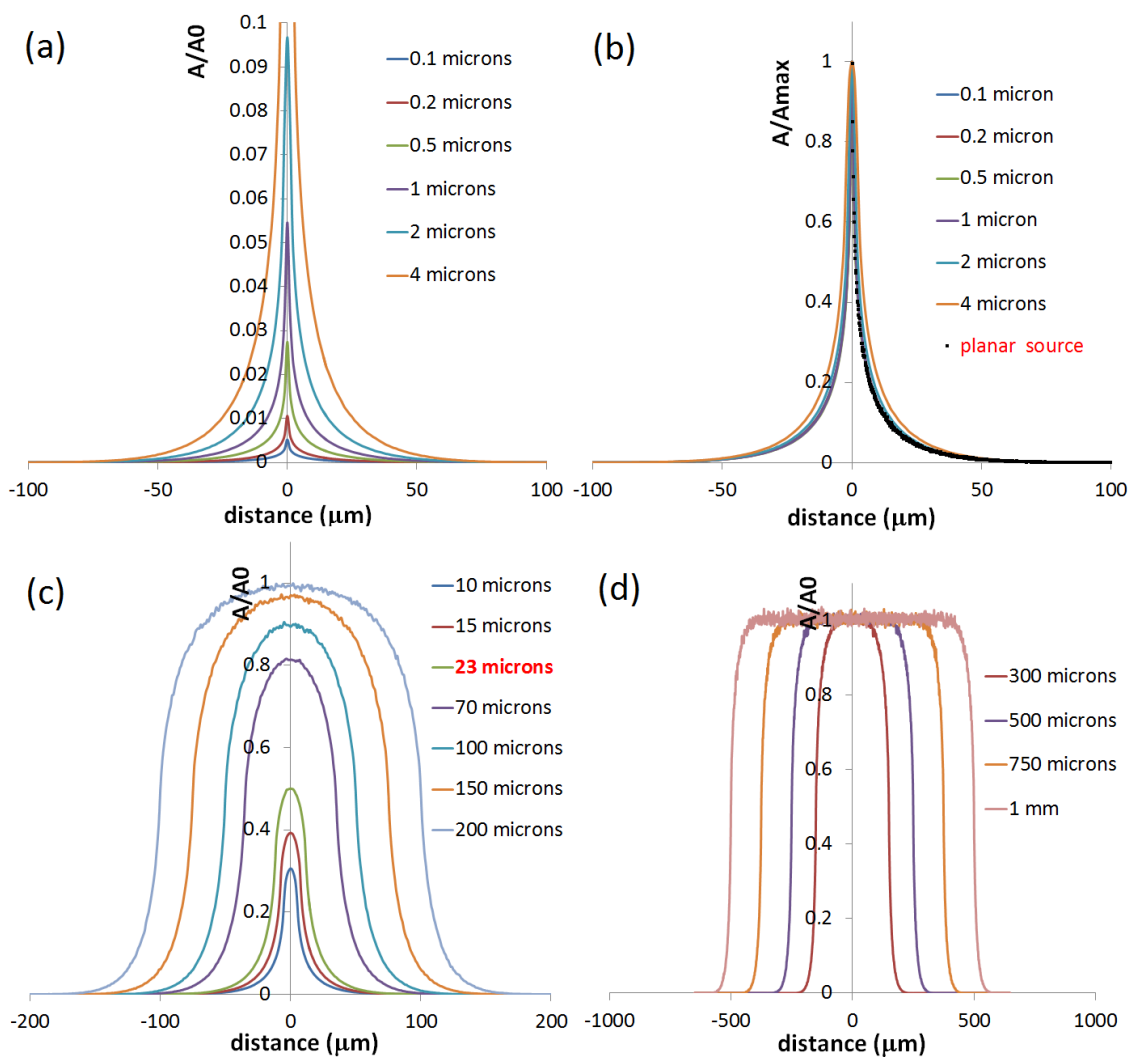
Figure 4.7: Activity profiles on autoradiographic film for fractures of various apertures obtained by Monte Carlo simulations. Profiles for thin fractures (aperture ≤ 4 µm) are presented without (a) and with (b) normalisation to the maximum. Analytical solution for a plane fracture is included in (b). Profiles for intermediate (4 µm $\leq$ aperture ≤ 200 µm) (c) and thick (aperture ≥ 300 µm) (d) fractures are not normalised.
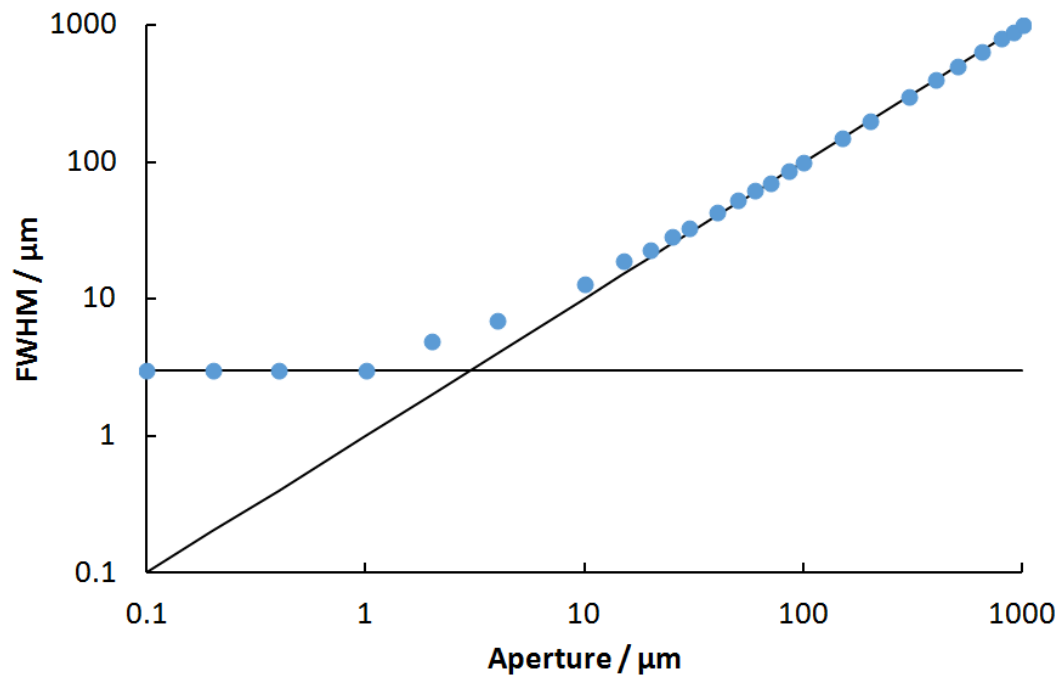
Figure 4.8: The Full Width Half Maximum (FWHM) of activity profiles as a function of corresponding fracture aperture. The solid slope marks FWHM = aperture.
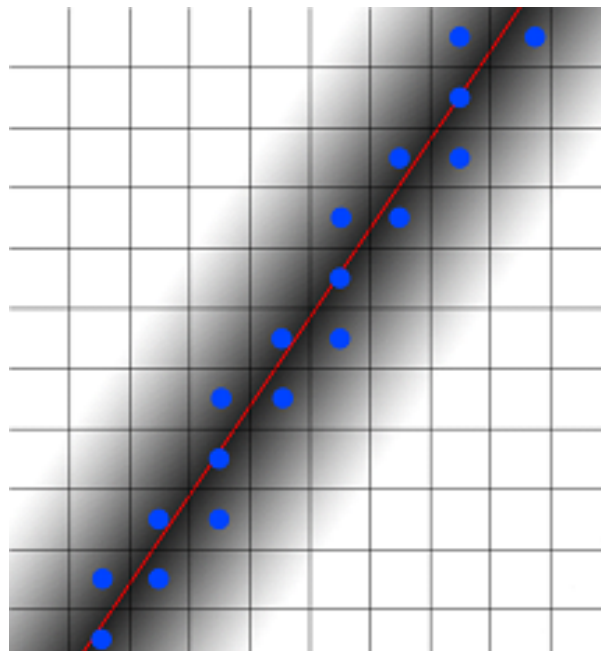
Figure 4.9: A network of square pixels superimposed on an activity profile of a fracture with the center line marked in red. The center of pixels that define the digitised center line of the fracture, marked with blue dots, are dispersed around the true center line.
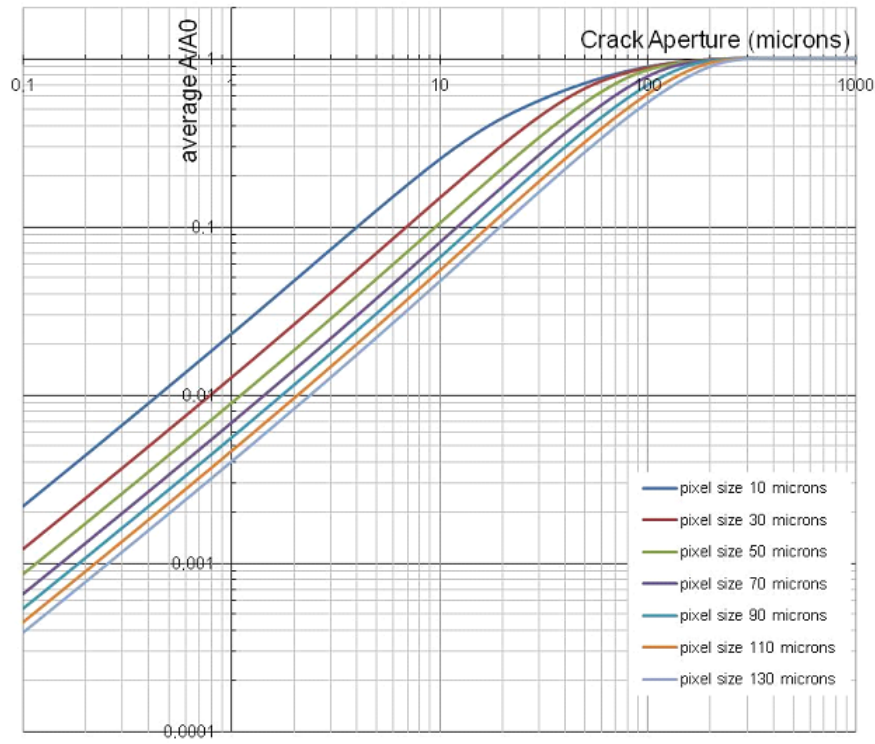
Figure 4.10: Moving averages of fracture activity profiles calculated with several pixel sizes for several apertures.
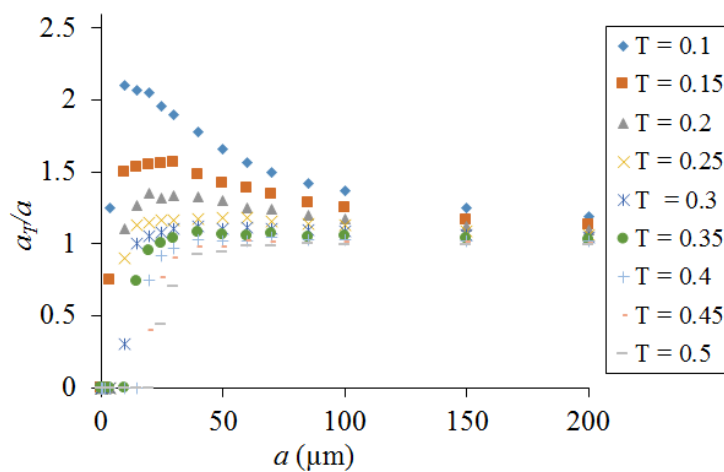
Figure 4.11: The ratio of aperture obtained by segmentation (a_T) to the actual aperture (a) for several threshold values (T).
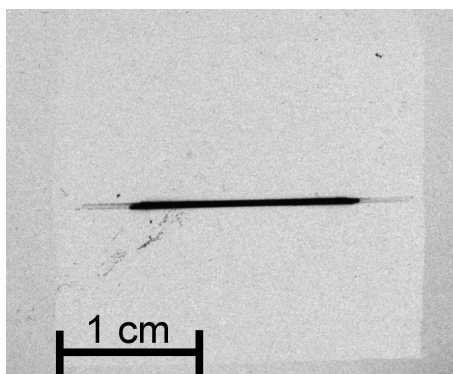
Figure 4.12: Digitised autoradiograph of a glass plate sample with an artificial fracture with a 90 μm aperture.

Verification of simulation

The next natural step was validating the method just proposed by experiments. To this end artificial fracture samples were manufactured using glass plates with mylar and Al-foil spacers for creating different apertures. Commercial glass plates have a roughness below 10 nm, making them very suitable for this kind of samples [135, 136]. Glass plates of 10 mm thickness were cut into rectangular pieces of 15x50 mm and 15x100 mm. Then spacers consisting of small strips of Al foil of various thicknesses (0.6, 2, 6, 12.5 and 90 μm) in various stacks and of Al-coated mylar foil of 1.5 μm thickness were placed between the plates to set the aperture. One sample was also prepared with no spacer for identification of possible artefacts. The plates were pressed together with clamps and epoxy resin was applied around the margins. Small incisions for application of ^{14}C-MMA and to pass residual air were left open. Interference patterns seen in the samples during inspection under a lamp showed that the apertures were in the range of the wavelength of light and that even the 10 mm thick glass was slightly bent over the relatively short distance of 10–20 mm between the foil spacers due to the applied pressure from the clamps. A mixture of hydroxyethylmethacrylate (HEMA) and ^{14}C-MMA (mixing ratio 75:25, specific activity 17.2 μCi/mm) was then added to the fractures along with 0.5 g/100 ml of benzoylperoxide (BPO) as a radical starter for the polymerisation and 0.25 g/100 ml of yellow fluorescent dye for checking the films under UV light. The incisions were then covered with epoxy resin and the samples were exposed to a 360 nm UV light (5 W) for about 24 h at a temperature of 10–15 °C. The polymerisation caused various shrinking artifacts, such as circular voids and fractal fissure networks, which needed to be accounted for in the analysis of the samples. Finally the samples were cut in half and the examined surfaces were polished.

The glass plate samples were exposed on high performance ^{14}C: Kodak BioMax MR autoradiographic films for exposure times ranging from five hours to 21 days together with a ^{14}C-PMMA calibration series of eight specific activities between 0.0125 and 2.5 μCi/mL. A wide range of exposure times was used because it was not known beforehand what would be optimal with regards to saturation. The autoradiographs were scanned at 200 dpi, 400 dpi, 800 dpi and 2400 dpi resolutions. An autoradiograph of a single sample is shown in fig. 4.12.

The actual apertures of the samples were determined using a scanning electron microscope (SEM) for small aperture samples and a visual microscope for large aperture samples, since it was deemed accurate enough for the largest apertures. The apertures for the small aperture samples were found to be between 2–28 μm and the apertures of the large aperture samples between 50–270 μm. Microscopic
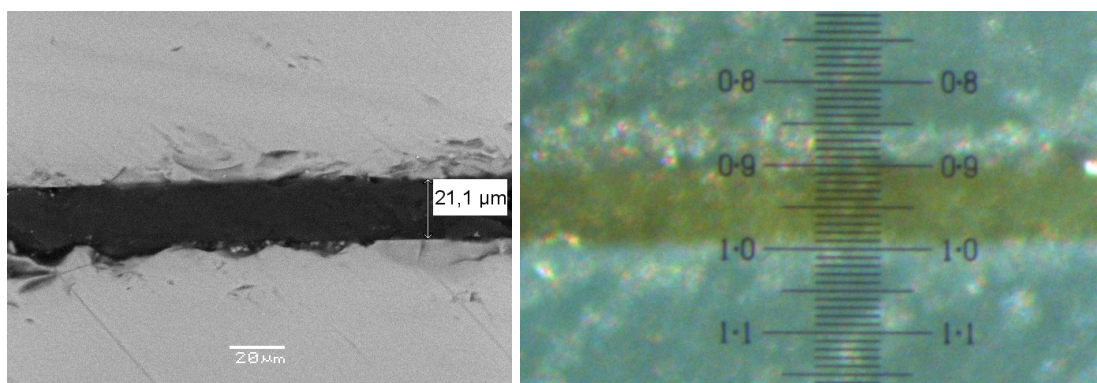
Figure 4.13: Scanning electron microscope (SEM) back-scattered electron (BSE) image of a glass plate sample with an aperture of 21 μm (left panel) and an optical microscope image of a glass plate sample with an aperture of 90 μm (right panel).

images of two samples are shown in fig. 4.13. The digitised autoradiographs were converted to activity maps using Eqs (3.1)-(3.3). Here special attention needs to be paid to the calibration curve resulting from Eq. (3.3), an example of which is shown in fig. 4.14. The calibration curve has a linear section, that reaches roughly to $OD = 1.5$ in the example. If the optical densities are not in the linear range, film saturation decreases the accuracy of the optical density - activity conversion. This is a smaller problem when determining bulk porosities, as then high activity pixels rarely play a major role, but in this case the pixels with the highest activity are the most important.

Several activity profiles for single pixel lines were then calculated for each artificial fracture. In theory a single profile could already be used to determine fracture aperture, but one must take into account the dispersion of peak pixels shown in fig. 4.9. This causes variation in peak height for activity profiles from a single fracture, so some averaging needs to be done. Fracture curvature or inaccurate verticalisation of the fracture image can also cause the peak to drift a bit to the side, which can be corrected by realigning all activity profiles in such a way that the maxima are in the same column. Both effects are shown in fig. 4.15. After realignment all activity profiles obtained from a fracture were averaged to get one activity profile for the fracture. The peak value of this profile would now correspond to the moving average used in fig. 4.10.

The shapes of the profiles were investigated first. The model predicted a constant FWHM of 4 μm for thin fractures with apertures up to 4 μm with the shape still remaining fairly stable until the aperture is much bigger than the used pixel size. Several activity profiles for thin fractures normalised to maximum are shown in fig. 4.16. The profile shapes acted like the model predicted, staying fairly constant when the aperture was below the pixel size and gradually starting to widen when the aperture was above the pixel size. The big difference to the model was the width, which was about one order of magnitude more than predicted. This could be accounted for by the simplifications of the model, mostly the lack of interaction with the autoradiographic film and the thickness of the film.

Thick fracture profiles are shown in fig. 4.17. First it could be seen that $T = 0.5$ is not a good threshold, as it underestimates the widest fractures and does not detect the 90 μm aperture samples at all, as the whole profile is under the threshold value. However thresholding at $T = 0.2$ gave a decent estimate for the wider apertures and only failed to detect the 70 μm aperture sample. Thresholds lower than 0.2 caused too much overestimation for the wide fractures. When the FWHM was plotted
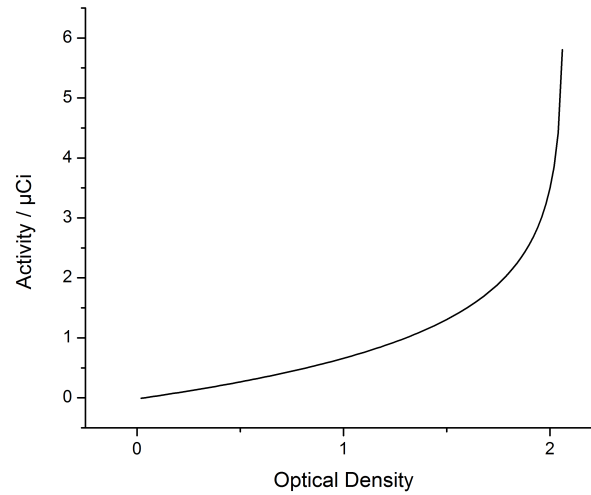
Figure 4.14: An example of a calibration curve for converting optical densities from an autoradiograph into activities.
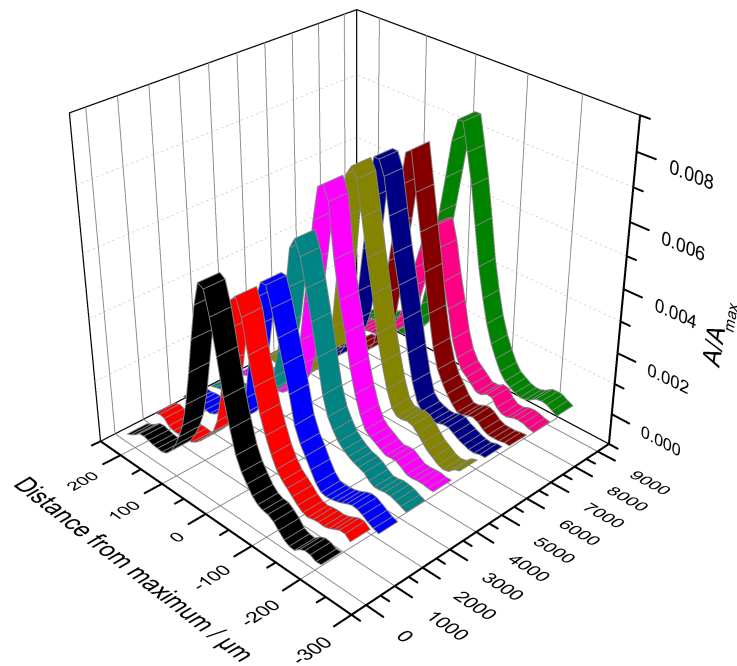
Figure 4.15: Ten one-line activity profiles for a glass plate sample all taken 1 mm apart from each other, showing both varying peak height and peak position drift. Fracture aperture is 10 μm. Resolution is 2400 dpi, i.e. pixel size is 10.6 μm.
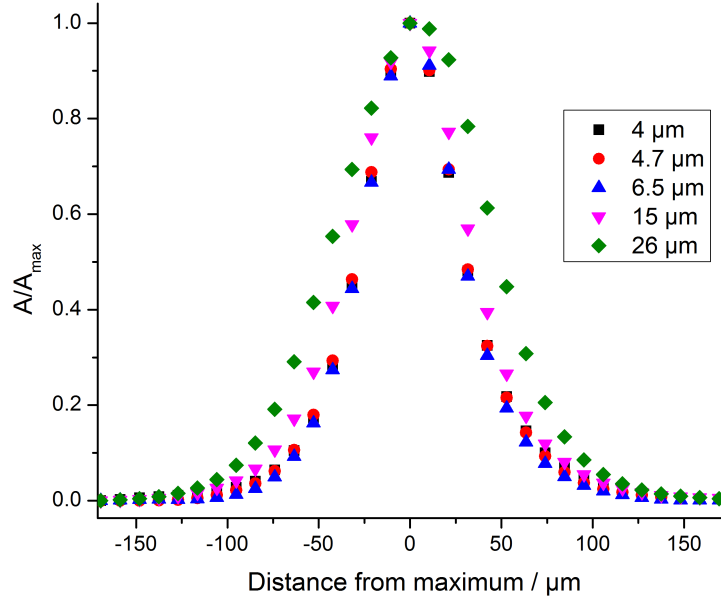
Figure 4.16: Activity profiles for thin fractures normalised to maximum. Used resolution is 2400 dpi, i.e. pixel size is 10.6 μm.

against the real fracture apertures (fig. 4.18), it could be seen that it behaved just like the model predicted (see fig. 4.8).

To try another method for determining fracture aperture for thick fractures, a one dimensional "pore volume" was calculated for each fracture by first calculating local porosity in each pixel according to Eq. (3.5) and multiplying it by the pixel size and then summing up these one-pixel one dimensional pore volume elements. As can be seen from fig. 4.19, this method is usable if the exposure time is kept short enough to avoid film saturation. It needs to be noted that with the three day exposure (fig. 4.19, left panel) the thin fracture samples are not saturated and the method grossly overestimates their aperture. It is thus not usable for thin fractures.

Now methods for converting activity profiles to fracture apertures were confirmed for thick fractures, but the thin fractures still needed some work, so the normalised activities $\frac{A}{A_0}$ were plotted as a function of fracture aperture, as shown in fig. 4.20. Thick fractures had to be left out of the plot as they were saturated and thus not compatible with the rest of the data. The behaviour of the activities was as expected since they could be described with a line that passes through the origin. It is more natural to write the linear relation the other way around:

$$w = z \cdot \frac{A}{A_0}, \tag{4.18}$$

where w is the aperture and z is a function of pixel size and also inverse of the slope of a fit like the one shown in fig. 4.20. To get a more general relation between the activity profile and aperture, the dependence of z on pixel size still needs to be investigated. As fig. 4.21 shows, a coarse approximation can be done with a second order polynomial fit. The fit shown in the image, $z = 0.014 \frac{1}{\mu m} S^2 - 0.47 S + 67$ μm seems to give a good approximation for larger pixel size, while a constant $z = 62$ μm works for pixel sizes below 30 μm.
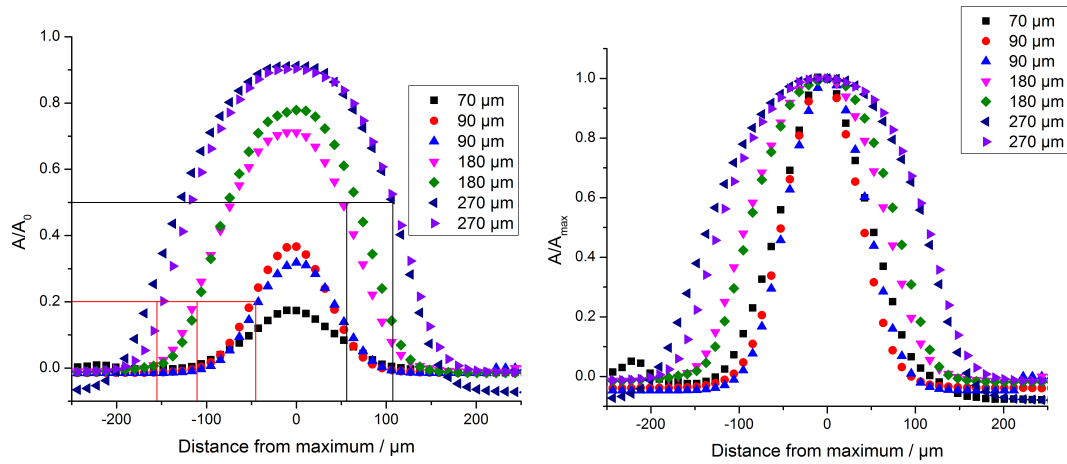
Figure 4.17: Activity profiles for thick fractures without (left panel) and with (right panel) normalisation to maximum. Thresholding at T=0.2 and T=0.5 are shown on the left panel. Used resolution is 2400 dpi, i.e. pixel size is 10.6 μm.
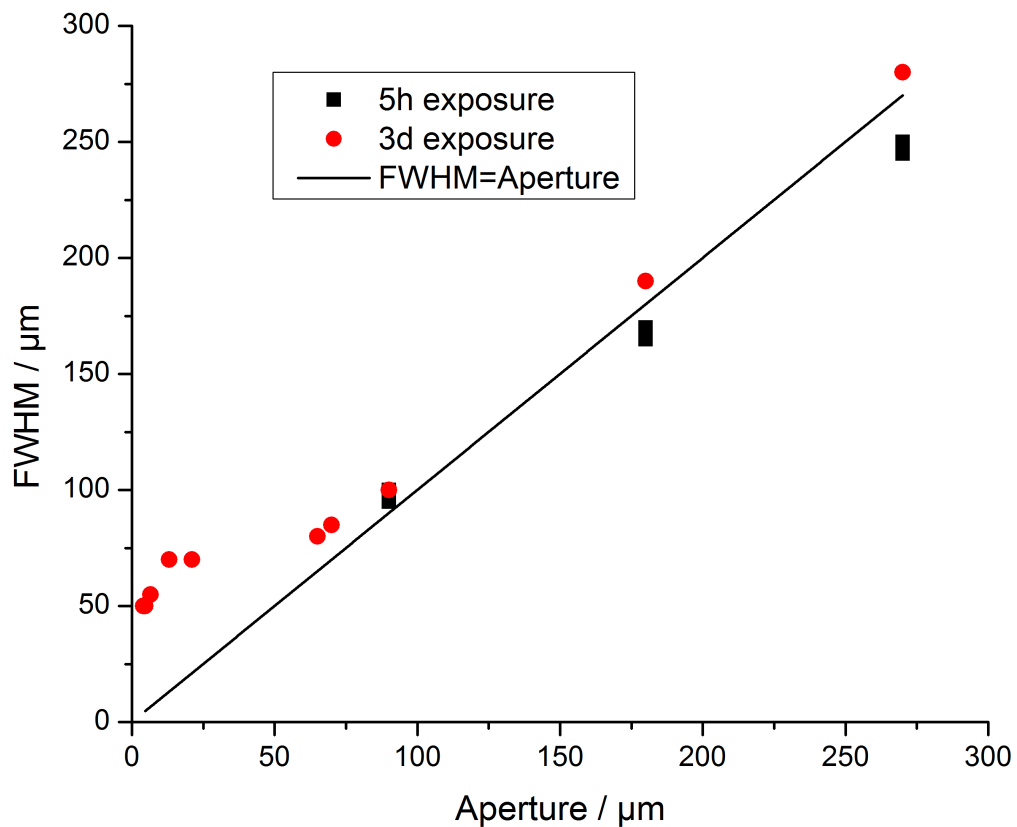
Figure 4.18: FWHM of activity profiles with two different exposure times as a function of real fracture aperture shows similar behaviour as the model predicted (see fig. 4.8).
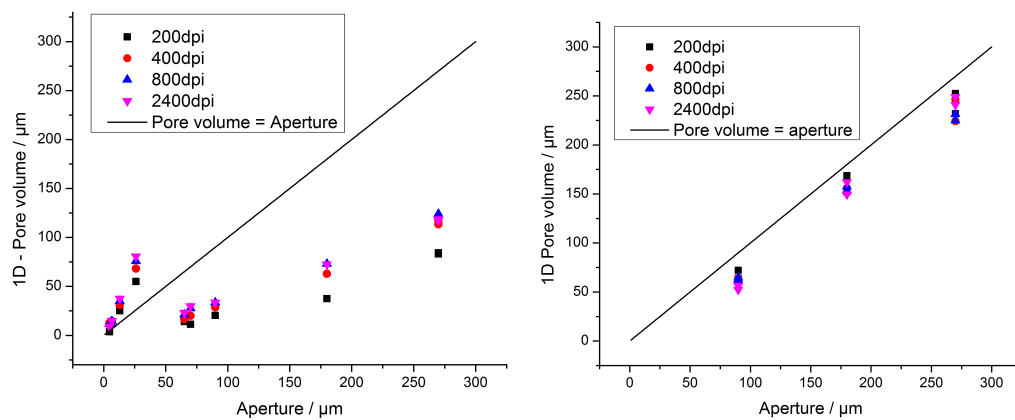
Figure 4.19: Left panel: 1D pore volumes of artificial fractures as a function of fracture aperture for a three day exposure, where the film is partly saturated. Right panel: Similar plot for a five hour exposure, where the film is not saturated.
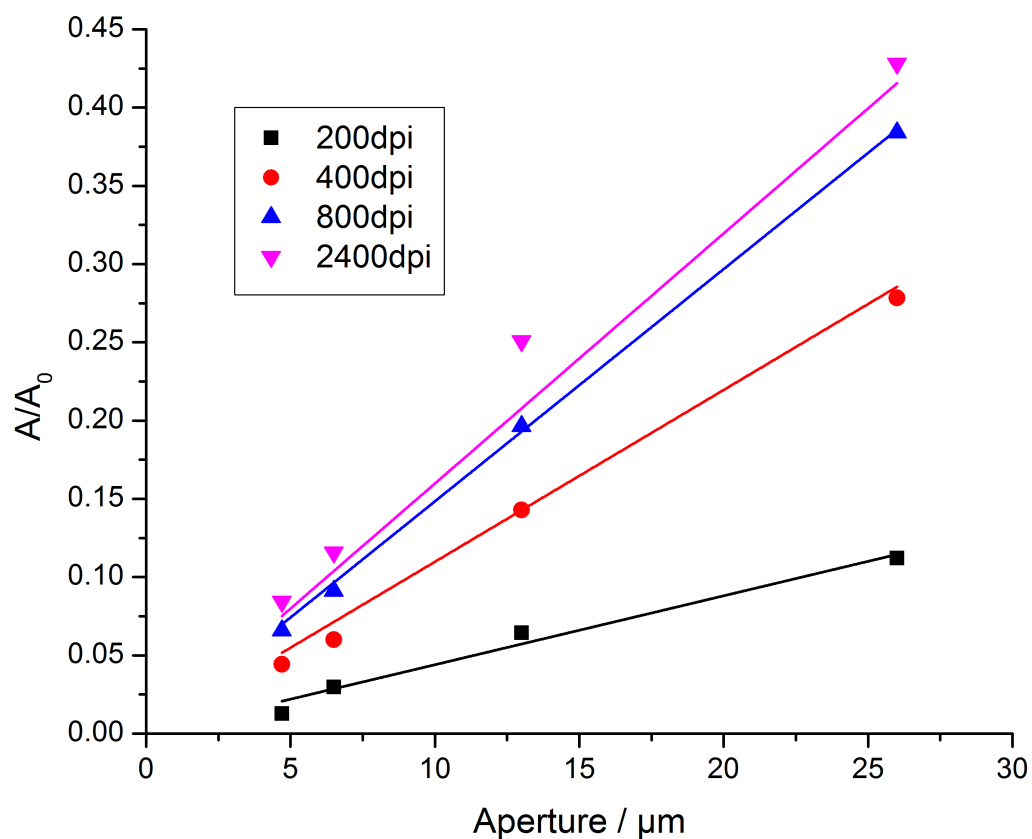
Figure 4.20: Peak activities of glass plate samples as a function of real fracture aperture. The linear fits have the same color as the corresponding data set.
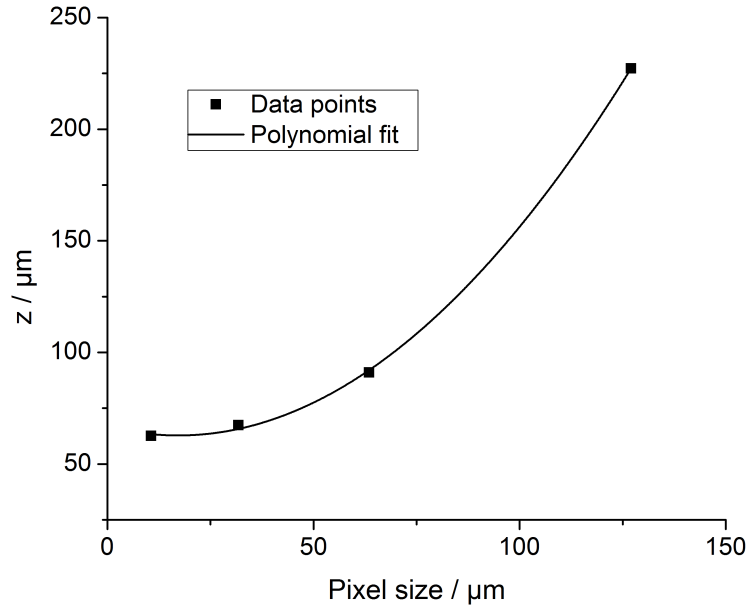
Figure 4.21: z plotted as a function of pixel size.

We have therefore shown that the method described above can be used to convert activity profiles into fracture apertures. The peak activity conversion works well for apertures below 30 μm and segmentation by $T = 0.2$ works for apertures above 50 μm. For intermediate fractures with apertures between 30 μm and 50 μm no single method could be proposed, but a combination of the two methods should give a decent approximation. The problem at this point is of course practical implementation, which still requires work. The method should also be improved to take fracture inclination into account and using digital autoradiography would make the saturation issues less important. Fracture filling and alteration around the fracture are also issues that could be resolved through further testing.

4.2 Rock alteration around fractures

Characterising fractures that have had water flowing in them and the alteration around those fractures can give vital information on the processes in such a fracture and their effect on radionuclide transport. In this section a closer look is taken at characterisation of water-flowing fractures in Olkiluoto. In the Olkiluoto bedrock the fractures are typically dominated by calcite, hydrothermal clays or both. Many fractures are single faults with slickensided surfaces. The calcite is often in the core of the fracture filling system and is generally a part of the latest filling phases. It is found even in non-cohesive clays as a 'glue' between clay particles. Calcite and sulfides usually occur together on surfaces of hydrothermal clay minerals. For this study three fracture types typical to the Olkiluoto area were selected: calcite dominated fractures, clay dominated fractures and slickensided fractures. [31, 137] The mineralogical and porosity changes and other characteristic properties near fracture surfaces of twelve drill-core samples were studied using X-ray tomography, the ^{14}C-PMMA autoradiography technique, and optical microscopy. All samples were sawn in half and one half was used for tomography and the other half for autoradiography and microscopy. The technical details of the performed measurements can be found in the article in Appendix I.

Figure 4.22: Mineral component distributions as a function of distance from the fracture surface for a calcite fracture (OL_KR13_227.40, left panel), a clay fracture (OL_KR25_56.78, middle panel) and a slickensided fracture (OL_KR14_491.19, right panel). Components with a smaller number are more dense than those with a larger number.
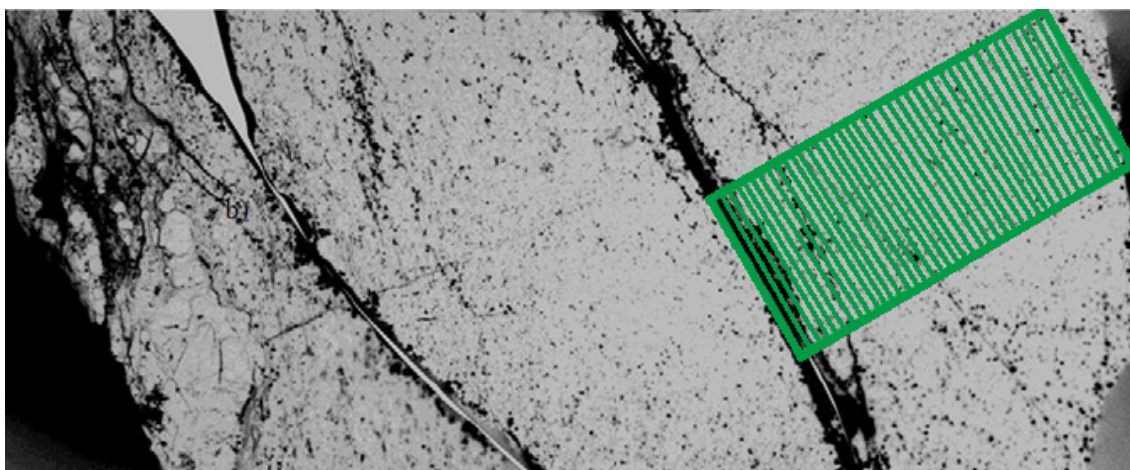
Figure 4.23: A digital autoradiograph and an example of division into rectangles parallel with the fracture to obtain a porosity distribution relative to the distance to the fracture.

The 3-d tomographic images were first filtered for noise with the VaWe algorithm. A gray-scale based mineral analysis of the resulting data was then done in 2-d by manual thresholding. The threshold values were determined visually. The abundances of each mineral component were then determined from the amount of voxels belonging to each gray-scale value range. To determine the distributions of the mineral components as a function of distance to the fracture, the tomographic image of each sample was divided into stacks of the shape of the fracture surface and the mineral composition of each stack was analysed separately. An algorithm using a dynamic 3-d surface [138] was used to detect the fracture surface and the image stacks were realigned accordingly to achieve surface-shaped stacks. Examples of these distributions are shown in fig. 4.22, one from each fracture type.

Porosity distributions as a function of distance to the fracture surface were obtained by dividing the autoradiographs into rectangles parallel with the fracture, as shown in fig. 4.23. Examples of these distributions are shown in fig. 4.24.

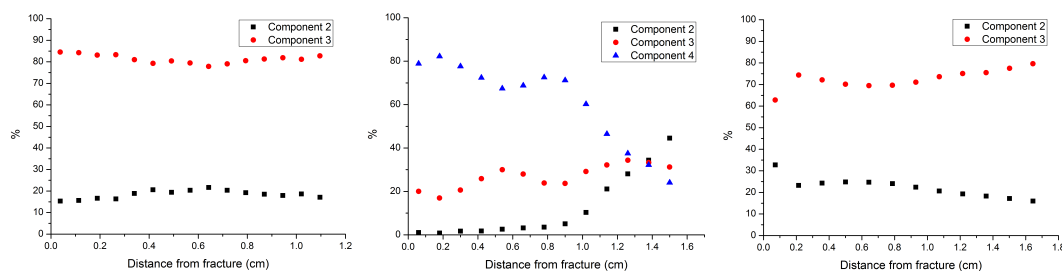For one clay fracture sample, OL_KR25_56.78, shown in fig. 4.25, it was possible to identify the
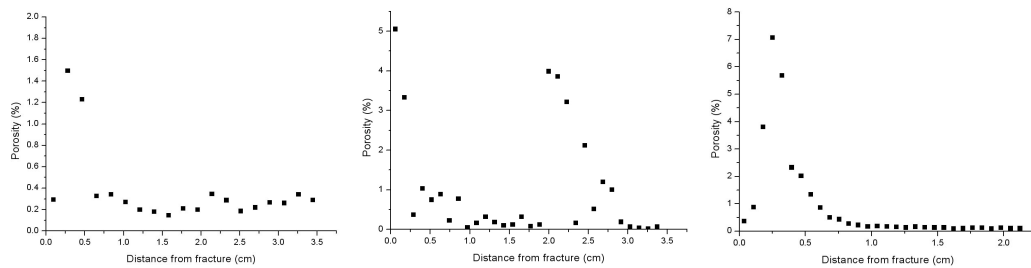
Figure 4.24: Porosity distributions as a function of distance from the fracture surface for a calcite fracture (OL_KR13_227.40, left panel), a clay fracture (OL_KR25_56.78, middle panel) and a slickensided fracture (OL_KR14_491.19, right panel).
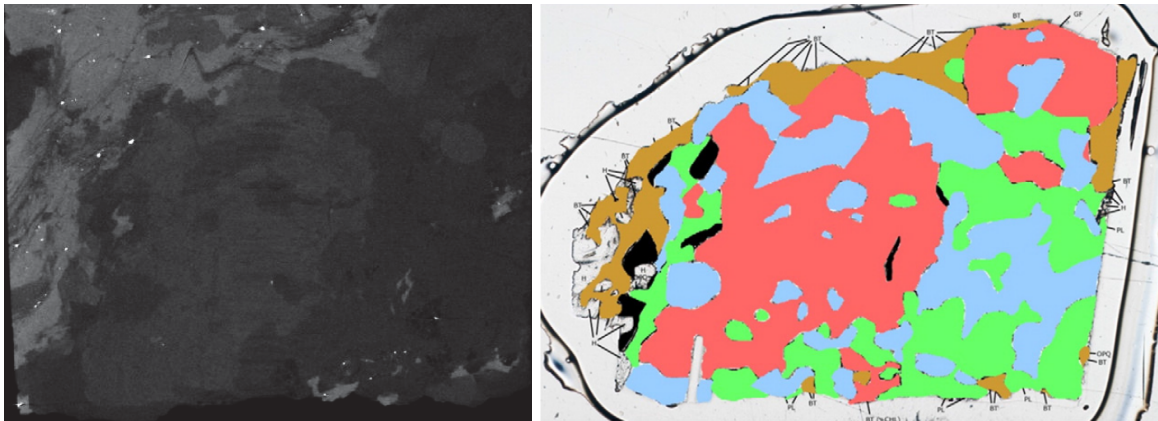
Figure 4.25: A tomographic cross-section (left panel) and the corresponding thin slice studied by polarisation microscopy (right panel) for clay fracture sample OL_KR25_56.78. The minerals are color coded in the thin slice. Quartz is blue, plagioclase is green, potassium feldspar is red, biotite is brown and accessory minerals, such as muscovite, sericite, cordierite, opaques and graphite are black.

mineral components from the tomography results (see fig. 4.22 middle panel) with polarised light microscopy. The sample needs to have features that are large and distinctive enough to be found from both images so that this method to be usable. Component 2 could not be identified, as it was missing from the thin slice, but component 3 was identified as potassium feldspar and component 4 as quartz and plagioclase, which cannot be distinguished by X-ray tomography due to being so close to each other in density.

The results for samples with a calcite fracture are shown in Table 4.1. Most samples with a calcite fracture had a low bulk porosity and no observable change in porosity close to the fracture. The only sample with a zone of altered porosity also had a high bulk porosity. There were porosity changes extending deep into the rock matrix, but they were not very drastic.

The results for samples with a clay fracture are shown in Table 4.2. Three of the four samples were very heavily altered and lacked a clear mineral orientation. All of the samples had a low bulk porosity and three of them had a clear 9–15 mm zone of altered porosity with a 3.5–6% peak porosity.

Table 4.1: Results for the samples with a calcite fracture.

Sample	OL_KR11_421.52	OL_KR13_171.55
Rock type	veined gneiss	mica gneiss
Bulk porosity	2 %	0.10 %
Zone of altered porosity (ZAP)	10 mm	0 mm
Highest porosity in ZAP	17 %	-
Zone of altered mineral densities (ZAMD)	N/A	Whole sample (10 mm)
Percentage of ZAMD altered by volume	N/A	3.50 %
Sample	OL_KR13_175.38	OL_KR13_227.40
Rock type	tonalitic gneiss	mica gneiss
Bulk porosity	0.50 %	0.30 %
Zone of altered porosity (ZAP)	0 mm	0 mm
Highest porosity in ZAP	-	-
Zone of altered mineral densities (ZAMD)	14 mm	6 mm
Percentage of ZAMD altered by volume	1.30 %	2.90 %

Table 4.2: Results for the samples with a clay fracture.

Sample	OL_KR20_421.78	OL_KR25_56.78
Rock type	veined gneiss	veined gneiss
Bulk porosity	0.50 %	0.20 %
Zone of altered porosity (ZAP)	10 mm	9 mm
Highest porosity in ZAP	3.50 %	5 %
Zone of altered mineral densities (ZAMD)	10 mm	Whole sample (15 mm)
Percentage of ZAMD altered by volume	1.50 %	40.40 %
Sample	OL_KR25_96.79	OL_KR25_482.54
Rock type	mica gneiss	veined gneiss
Bulk porosity	0.50 %	0.30 %
Zone of altered porosity (ZAP)	15 mm	0 mm
Highest porosity in ZAP	6 %	-
Zone of altered mineral densities (ZAMD)	9 mm	Whole sample (11 mm)
Percentage of ZAMD altered by volume	22.40 %	21.60 %

Table 4.3: Results for the samples with a slickensided fracture.

Sample	OL_KR13_205.65	OL_KR14_446.89
Rock type	veined gneiss	mica gneiss
Bulk porosity	0.50 %	0.10 %
Zone of altered porosity (ZAP)	0 mm	3 mm
Highest porosity in ZAP	-	0.35 %
Zone of altered mineral densities (ZAMD)	Whole sample (15 mm)	7 mm
Percentage of ZAMD altered by volume	4.80 %	5.00 %
Sample	**OL_KR14_461.91**	**OL_KR14_491.19**
Rock type	mica gneiss	mica gneiss
Bulk porosity	0.20 %	0.10 %
Zone of altered porosity (ZAP)	4 mm	8 mm
Highest porosity in ZAP	9 %	7 %
Zone of altered mineral densities (ZAMD)	12 mm	Whole sample (16 mm)
Percentage of ZAMD altered by volume	13.50 %	8.00 %

The results for samples with a slickensided fracture are shown in Table 4.3. Two of the four samples had a low bulk porosity and a 4–8 mm deep altered zone with a high peak porosity (7–9 %). All four samples had relatively deep, highly altered zones.

For best results it would be advantageous to combine the three methods used, but this has proven difficult. Especially combining tomography with microscopy would be very useful, but finding a tomographic cross-section that corresponds with a microscopic thin slice is often impossible without very careful design of sample preparation. The methods do however complement each other even when used separately. Tomography can be used to obtain 3-d information on mineral distributions and thus information on mineral alteration when the altered minerals have a different X-ray attenuation coefficient than the original mineral. Microscopy can be used to examine what kind of alteration is present in the sample and also to check if the sample is altered in a way not noticable by tomography. The 2-d porosity maps obtained through the ^{14}C-PMMA technique can help interpret both of these results and also provide a new alteration metric in the form of a porosity distribution.

The properties of rock around a water-conducting fracture depend on many uncorrelated factors and no clear pattern emerged for rock samples with a given type of fracture. The sample density had increased just as often as it had decreased near the fracture and the depths of the alteration zones varied quite much. As a general rule the samples with a calcite fracture were only slightly altered, the samples with a clay fracture were heavily altered and the samples with a slickensided fracture were somewhere in between.

5 Transport properties of rock

As mentioned in the beginning of Chapter 4 the possible transport mechanisms for radionuclides are advection in fractures and diffusion in the rock matrix. Advective transport in the fractures is the fastest and most prominent transport mechanism, but the surrounding rock matrix works to retard transport in the fractures. To model this accurately, determination of the transport properties of the rock matrix is of major importance. To this end, porosities, diffusion coefficients and permeabilities were measured for rock samples from the REPRO-niche in ONKALO, Olkiluoto. The measurements were done in gas phase in a laboratory environment. This means the measured results do not take into account any chemical effects or the effect of removing the rock from in situ environment, but it also means the measurements could be done in a much more reasonable amount of time than water phase in situ measurements and with better control over the measurement system. The gas phase results also gave valuable info for planning of in situ experiments and interpretation of their results, as the gas phase results can also be converted into the water phase by dividing them by a conversion factor of about 11600 [64], an empirical constant arising from the differences in diffusion coefficients in water and nitrogen. The correlation of different transport parameters on one another was also investigated, as well as matrix diffusion from fracture flow. In the advection - matrix diffusion experiments the measurement setup is closer to the real life scenario of fracture flow and can thus give important results for safety analysis. These gas phase measurements were included in the articles found in Appendices III and V.

Samples

The samples measured in this work were drill core samples from ONKALO, Olkiluoto, from a depth of about 400 m [139]. All measured samples had a diameter of about 41.5 mm. The samples for porosity-, through diffusion- and permeability-measurements had a length of 17 – 51 mm and the samples for advection - matrix diffusion measurements had a length of 800 – 803 mm. The samples were named after the drill core they originated from. After drilling the samples were cut with a diamond saw and the smaller samples were dried to constant weight in a vacuum at 60 °C [140]. The large advection - matrix-diffusion samples were dried for three months in a vacuum at room temperature as they were too big for an oven.

The samples consisted of veined gneiss (VGN) or pegmatitic granite (PGR). Olkiluoto VGN contains migmatites with vein-like, elongated leucosomes. The rock is very heterogeneous and isotropic due to the random nature of the leucosome veins and a big portion of alteration products. Olkiluoto PGR is leucocratic, coarse-grained rock (grain size 4–10 mm). It is weakly altered. [140, 141]. The samples along with their sizes, their rock types and the measurements performed on them are listed in Table 5.1.

Table 5.1: Dimensions, rock types and performend measurements of the samples from the REPRO-niche in ONKALO, Olkiluoto, Finland. ϵ = porosity, D_{et} = effective diffusion coefficient from through diffusion experiments, k = permeability and D_{em} = effective diffusion coefficient from advection - matrix diffusion experiments.

Sample	Diameter / mm	Length / mm	Rock type	ϵ, D_{et}, k	D_{em}
ONK-PP318 11.98-12.78	41.58	803	PGR		X
ONK-PP318 13.92-13.95	41.56	29.6	PGR	X	
ONK-PP318 13.97-14.02	41.6	47.6	PGR	X	
ONK-PP318 15.76-15.81	41.67	49.78	PGR	X	
ONK-PP318 16.87-16.92	41.4	50.4	VGN	X	
ONK-PP319 9.21-9.26	41.54	49.21	VGN	X	
ONK-PP319 9.47-9.52	41.4	45.9	VGN	X	
ONK-PP319 12.54-12.59	41.50	47.67	VGN	X	
ONK-PP319 12.70-12.75	41.4	47.9	VGN	X	
ONK-PP321 10.26-10.31	42.0	47.7	VGN	X	
ONK-PP323 18.50-18.55	41.5	49.5	VGN	X	
ONK-PP323 18.86-18.91	41.51	49.97	VGN	X	
ONK-PP323 18.94-18.97	41.48	29.0	VGN	X	
ONK-PP323 19.10-19.15	41.45	47.20	VGN	X	
ONK-PP323 19.25-20.05	41.50	800	VGN		X
ONK-PP323 20.89-20.91	41.58	20.2	VGN	X	
ONK-PP324 11.49-11.51	41.5	17.1	VGN	X	
ONK-PP326 11.42-11.44	41.4	18.4	VGN	X	
ONK-PP326 11.72-11.74	41.42	20.3	VGN	X	
ONK-PP327 12.05-12.07	41.1	17.3	VGN	X	
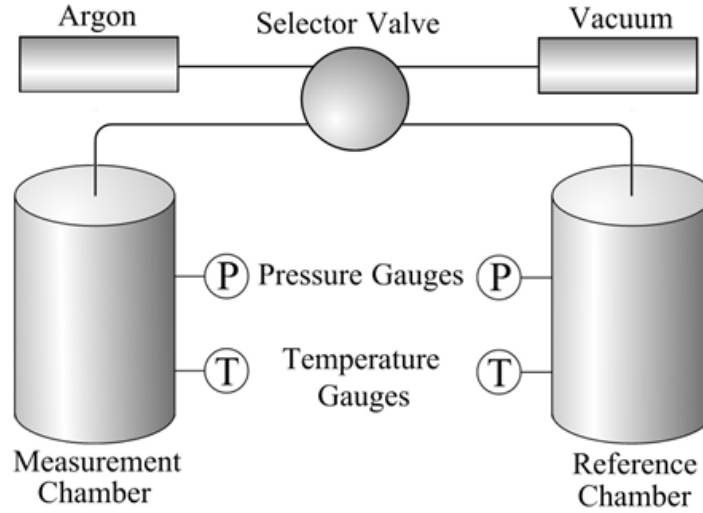
Figure 5.1: [58] A schematic layout of the pycnometer. The sample is placed in the measurement chamber and the selector valve is used to evacuate, pressurise and connect the chambers.

5.1 Porosity measurements by Ar-pycnometry

Porosity is naturally an important transport property, as transport through the geosphere can only happen through the pore network. The bulk porosity of intact rock is not an important figure for nuclide flow as that takes place mostly in fractures, but it determines the amount of stagnant pore space around the fractures where the nuclides can diffuse to and thus provides vital information on nuclide transport retardation.

The equipment used to measure porosities in this work consists of two chambers, a measurement chamber and a reference chamber. A schematic of the equipment is presented in fig. 5.1. Argon is used here because it is nonreactive, penetrates easily into small pores, is less prone to leaks than helium and satisfies the equation of state of ideal gas quite well [142]. A sample is placed in the measurement chamber and both chambers are evacuated until a gauge vacuum of -95 kPa is reached. The reference chamber is then pressurised with argon gas to a gauge pressure of 100 kPa. Finally the chambers are connected. The pressure and temperature of both chambers are measured in all steps after stabilisation. An example measurement of pressure in the reference chamber is shown in fig. 5.2. The grain volume and thus the porosity of the sample can be determined by using the equation of state of ideal gas, which eventually gives

$$V_g = V_M - V_R \frac{(P_R T_M T_V - P_M T_V T_R)}{(P_M T_V T_R - P_V T_M T_R)}, \tag{5.1}$$

where V_g is the grain volume of the sample, V_M and V_R are the volumes of the measurement and reference chambers, respectively, P_V and T_V are the pressure and temperature, respectively, of the reference chamber after evacuation, P_R and T_R are the same quantities of the reference chamber after pressurisation and P_M and T_M are the same quantities of the measurement chamber after connecting the chambers. The volumes of the chambers are determined by performing the measurement with two calibration samples of known grain volumes and solving from Eq. (5.1). Porosity ϵ can then be
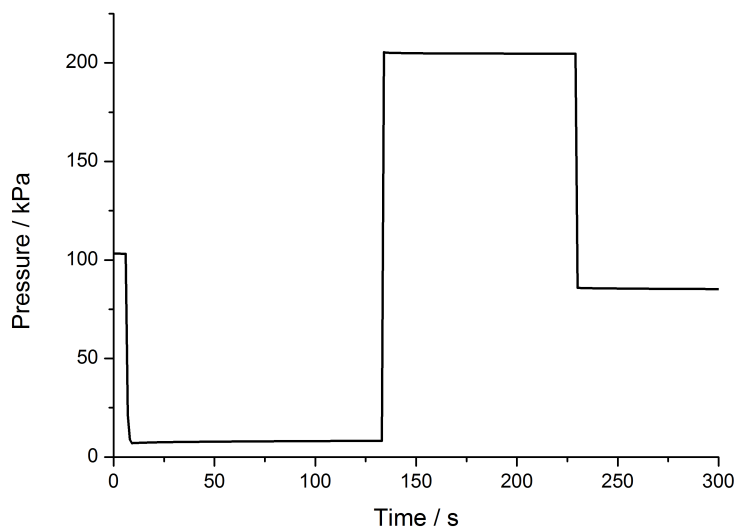
Figure 5.2: Typical variation of pressure in the reference chamber during a pycnometer measurement. First both chambers are evacuated, then the reference chamber is pressurised and finally the chambers are connected.

obtained from

$$\epsilon = \frac{V_b - V_g}{V_b},\tag{5.2}$$

where V_b is the bulk volume of the sample. In this work V_b was obtained by the water immersion method, where a sample is weighed outside of water and immersed in water, and the bulk volume is obtained by the Archimedes principle. To account for water penetrating the sample pores during immersion the weight of the sample was monitored with a computer and extrapolated to the moment of immersion. Ion-exchanged water was used to decrease bubble formation and the temperature of the water was monitored for accurate density calculation. An example of the weight and temperature measurements is shown in fig. 5.3. Previous studies have shown that measurements in the gas and water phase yield equivalent results [143, 144] but the results between laboratory experiments and in situ experiments can differ [76–79]. This is mainly due to stress release of the samples, but also due to sampling procedures and sample preparation, which can increase the porosity of the laboratory samples.

5.2 Through diffusion and permeability measurements

Through diffusion is not an important means of transport for radionuclides, although it can be used to quickly obtain accurate diffusion coefficients that can be used to estimate retardation via matrix diffusion. The same experimental setup can also be used to measure permeability, another useful parameter for transport modelling and estimation of the bedrock transmissivity.

The equipment used for through diffusion and permeability measurements [60, 61, 63, 64] uses nitrogen as the carrier and helium as the tracer. The equipment consits of a sample holder, an injection valve, a He-mass spectrometer, a gas-flow meter, two pressure gauges, and several valves that also
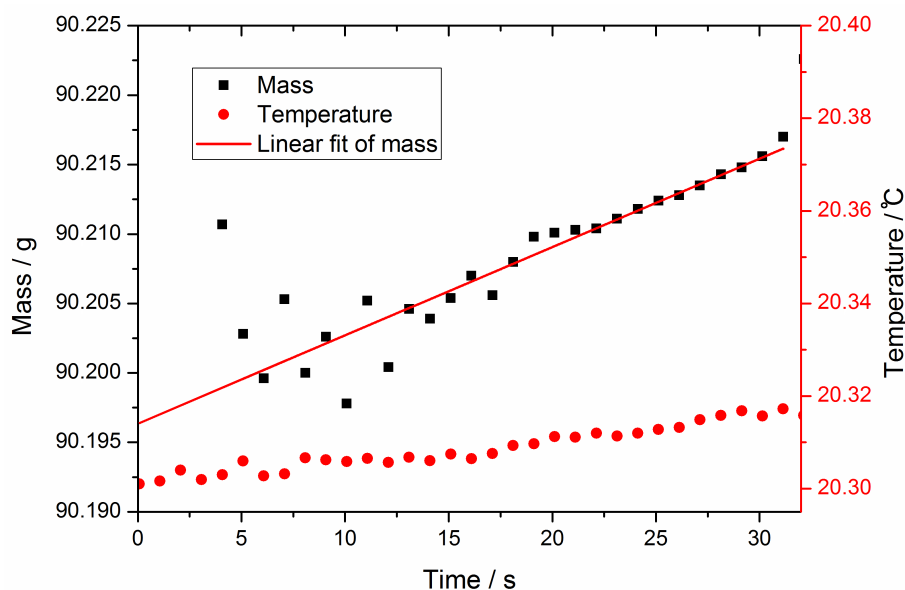
Figure 5.3: A typical time dependence of sample weight as a function of time, expressed in the units of mass, along with a linear fit. Fluctuations in the beginning arise from leaving air bubbles and slight swinging of the sample in water.

connect the setup to nitrogen and helium outlets and a vacuum pump (see fig. 5.4). The injection valve can be used with several injection loops of different volumes. The selection valve is used to connect the injection chamber to the injection valve, the vacuum pump or directly to the helium source, which is done in the permeability measurements. The He-mass spectrometer data is recorded on a PC using a LabView-based software. The sample is attached to the sample holder using a commercial butyl rubber sealant band in such a way that only the flat ends of a cylindrical sample are left in contact with the measurement. Blank measurements showed that the leaks through the sealant were smaller than the detection limit of the mass-spectrometer and could thus be neglected.

In the through diffusion measurements the injection chamber was first connected to the vacuum pump and evacuated to -95 kPa gauge. A 5 ml loop connected to the injector was filled with helium. The injector was then used to connect the loop to the nitrogen source and the injection chamber, causing the helium to be sucked to the injection chamber and replaced by nitrogen. Integration of the nitrogen flow data acquired from the flow meter (Sierra SmartTrak 100) gives a good estimate of the volume of the injected helium. The helium then diffused through the sample into the flushing chamber which was constantly flushed with nitrogen, which was measured with a He-mass spectrometer (Leybold UL 200). A pressure gauge connected to the flushing chamber was used to ensure that the nitrogen pressure was slightly (5–10 kPa) above the ambient pressure, but not so much as to create a disturbing advection flux proportional to the induced pressure gradient across the sample. This slight over-pressure guaranteed that no helium was leaked into the flushing chamber from the laboratory, whose air contained helium at a ppm level. Possible out-diffusion of helium from the flushing chamber was of no concern, as the detection efficiency of the spectrometer requires a correction factor to the helium flux for data analysis and this correction factor includes the effects of possible out-diffusion. The pressure gauge, flow-rate, and He-mass spectrometer data were all recorded on PC for later analysis.

In the permeability measurements the helium source was connected directly to the injection chamber
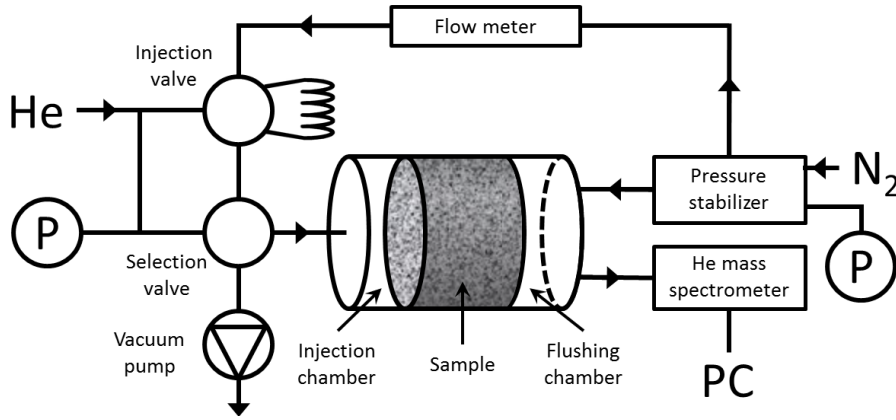
Figure 5.4: A layout of the through diffusion equipment. It consists of a sample holder, an injection valve, a He-mass spectrometer, a gas-flow meter, two pressure gauges (P), and several valves that also connect the setup to nitrogen (N_2) and helium (He) outlets and a vacuum pump.

with the selector valve, and the pressure in both chambers was controlled while flushing the flushing chamber with nitrogen. Pressure of the injection chamber was increased by regular increments, and all pressures and the helium flow were measured after all these values were stabilised. Pressure difference across the sample varied from 20 kPa to 90 kPa.

Analysis

Modelling of the through diffusion measurements was based on the solution of the Fickian diffusion equation with appropriate initial and boundary conditions. The sample geometry and reflective boundary conditions in the transverse directions made it possible to use a one-dimensional approximation of this equation.

To find the helium flow as a function of time, its one-dimensional diffusion across the sample is considered, and its density $\rho(x,t)$ is defined such that $x = 0$ is the sample surface in the flushing chamber and $x = L$ is the sample surface in the injection chamber. The diffusion equation can be expressed in the form

$$\frac{1}{D_e}\frac{\partial \rho}{\partial t} = \frac{\partial^2 \rho}{\partial x^2},$$

(5.3)

where D_e is the effective diffusion coefficient of helium in the sample whose pores are filled with nitrogen. Flushing effectively removes the helium from the flushing chamber, so that $\rho(0,t) = 0$. Conservation of mass gives the other boundary condition, as all tracer molecules that leave the injection chamber must enter the sample, so that

$$V \cdot \frac{\partial \rho}{\partial t}(L,t) = -\epsilon A \cdot D_e \frac{\partial \rho}{\partial x}(L,t),$$

(5.4)

where V is the volume of the injection chamber, ϵ is the porosity of the sample, and A is the area of its cross-section. The initial condition is zero concentration inside the sample and $\rho_0 = \frac{m_0}{V}$ at $x = L$, where m_0 is the mass of the injected helium. The solution of Eqs (5.3) and (5.4) with these initial

and boundary conditions can be written in the form of a series expansion [145]

$$\rho(x,t) = \rho_0 \sum_{n=1}^{\infty} \frac{\sin(\frac{\lambda_n x}{L})}{\sin \lambda_n} \cdot \frac{2LH}{\lambda_n^2 + (LH)^2 + LH} e^{-\frac{D_e \lambda_n^2}{\rho L^2} t}, \tag{5.5}$$

where $H = \frac{\epsilon A}{V}$ and $0 < \lambda_1 < \lambda_2 < ...$ are the positive roots of the equation

$$\lambda \tan \lambda = LH. \tag{5.6}$$

Using conservation of mass, $\dot{m} = \frac{dm}{dt} = D_e \frac{\partial \rho}{\partial x}(0,t) \cdot \epsilon A$, the helium flux across the sample can be expressed in the form

$$\frac{\dot{m}}{m_0} = \sum_{n=1}^{\infty} \frac{\lambda_n}{\sin \lambda_n} \cdot \frac{2D_e H^2}{\rho \cdot \left(\lambda_n^2 + (LH)^2 + LH \right)} e^{-\frac{D_e \lambda_n^2}{\rho L^2} t}, \tag{5.7}$$

where $H = \frac{\epsilon A}{V}$. This equation can be used to fit the measured breakthrough curve with the effective diffusion coefficient and optionally porosity as the fitting parameters. The effective diffusion coefficient is mainly determined by the late-time behaviour of the breakthrough curve, which is rather insensitive to small details of the system. Porosity is determined by the main pulse of the breakthrough curve, but the measurement is more accurate if porosity is determined by a separate measurement, e.g. like described in section 5.1. The porosity can then be fixed and effective diffusion coefficient used as the only fitting parameter.

In the permeability measurement a controlled pressure difference is created across the sample, which induces a flux of helium through the sample. To derive an equation for this flux, the differential form of Darcy's law [146] is first examined:

$$\bar{v} = -\frac{k}{\mu} \nabla (P - \rho \bar{g}), \tag{5.8}$$

where $\bar{v} = \frac{\partial Q}{\partial A}$ is the velocity of the gas averaged over a given cross-section of area A, Q is its volume flow, k is the permeability, μ the dynamic viscosity, and P the pressure of the tracer gas of density ρ, and $\bar{g}$ is the acceleration caused by gravity. Since gases are compressible, ρ is not constant, as is the case in the liquid phase. However, in steady state at constant temperature, the product of velocity and pressure is constant throughout the sample. Thus the velocity of the gas at the surface of the flushing chamber v_2 is given by

$$v_2 = \frac{k}{\mu} \frac{\left(P_2^2 - P_1^2 \right)}{2P_2 L}, \tag{5.9}$$

where P_1 is the pressure in the flushing chamber and P_2 that in the injection chamber. Using now $v = \frac{dQ}{dA}$ and integrating over the cross-sectional area on both sides of the above equation, one finds that

$$Q = Q_{diff} + \frac{kA}{\mu L} \frac{\left(P_2^2 - P_1^2 \right)}{2P_2}, \tag{5.10}$$

where Q_{diff} is the flux due to diffusion.

5.3   Advection - matrix diffusion measurements

Advection - matrix diffusion measurements were done in gas phase with the measurement setup shown in fig. 5.4 with a different kind of sample holder and the selection valve connecting both gas
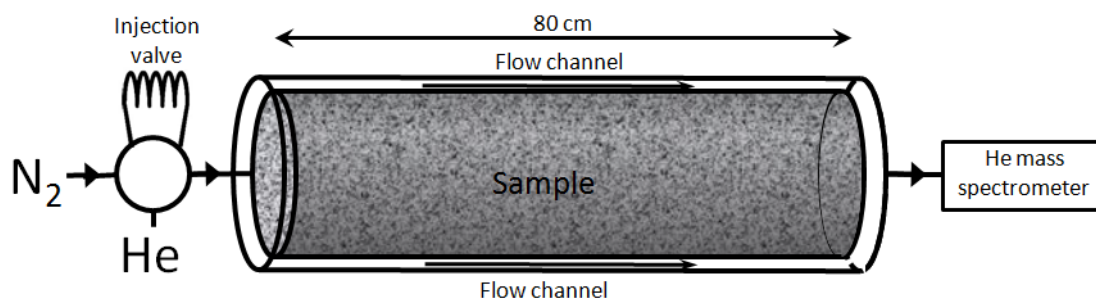
Figure 5.5: Layout of the advection - matrix diffusion system. It consisted of a sample holder, an injection valve, a He–mass spectrometer and several valves that also connected the setup to nitrogen and helium outlets. The gas-flow meter is not shown in this figure.

supplies to the injection valve. The aim was to help water phase in situ measurements as well as planned gas phase in situ measurements [80]. A schematic of the equipment in this measurement is shown in fig. 5.5. The sample holder was self made and designed to keep the sample centered in a metal tube, leaving a thin, uniform flow channel $(0.2 - 0.3$ mm$)$ around it. In order to help the flow fill properly the whole flow channel, a stainless-steel capillary tube (inner diameter 0.9 mm) and a special input flange were used, from which the flow spread uniformly to the cylindrical channel. The output flange was identical with the input flange. The ends of the sample were sealed with a commercial butyl rubber sealant and aluminium caps to only allow diffusion from the flow channel. The used He-mass spectrometer had a measuring range of 9 decades $(0.1 - 5 \cdot 10^{-11} \frac{\text{mbar} \cdot \text{l}}{\text{s}})$, which enabled measurement of the relatively-high He concentrations at the early stages of the measurement, as well as the low concentrations at its later stages. Since the mass spectrometer required a rough vacuum, a throttle was installed before the spectrometer, so as to keep the rest of the measurement setup as close to the ambient pressure as possible. The gas-flow meter/controller was used to simultaneously control and measure the nitrogen flow in the range 40–50 ml/min.

After placing a sample in the sample holder, a steady, uniform nitrogen flow was produced in the flow channel around it. The pressure from the nitrogen source was set 5–10 kPa above the ambient pressure, and the throttle was set as tight as possible to allow a sufficient flow rate, while maintaining the void inside the spectrometer as well as possible. The gas-flow controller was finally used to set the flow rate exactly to the desired value. When the nitrogen flow was stable, the injection loop was filled with helium which was then injected into the flow. This injection caused a small negative peak in the flow-rate data, which could be used to track the time step of the injection. The amount of helium in the nitrogen was tracked during the whole measurement and saved for analysis.

Mathematical model

In this section the mathematical model that is used to interpret the measured breakthrough curves is described. The geometry used in the mathematical model consisted of a thin (1D) flow channel around a porous cylinder. The cylinder can be homogeneous, layered or divided into sectors of different properties, as shown in fig. 5.7. The sectors can also be layered. The sectors are divided evenly around the cylinder to ensure a well-mixed flow, but are presented undivided here for clarity. The outer wall of the flow channel is impermeable. The solution is first obtained for a general case (see fig. 5.6, then for a homogeneous cylinder and then for a heterogeneous cylinder).
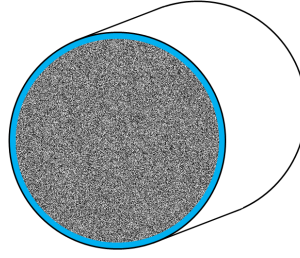
Figure 5.6: A schematic presentation of the measurement geometry for a general porous cylinder. The flow channel is shown in blue.

For tracer transport in an advection-diffusion system, the tracer concentration in the flow channel (C_f) is described by an advection-diffusion equation and in the porous matrix (C_m) by a diffusion equation:

$$\frac{\partial C_f}{\partial t} + \nabla \cdot (C_f\, v) - D_0\, \Delta C_f = 0,$$
$$\frac{\partial C_m}{\partial t} - \nabla \cdot (D_p\, \nabla C_m) = 0,$$

(5.11)

where v is the velocity of the flow, D_p is the pore-diffusion coefficient of the tracer in the matrix, and D_0 is the diffusion coefficient of the tracer in the fluid. Transmission conditions between the flow channel and the porous matrix are given by

$$C_f = C_m, \quad \text{and} \quad D_0\, \frac{\partial C_f}{\partial n} = \epsilon\, D_p\, \frac{\partial C_m}{\partial n},$$

(5.12)

where ϵ is the porosity of the matrix. The outer wall of the flow channel is impermeable, so the normal derivative of C_f vanishes at the outer wall of the flow channel:

$$\frac{\partial C_f}{\partial r} = 0,$$

(5.13)

In the following some simplifying assumptions are made such that the system can be solved analytically with appropriate initial and boundary conditions.

Homogeneous matrix

The matrix is assumed to be homogeneous, *i.e.*, D_p is constant. The system is also assumed to be rotationally symmetric. Furthermore, as advection along the channel is much faster than transport by diffusion in the matrix, we can assume that diffusion in the matrix is radial. By taking the radial average over the flow channel and assuming that the fluid is 'well-mixed', *i.e.*, that the tracer concentration in the channel is constant in the cross sections perpendicular to the direction of the flow channel (x direction), it is found that

$$\frac{\partial C_f}{\partial t}(x,t) + v\, \frac{\partial C_f}{\partial x}(x,t) - D_0\, \frac{\partial^2 C_f}{\partial x^2}(x,t) = -\frac{2\epsilon D_p a}{2ab + b^2}\, \frac{\partial C_m}{\partial r}(x,a,t)$$
$$\frac{\partial C_m}{\partial t}(x,r,t) - D_p \left(\frac{\partial^2 C_m}{\partial r^2}(x,r,t) + \frac{1}{r}\, \frac{\partial C_m}{\partial r}(x,r,t) \right) = 0.$$

(5.14)

Here a is the radius of the matrix and b is the aperture of the flow channel. These equations can also be applied in the case of laminar flow with a parabolic velocity profile across the flow channel. In this

case D_0 must be replaced by an effective diffusion coefficient that includes Taylor dispersion [147], and v is the cross sectional average of the flow velocity. The situation in which a short pulse (mass M) of the tracer is injected into the beginning ($x = 0$) of the channel at time $t = 0$, is described by the boundary and initial conditions

$$C_m(x, a, t) = C_f(x, t), \quad \frac{\partial C_m}{\partial r}(x, R, t) = 0, \quad C_m(x, r, 0) = 0$$

$$C_f(0, t) = \frac{M}{\pi(a^2 - (a-b)^2)v} \delta(t), \quad C_f(x, 0) = 0. \tag{5.15}$$

The boundary condition for C_f at the end of the channel ($x = L$) is not set, but the system is considered in an unbounded domain, $x > 0$, with a 'physical boundary condition' at infinity,

$$\lim_{x \to \infty} C_f(x, t) = 0. \tag{5.16}$$

What is of interest is the breakthrough curve, *i.e.*, $C_f(L, t)$. With the substitution

$$\tau = \frac{t\,v}{L}, \qquad \xi = \frac{x}{L}, \qquad \rho = \frac{r}{a}$$

$$C(\xi, \tau) = \frac{\pi(2ab + b^2)L}{M} C_f(x, t), \tag{5.17}$$

$$C_M(\xi, \rho, \tau) = \frac{\pi(2ab + b^2)L}{M} C_m(x, r, t)$$

equations (5.14), (5.15) and (5.16) can be expressed in a dimensionless form,

$$\frac{\partial C}{\partial \tau}(\xi, \tau) + \frac{\partial C}{\partial \xi}(\xi, \tau) - \mu^2 \frac{\partial^2 C}{\partial \xi^2}(\xi, \tau) = -\frac{\lambda}{\kappa} \frac{\partial C_m}{\partial \rho}(\xi, 1, \tau)$$

$$\frac{\partial C_m}{\partial \tau}(\xi, \rho, \tau) - \frac{1}{\kappa^2} \left(\frac{\partial^2 C_m}{\partial \rho^2}(\xi, \rho, \tau) + \frac{1}{\rho} \frac{\partial C_m}{\partial \rho}(\xi, \rho, \tau) \right) = 0 \tag{5.18}$$

$$C_m(\xi, 1, \tau) = C(\xi, \tau), \quad C_m(\xi, \rho, 0) = 0$$

$$C(0, \tau) = \delta(\tau), \quad C(\xi, 0) = 0, \quad \lim_{\xi \to \infty} C(\xi, \tau) = 0,$$

where the dimensionless parameters are

$$\lambda = \frac{2\epsilon a}{2ab + b^2} \sqrt{\frac{D_p L}{v}}, \quad \kappa = a\sqrt{\frac{v}{D_p L}}, \quad \mu = \sqrt{\frac{D_0}{Lv}}. \tag{5.19}$$

For a fixed ξ, the diffusion equation can be solved for C_m by separating the variables. Substituting that solution into the first equation in Eq. (5.18) results in a closed integro-differential equation - *the matrix diffusion equation* - for C,

$$\frac{\partial C}{\partial \tau}(\xi, \tau) + \frac{\partial C}{\partial \xi}(\xi, \tau) - \mu^2 \frac{\partial^2 C}{\partial \xi^2}(\xi, \tau) = -\lambda \int_0^\tau \Lambda(\tau - \sigma) \frac{\partial C}{\partial \sigma}(\xi, \sigma)\, d\sigma, \tag{5.20}$$

with

$$C(\xi, 0) = 0, \quad C(0, \tau) = \delta(\tau), \quad \lim_{\xi \to \infty} C(\xi, \tau) = 0, \tag{5.21}$$

where

$$\Lambda(\tau) = \frac{2}{\kappa} \sum_{n=1}^\infty \gamma_n \cdot e^{-\frac{\alpha_n^2}{\kappa^2}\tau}. \tag{5.22}$$

Here eigenvalues α_i are the positive zeros of the Bessel function J_0 and the coefficients $\gamma_n = 1$. The matrix diffusion equation Eq. (5.20) can be solved using the Laplace transform, see [89]. The breakthrough curve can be expressed in the form

$$C(\tau) = \frac{1}{\pi} \int\limits_0^\infty e^{-G(x)-\tau x} \left(\cos(\tau x - H(x)) - \sin(\tau x - H(x)) \right) dx, \tag{5.23}$$

where

$$G(x) = \frac{\sqrt{\sqrt{(1+4\mu^2(f(x)-x))^2+(4\mu^2(h(x)+x))^2}+1+4\mu^2(f(x)-x)} - \sqrt{2}}{2\sqrt{2}\mu^2},$$
$$H(x) = \frac{\sqrt{\sqrt{(1+4\mu^2(f(x)-x))^2+(4\mu^2(h(x)+x))^2}-1-4\mu^2(f(x)-x)}}{2\sqrt{2}\mu^2}, \tag{5.24}$$

and

$$f(x) = \frac{2\lambda}{\kappa} \sum_{n=1}^\infty \gamma_n \cdot \frac{2x^2 - x\alpha_n^2/\kappa^2}{(\alpha_n^2/\kappa^2 - x)^2 + x^2}$$
$$h(x) = \frac{2\lambda}{\kappa} \sum_{n=1}^\infty \gamma_n \cdot \frac{x\alpha_n^2/\kappa^2}{(\alpha_n^2/\kappa^2 - x)^2 + x^2}. \tag{5.25}$$

Matrix with two layers

Now another coaxial layer is added to the cylinder (interface at radius $r = R$) with different transport properties (modelling a cylinder composed of two layers with porosities ϵ_1 and ϵ_2 and pore diffusion coefficients D_{p1} and D_{p2}), respectively, see fig. 5.7, left panel; such a system can be used, e.g., to model an excavation disturbed zone).
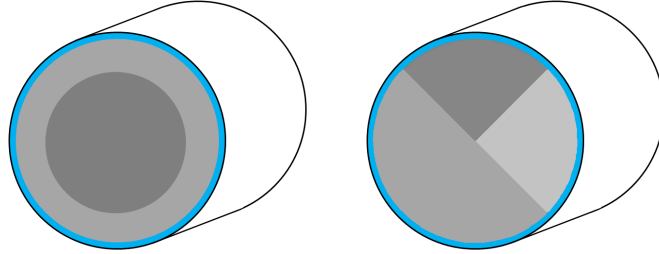
Figure 5.7: Schematic representation of the measurement geometry for a layered cylinder (left panel) and a sector cylinder (right panel). The sectors are divided evenly around the cylinder to ensure a well mixed flow, but are presented undivided here for clarity. The flow channel is shown in blue and different levels of grey describe layers with different transport properties.

In this case the model is the same, except that the diffusion equation for C_m in Eq. (5.14) is replaced by the equation

$$\frac{\partial C_m}{\partial t}(x,r,t) - D_{p1} \left(\frac{\partial^2 C_m}{\partial r^2}(x,r,t) + \frac{1}{r} \frac{\partial C_m}{\partial r}(x,r,t) \right) = 0, \quad R < r < a$$
$$\frac{\partial C_m}{\partial t}(x,r,t) - D_{p2} \left(\frac{\partial^2 C_m}{\partial r^2}(x,r,t) + \frac{1}{r} \frac{\partial C_m}{\partial r}(x,r,t) \right) = 0, \quad 0 < r < R, \tag{5.26}$$

with the transmission conditions

$$C_m(x, R+, t) = C_m(x, R-, t)\epsilon_1 D_{p1} \frac{\partial C_m}{\partial r}(x, R+, t) = \epsilon_2 D_{p2} \frac{\partial C_m}{\partial r}(x, R-, t). \qquad (5.27)$$

The breakthrough curve can be built in a similar manner as with the homogeneous model. Also in this case a matrix diffusion equation of the same form Eq. (5.20) is obtained, but with

$$\gamma_n = \frac{4}{4 + \pi^2 \alpha_n^2 \rho_0^2 \nu_n}, \qquad (5.28)$$

where

$$\nu_n = \left(\frac{1}{\epsilon} - 1\right) (Y_0(\alpha_n) J_0(\alpha_n \rho_0) - J_0(\alpha_n) Y_0(\alpha_n \rho_0))^2 \\ (\beta^2 \epsilon - 1) (J_0(\alpha_n) Y_1(\alpha_n \rho_0) - Y_0(\alpha_n) J_1(\alpha_n \rho_0))^2, \qquad (5.29)$$

and eigenvalues α_n are the positive roots of the equation

$$Y_0(\alpha) (J_0(\alpha \rho_0) J_1(\alpha \beta \rho_0) - \epsilon \beta J_0(\alpha \beta \rho_0) J_1(\alpha \rho_0)) \\ - J_0(\alpha) (Y_0(\alpha \rho_0) J_1(\alpha \beta \rho_0) - \epsilon \beta J_0(\alpha \beta \rho_0) Y_1(\alpha \rho_0)) = 0. \qquad (5.30)$$

Here the dimensionless parameters are

$$\lambda = \frac{2\epsilon_1 a}{2ab + b^2} \sqrt{\frac{D_{p1}L}{v}}, \quad \kappa = a \sqrt{\frac{v}{D_{p1}L}}, \quad \mu = \sqrt{\frac{D_0}{Lv}} \beta = \sqrt{\frac{D_{p1}}{D_{p2}}}, \quad \epsilon = \frac{\epsilon_1}{\epsilon_2}, \quad \rho_0 = \frac{R}{a}, \qquad (5.31)$$

Multi-component matrix

Lastly an analytically solvable 'toy model' for a rock matrix is considered, which consists of several minerals with different diffusion properties, see fig. 5.7, right panel. If the flow is well mixed, and if transport in each mineral component can be described independently with radial diffusion, then the system can be mathematically described such that the flux term on the right-hand side of the first equation in Eq. (5.14) is replaced by a sum of fluxes from each component:

$$\frac{\partial C_f}{\partial t}(x, t) + v \frac{\partial C_f}{\partial x}(x, t) - D_0 \frac{\partial^2 C_f}{\partial x^2}(x, t) = -\sum_{j=1}^{n} \frac{2\epsilon_j p_j D_p^{(j)} a}{2ab + b^2} \frac{\partial C_m^{(j)}}{\partial r}(x, a, t), \qquad (5.32)$$

where p_j is the portion of component j at the surface of the flow channel. Concentration of the tracer $C_m^{(j)}$ in component j is described by radial diffusion (or two-layer diffusion) with the initial and boundary conditions as in Eq. (5.15) and Eq. (5.16). These assumptions are valid if it is assumed that each component is a sector in the cylinder (with one or two layers), and the fluxes between different components are not taken into account, and different components of varying properties are distributed 'uniformly' at the wall of the flow channel (see fig. 5.7). Grains of different minerals are assumed homogeneous, and each grain can correspond to a sector in the cylinder (or a layer in a two-layer cylinder), and angular and axial diffusion between different grains is ignored. This model is good at short times, when fluxes between different components of the rock are small in comparison with the flux between the rock and the flow channel. In practice it seems to work quite well for modelling the breakthrough curves of heterogeneous flow channels (rock matrices). The above matrix diffusion equations can easily be generalised into this case.
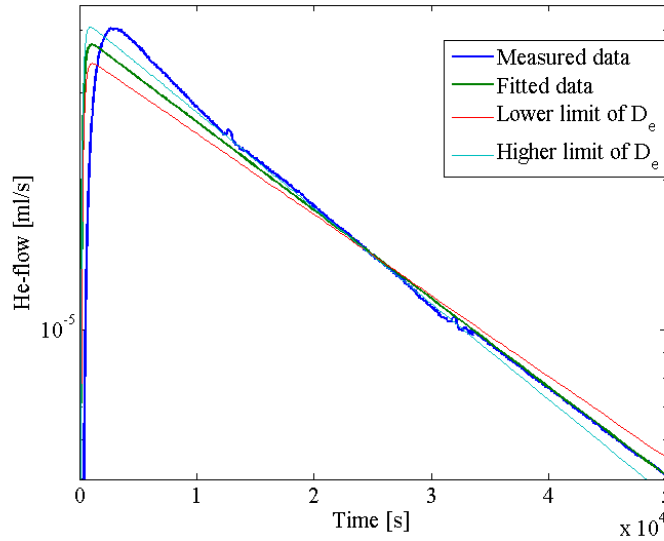
Figure 5.8: A typical through diffusion breakthrough curve and its fit by Eq. (5.7) together with the confidence limits. Depicted sample is ONK-PP318 15.76-15.81 with $D_e = (5.7 \pm 0.5)\frac{m^2}{s}$.

5.4   Porosity, through diffusion and permeability results

The porosity results are listed in Table 5.3. The obtained values were 0.44–0.63 % for PGR and 0.19–2.9 % for VGN. The results are of the same magnitude as measured before for Olkiluoto samples, such as in the article of Appendix I, except for the highest values for VGN.

The effective diffusion coefficients were obtained from the measured breakthrough curves by fitting them by Eq. (5.7). Figure 5.8 shows a typical through diffusion breakthrough curve (sample ONK-PP318 15.76-15.81) together with its fit. Evacuation of the injection chamber before the measurement (i.e., $t = 0$) causes also evacuation of the pore space of the sample close to that chamber so that in fact helium enters the sample more quickly than assumed in the solution of the diffusion equation, which causes the measured breakthrough curve to rise above the fitted one. As D_e is mainly determined by the late-time behaviour of this curve, however, is not affected by this feature. The effective diffusion coefficients were $3.2 \cdot 10^{-9} - 8.2 \cdot 10^{-9}$ m^2/s for PGR and $5.0 \cdot 10^{-10} - 6.7 \cdot 10^{-9}$ m^2/s for VGN. Full results are listed in Table 5.3. The results were of the same magnitude as measured before for Olkiluoto samples [148].

It was also analysed if Knudsen diffusion [149–151] affects the results. To this end, the diffusion coefficient of sample ONK-PP323 18.86-18.91 that was estimated to have a lot of pores with small apertures due to its high contents of biotite [140], was measured at many different gas pressures. As the mean free path of the tracer in a gas is linearly related to the pressure of the gas, increasing ambient pressure decreases this mean free path, and should thus reduce the possible effect of Knudsen diffusion. If Knudsen diffusion were significant in the measurement of diffusion coefficient, it should change when the pressure is changed. The results of such a measurement, shown in Table 5.2, indicate that only small changes appear in the diffusion coefficient when the pressure is changed. These changes can be attributed to uncertainties in the measurements.

Table 5.2: Diffusion coefficient of the tracer (He) for a varying pressure of the carrier gas (N_2).

Gauge pressure (kPa)	$D_e \left(10^{-10} \frac{m^2}{s} \right)$
6	7.6 ± 0.8
30	9.0 ± 0.9
60	8.0 ± 0.9
97	9.0 ± 0.9
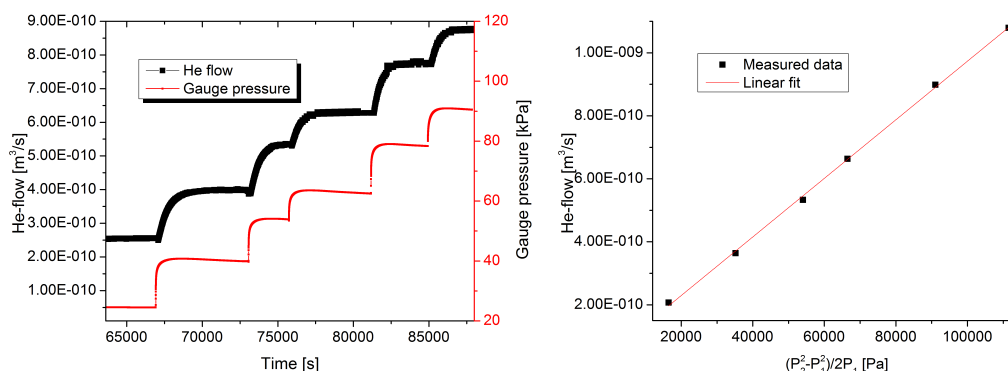
Figure 5.9: Left panel: Gauge pressure of the injection chamber as a function of time (thin curve) together with the corresponding breakthrough curve (thick curve). Right panel: Fit of volume flow at the plateaus shown in left panel by Eq. (5.10). Gauge pressure in the flushing chamber was nearly constant (about 10 kPa). Depicted sample is ONK-PP318 13.97-14.02. The linear fit had an R value of 1.00.

Figure 5.9 shows a typical breakthrough curve for the permeability measurements (sample ONK-PP318 13.97-14.02) along with the corresponding pressure of the injection chamber during the measurement. Permeability was obtained from this curve by plotting the helium flux (at the plateaus) against the pressure term in Eq. (5.10) and dividing the slope of the resulting straight line by $\frac{A}{\mu l}$ (see Eq. (5.10)). An example of this 'Darcy plot' is also shown in fig. 5.9. The linear behaviour seen in the Darcy plot shows that the Klinkenberg effect [149], which is an effect similar to Knudsen diffusion that affects permeability, is not significant in these measurements, as it would make the permeability pressure-dependent and remove the linearity. The permeabilities were $5.9 \cdot 10^{-19} - 6.4 \cdot 10^{-18}$ m^2 for PGR and $1.4 \cdot 10^{-20} - 8.6 \cdot 10^{-17}$ m^2 for VGN. Full results are again listed in Table 5.3. The results were of the same magnitude as those measured before for Olkiluoto samples [148], except for the highest VGN results.

Correlation of transport parameters

The measured porosities, effective diffusion coefficients and permeabilities from sections 5.1 and 5.2 are listed in Table 5.3. To try to find out if any of the three properties are correlated, the measured data was combined with several previous results [64, 148, 152–154] and the properties were plotted

Table 5.3: Measured porosities ϵ, effective diffusion coefficients D_e, permeabilities k, and rock types of the REPRO samples. Errors are 1 σ

Sample	ϵ / %	D_e / $10^{-9}\frac{\mathrm{m}^2}{\mathrm{s}}$	k / $10^{-19}\mathrm{m}^2$	Rock type
ONK-PP318 13.92-13.95	0.6 ± 0.3	8.2 ± 0.8	860 ± 70	PGR
ONK-PP318 13.97-14.02	0.63 ± 0.05	3.2 ± 0.6	64 ± 1	PGR
ONK-PP318 15.76-15.81	0.44 ± 0.14	5.7 ± 0.5	5.9 ± 0.2	PGR
ONK-PP318 16.87-16.92	0.70 ± 0.05	6.7 ± 0.7	9 ± 1	VGN
ONK-PP319 9.21-9.26	0.34 ± 0.14	2.0 ± 0.2	1.3 ± 0.2	VGN
ONK-PP319 9.47-9.52	2.4 ± 0.2	1.4 ± 0.3	6 ± 1	VGN
ONK-PP319 12.54-12.59	0.77 ± 0.15	2.8 ± 0.2	1.1 ± 0.1	VGN
ONK-PP319 12.70-12.75	0.60 ± 0.14	3.8 ± 0.5	49 ± 5	VGN
ONK-PP321 10.26-10.31	0.55 ± 0.14	1.9 ± 0.7	39 ± 1	VGN
ONK-PP323 18.50-18.55	0.82 ± 0.13	3 ± 1	11.3 ± 0.1	VGN
ONK-PP323 18.86-18.91	1.24 ± 0.14	0.58 ± 0.05	0.2 ± 0.1	VGN
ONK-PP323 18.94-18.97	2.7 ± 0.3	5.4 ± 0.5	53 ± 5	VGN
ONK-PP323 19.10-19.15	0.7 ± 0.2	0.50 ± 0.05	0.14 ± 0.02	VGN
ONK-PP323 20.89-20.91	0.19 ± 0.08	0.8 ± 0.1	0.9 ± 0.1	VGN
ONK-PP324 11.49-11.51	1.02 ± 0.05	0.8 ± 0.1	3.6 ± 0.4	VGN
ONK-PP326 11.42-11.44	2.9 ± 0.1	1.4 ± 0.1	2.0 ± 0.2	VGN
ONK-PP326 11.72-11.74	0.68 ± 0.08	1.1 ± 0.1	9.5 ± 0.2	VGN
ONK-PP327 12.05-12.07	0.7 ± 0.1	1.2 ± 0.1	0.2 ± 0.1	VGN

as a function of each other, as shown in Figs 5.10 - 5.12.

It seems that the porosities and effective diffusion coefficients are slightly correlated. In general, the effective diffusion coefficient of the sample increases as its porosity is increased. On the average data points roughly follow a power law function,

$$y = a \cdot x^b, \tag{5.33}$$

where a and b are fitting parameters, suggesting a weak correlation with, however, a rather large variation. Such a correlation was not observed for the REPRO samples alone. Archie's law with suitable Parkhomenko coefficients [70], $D_e = 0.71 \cdot D_{He} \cdot \epsilon^{1.58}$ with $D_{He} = 6.75 \cdot 10^{-5}\frac{\mathrm{m}^2}{\mathrm{s}}$ the effective diffusion coefficient of helium in nitrogen [155], also seemed to roughly agree with the data of fig. 5.10. However the R-value for $\log(\epsilon)$ vs $\log(D_e)$ was only 0.50, indicating weak correlation. A clear difference between the results for samples from drill core ONK-PP318 and those for other REPRO samples existed: Samples from ONK-PP318 had a systematically lower porosity and higher effective diffusion coefficient than other REPRO samples. These differences can be explained by structural and mineralogical differences of the samples. Samples from ONK-PP318 were typically PGR, and they had grain boundaries and intragranular fissures with a locally high porosity forming low-tortuosity migration paths, while the total porosities of these samples were still relatively low. The other REPRO samples were VGN and included high quantities of biotite which has a tight, foliated structure with nanometer-scale apertures between laminas and a relatively wide variation in porosity [140, 156]. Such structural and mineralogical differences may also explain the overall large variation of the data.

Permeability and porosity correlate similarly (i.e., weakly) as diffusion and porosity (see Fig 5.11). In general, permeability of the sample increases when its porosity is increased. No fit was attempted, as $\log(\epsilon)$ vs. $\log(k)$ had an R-value of 0.44, indicating a very weak power-law correlation. A difference
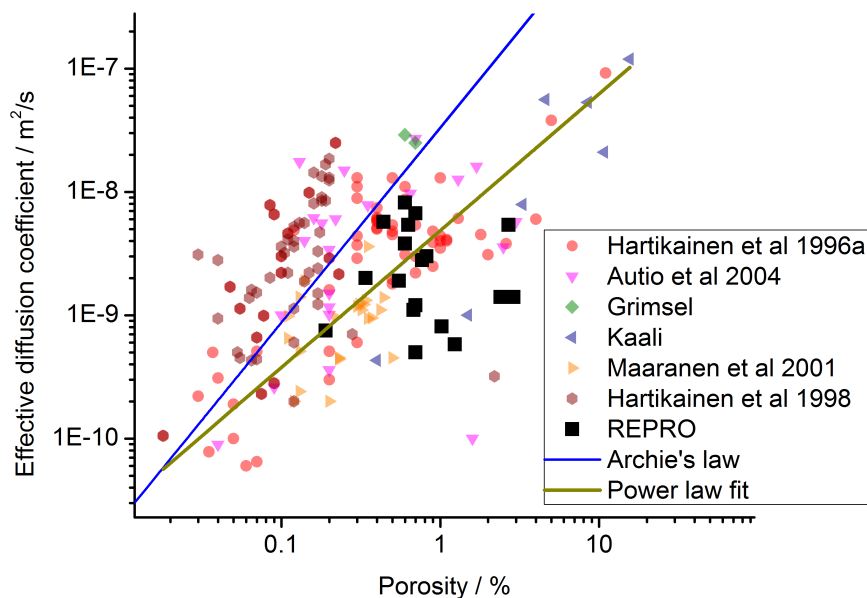
Figure 5.10: Effective diffusion coefficients plotted as a function of porosity reveals a weak correlation between these quantities.

between the samples from drill core ONK-PP318 and the other REPRO samples existed also here. Samples from ONK-PP318 had a systematically lower porosity and higher permeability than the other REPRO samples. Here again, this and the high overall variation of the data can be explained by structural and mineralogical differences between the samples.

The effective diffusion coefficients and permeabilities are, however, more correlated. As expected, permeability increases when the effective diffusion coefficient is increased. Since both of these quantities are strongly related to the pore structure of the material and the tortuosity and constrictivity of the pore network, and since they represent their transport properties, it can be expected that some correlation exists. It needs to be noted that to use this correlation in water phase, it needs to be converted from gas phase using a ratio of diffusion coefficients in pure carriers. A power-law relation $k = 3.6 \cdot 10^{-5} \cdot D_e^{1.67}$ seems to describe the data points quite well (see fig. 5.12). For a linear plot the R-value was 0.48 and for $\log(D_e)$ vs. $\log(k)$ it was 0.87. For the REPRO samples $k = 12200 \cdot D_e^{2.52}$ was used to describe the data points with $R = 0.77$ for a linear plot and $R = 0.76$ for $\log(D_e)$ vs. $\log(k)$. Note that linear fittings are not shown in fig. 5.12. These results suggest that linear correlation of these quantities is not very strong, except for the REPRO samples, but they seem to be related by a power law. Here the REPRO samples fall into two groups. The samples from drill core ONK-PP318, which are mostly PGR, have high effective diffusion coefficients and high permeabilities, and the other REPRO samples, which are mostly VGN, have lower diffusion coefficients and lower permeabilities.

Only a weak correlation was found between porosity and the other two measured properties. This was expected, since bulk porosity completely ignores the structure of the pore space. Quantities such as tortuosity and constrictivity are needed to connect porosity with effective diffusion coefficient and

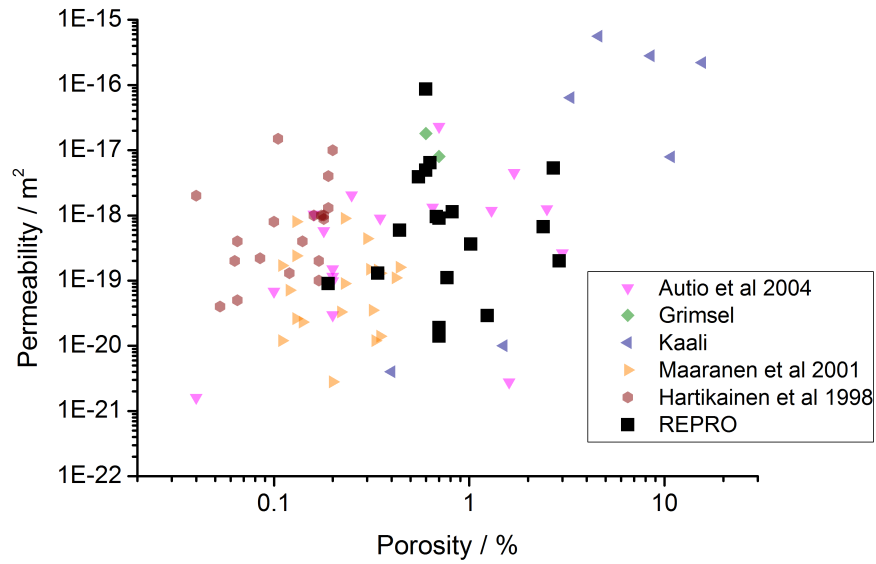**Figure 5.11**: Permeability as a function of porosity displays a very weak correlation between these quantities.
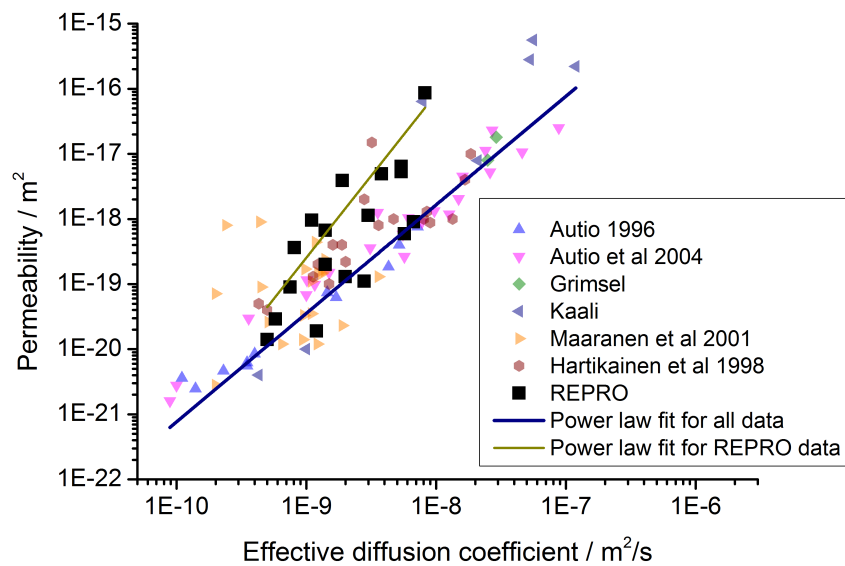

Figure 5.12: Permeability as a function of effective diffusion coefficient displays quite strong correlation between these quantities.

Table 5.4: Results of advection - matrix diffusion measurements for the VGN sample ONK-PP323 19.25-20.05.

Flow rate / $\frac{\text{cm}^3}{\text{min}}$	ϵ / %	D_e / $10^{-10}\frac{\text{m}^2}{\text{s}}$	D_0 / $10^{-4}\frac{\text{m}^2}{\text{s}}$
40	0.6	4.2 ± 0.9	3.2
45	0.6	4.2 ± 0.9	2.7
50	0.6	4.2 ± 0.9	2.7

permeability, but both these quantities have been very difficult to determine (measure). The effect of rock structure was clearly demonstrated when comparing the results for samples from drill core ONK-PP318 and those for the other REPRO samples: ONK-PP318 samples, which were mostly PGR, had a lower porosity and higher effective diffusion coefficient and permeability than the other REPRO samples, which were mostly VGN. This is counter-intuitive, but is explained by structural and mineralogical differences of these samples. Diffusion and permeability are quite similarly affected by tortuosity and constrictivity, at least in gas phase, and were found to be closely related. A power-law relation between these two quantities seems to well describe the data. It can thus be used to estimate one of them if the other one is known. However, the precise values of these quantities must always be determined by direct measurement.

5.5 Advection - matrix diffusion results

The breakthrough curve of the VGN-sample (ONK-PP323 19.25-20.05) measurement was first fitted with the homogeneous model of Eq. (5.23) by fixing ϵ=0.6 % from porosity measurements for VGN in the same drill core and using D_0 and D_p as fitting parameters (see fig. 5.13). The model followed the experimental curve very well. The early part of the breakthrough curve was dominated by advective transport, and the retarding effect of matrix diffusion was seen as strong tailing of the late part of the curve. The results of VGN measurements with various flow rates, shown in Table 5.5, are in accordance with those of the previous gas phase measurements for the same drill core, shown in Table 5.3. The diffusion coefficients were changed to effective diffusion coefficients $D_e = D_p \cdot \epsilon$. The results for D_0 are slightly larger than the literature value for diffusion of helium in nitrogen, 6.5 $\cdot 10^{-5}\frac{\text{m}^2}{\text{s}}$ [155]. This difference of less than an order of magnitude can be explained by dispersion and a possible additional effect within the mass spectrometer.

It needs to be noted that a similar result was also obtained by fixing D_0 at the literature value and adding a second, more porous component with a higher diffusion coefficient in the matrix. Thus the method cannot reliably measure D_0, as its effect is indistinguishable from that of a high porosity component in the sample.

The breakthrough curve for the PGR-sample (ONK-PP318 11.98-12.78) measurement had, however, a very different shape and could not be modeled with the homogeneous model, as is evident from fig. 5.14. If the model was fitted to the tail of the curve, it did not describe the measurement at the end of the main pulse (left panel) and if it was fitted to the main pulse of the curve, it did not describe the measurement at the tail (right panel).

This effect was concluded to arise from differences in rock structure, as the porosities of VGN from ONK-PP323 and PGR from ONK-PP318 are close to each other and the difference between their diffusion coefficients is about one order of magnitude. To study this, separate samples of both rock
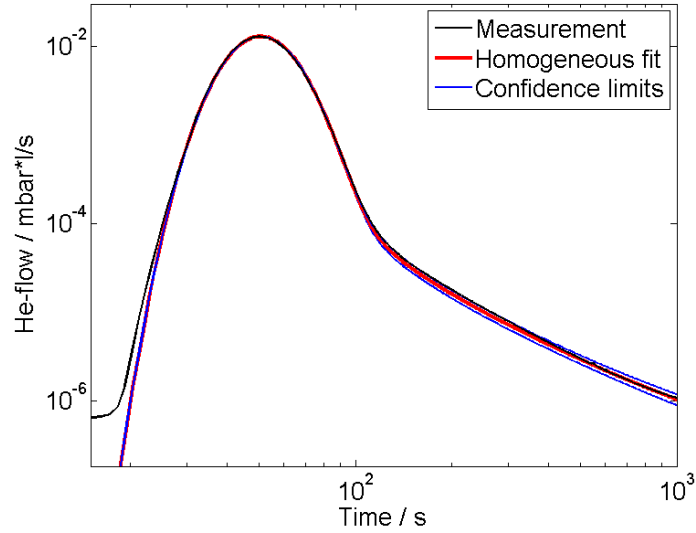
Figure 5.13: Result of an advection - matrix diffusion measurement on the VGN sample ONK-PP323 19.25-20.05 together with a homogeneous fit by Eq. (5.23) with confidence limits. In this measurement, $\epsilon = 0.6$ % and $D_e = (4.2 \pm 0.9) \cdot 10^{-10} \frac{\text{m}^2}{\text{s}}$. The flow rate used was 45 $\frac{\text{cm}^3}{\text{min}}$.
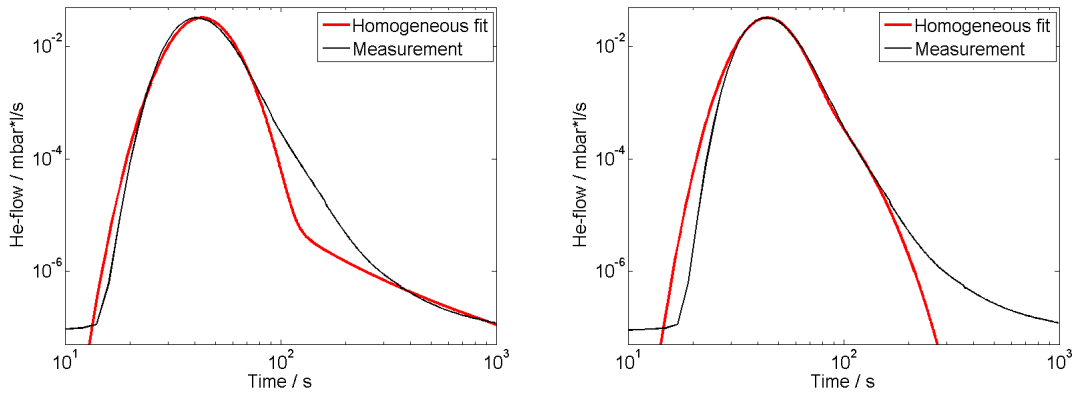
Figure 5.14: The breakthrough curve of the PGR sample ONK-PP318 11.98-12.78 with an attempt to fit it by a homogeneous model: fitting of the tail (left panel) and fitting of the main pulse (right panel) of the curve. The "shoulder" effect created by a finite matrix depth is evident in the breakthrough curve (right panel).
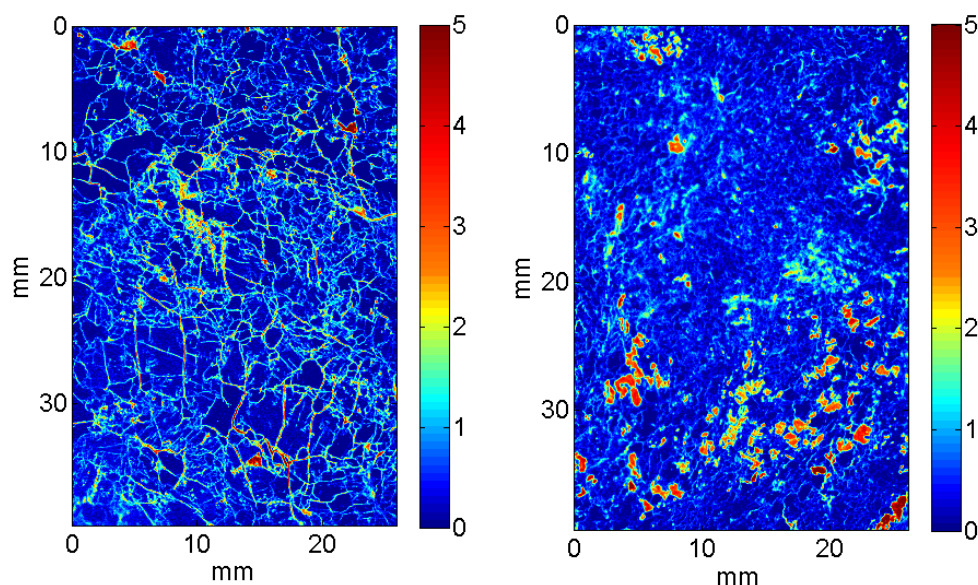
Figure 5.15: 2-d porosity maps obtained with the ^{14}C-PMMA-autoradiography technique for PGR (left) and VGN (right). Porosities from 0% to 5% are shown, with porosities over 5% (up to 12% for PGR and 7% for VGN) shown in red. Difference in the distributions of porosity is clearly visible. PGR has a low background porosity with thin, connected, high-porosity features, whereas VGN has a higher background porosity with larger high-porosity areas that are grain like and do not form a connected network.

types, from the same drill cores as the advection - matrix diffusion samples, were studied using the ^{14}C-PMMA-autoradiography technique (see Section 3.1). 2-d porosity maps of both rock types are shown in fig. 5.15. It is evident that in VGN the porosity is divided into high-porosity (3–7 %) areas that are a few mm in diameter, and into a moderately high and even background porosity (0.5–1.0 %), which means the grain boundary pores are filled with PMMA. The high porosity areas in VGN are granular, and should thus affect matrix diffusion more than through diffusion, but this was not observed as the D_e obtained from the advection - matrix diffusion experiments was actually from the lower end of VGN results. They are congruent with altered mineral grains, such as cordierite and chlorite and of the same length scale as the high porosity component used in the two-component fit above. In PGR the background porosity is smaller (0–0.3 %), but there are thin (tens of μm) intergranular areas, where porosity is very high (up to 12 %). The high-porosity areas in PGR are grain boundaries that form a continuous migration network across the sample. In PGR there are also mineral grains (quartz) that are completely non-porous.

This difference in the porosity distributions is also evident in the porosity histograms shown in fig. 5.16. VGN has larger areas of moderate porosity, whereas PGR is more divided into areas of very-low and very-high porosity.

Based on the porosity structure information a multi-component model was used for the PGR sample of the same form as Eq. (5.20). A crude division into three parts was done, loosely based on the ^{14}C-PMMA data of fig. 5.15. One quarter of the sample was considered to be less porous with a lower diffusion coefficient than the rest of the sample, as PGR has some very low-porosity quartz grains. This quarter is now referred to as component 1. One quarter of the sample was considered to be more porous with a higher diffusion coefficient than the rest of the sample to account for the high-
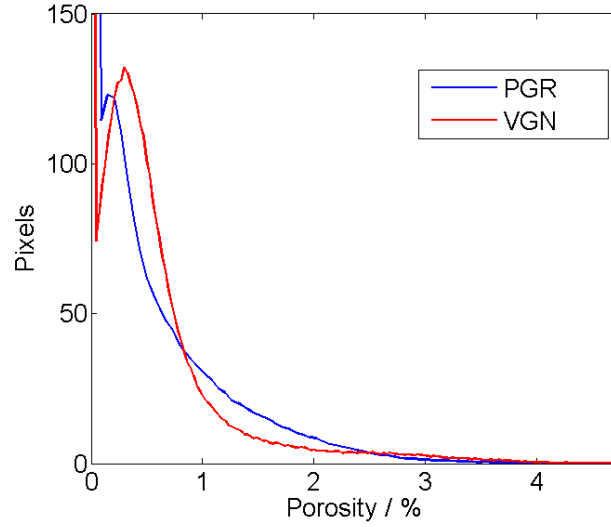
Figure 5.16: Porosity histograms obtained with the ^{14}C-PMMA-autoradiography technique for PGR (blue line) and VGN (red line) samples. Total amount of pixels in the analysis was 570 000 / sample. VGN has more zones of moderate porosity, whereas PGR has more areas of very low or very high porosity.

Table 5.5: Results of advection - matrix diffusion measurements for the PGR sample ONK-PP318 11.98-12.78.

Flow rate / $\frac{\text{cm}^3}{\text{min}}$	ϵ_1 / %	D_{e1} / $10^{-10}\frac{\text{m}^2}{\text{s}}$	ϵ_2 / %	D_{e2} / $10^{-10}\frac{\text{m}^2}{\text{s}}$	ϵ_3 / %	D_{e3} / $10^{-10}\frac{\text{m}^2}{\text{s}}$	D_f / $10^{-4}\frac{\text{m}^2}{\text{s}}$
40	0.08	0.16 ± 0.04	0.45	32 ± 7	1.6	800 ± 400	1.9
45	0.08	0.16 ± 0.04	0.45	29 ± 6	1.6	800 ± 400	2.4
50	0.08	0.24 ± 0.05	0.45	32 ± 7	1.6	800 ± 400	3.0

porosity grain boundaries of the sample, and will now be referred to as component 3. The remaining half was considered to be of average porosity and diffusion coefficient, and will now be referred to as component 2. Components 2 and 3 also had a layer of component 1 placed underneath them to model the tight inner matrix. A schematic form of the model is shown in fig. 5.17. The components are divided evenly around the sample to ensure a well-mixed flow, but are presented undivided here for clarity. The porosities of the components were taken by dividing the porosity distribution into four quarters and using the average porosity of the first quarter for component 1, the average porosity of the last quarter for component 3 and the average porosity of the two middle quarters for component 2. These porosities were fixed, and the diffusion coefficients D_p of all three components, along with D_0, were used as the fitting parameters. The breakthrough curve along with a three-component fit with confidence limits are shown in fig. 5.18 and the results for various flow rates in Table 5.5 with the diffusion coefficients again converted to effective diffusion coefficients D_e.

Comparing the three-component result with that of the through diffusion measurements that only gave a single value for ϵ and D_e, is not straightforward, as none of the values given by the three-component model directly correspond with a single value given by a single component model. If
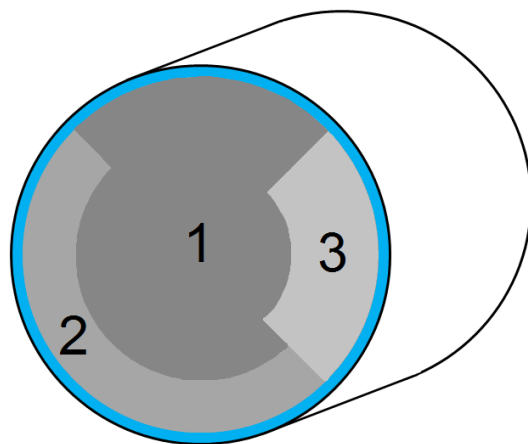
Figure 5.17: A schematic presentation of the geometry used for modelling the PGR sample (ONK-PP318 11.98-12.78) with three components. Components are numbered from that of the lowest porosity and diffusion coefficient to that of the highest ones. The components are spread evenly around the sample to ensure a well-mixed flow, but are presented undivided here for clarity. The surface areas of the components are 25 % for components 1 and 3 and 50 % for component 2. The border between the components is at $0.7R$ between components 1 and 2 and at $0.5R$ between components 1 and 3, where R is the radius of the sample.
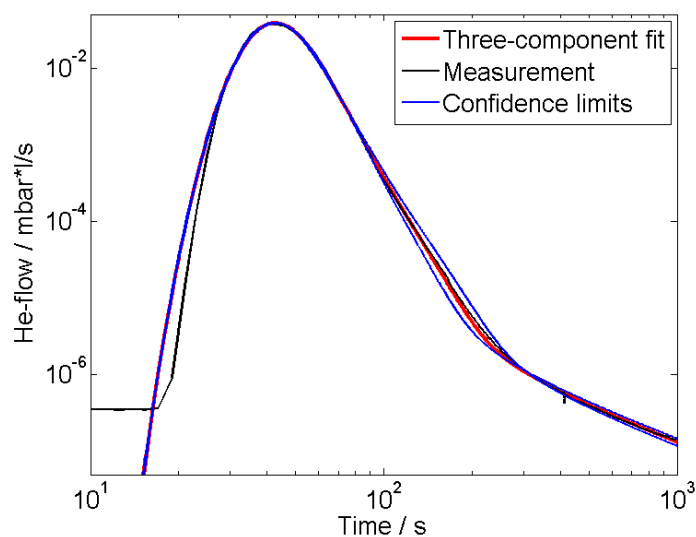
Figure 5.18: Result of an advection - matrix diffusion measurement of the PGR sample together with a three-component fit of the form Eq. (5.20) along with confidence limits, where all three components were varied in the same direction. In this measurement ϵ_1=0.08%, ϵ_2=0.45%, ϵ_3=1.6%, $D_{e1} = (0.24 \pm 0.05) \cdot 10^{-10} \frac{\text{m}^2}{\text{s}}$, and $D_{e2} = (32 \pm 7) \cdot 10^{-10} \frac{\text{m}^2}{\text{s}}$ and $D_{e3} = (800 \pm 400) \cdot 10^{-10} \frac{\text{m}^2}{\text{s}}$. The flow rate used was 50 $\frac{\text{cm}^3}{\text{min}}$.

one considers the through diffusion behaviour to be dominated by component 2, the results are in accordance with each other. The through diffusion results are shown in Table 5.3. For the longitudinal diffusion coefficient in the channel, the result was again close enough to the literature value so it can be explained, although now a clear dependence on the flow rate can be observed.

The used measurement setup and mathematical model have both been developed and used well before this experiment, but both have also taken big steps forward during the project. This is the first time the gas phase measurement is done with a column of this size. The measurement setup has been improved by analysing measurements done with an impermeable dam, which were used to get rid of artifacts caused by a bad flange design that showed as additional tracer retardation. It is now capable of measuring matrix diffusion with good accuracy in a well-controlled system. The repeatability of the measurements with various flow rates is a good indicator of that. The mathematical model has developed into a powerful tool in the interpretation and analysis of this kind of advection - diffusion experiments, as it can now be used for several types of samples with different heterogeneities. The retarding effect of matrix diffusion was detected and quantified in both samples, and therefore it can be concluded that these tools can be used to study matrix diffusion and to approximate the effect it has on the radionuclide transport in the geosphere.

The homogeneous model agreed with the result of measurement for the VGN sample very well. The obtained results for porosity and effective diffusion coefficient were in accordance with those we have measured from the same drill core previously with the gas phase through diffusion measurements. The diffusion coefficients obtained from the advection - matrix diffusion measurements were slightly larger than those of the through diffusion measurements, which was to be expected as VGN contains high-porosity areas that do not form a continuous transport network for through diffusion. The homogeneous model seems to work very well if the local variations in pore structure in the sample are not too drastic. The longitudinal diffusion coefficient in the flow channel was about four times larger than the literature value for diffusion of helium in nitrogen. The difference is not big considering the accuracy of the model, but it does indicate that dispersion in the measurement is perhaps more complicated than Taylor dispersion, which was included in the model. The difference could also be due to some artifacts caused by the ends of the sample and to some kind of delay effect inside the mass spectrometer. It needs to be noted that the model is not capable of accurately measuring longitudinal diffusion in the flow channel, as its effect is indistinguishable from that of a high-porosity layer on top of the rock matrix, which could be attributed to something like a bore-disturbed zone (BDZ) or the high-porosity areas in VGN.

The homogeneous model did not work for the PGR sample even though both samples had a similar total porosity, and the difference in D_e obtained from through diffusion measurements was just one order of magnitude. It was concluded that the reason for this was the high variation in the local porosity and pore structure, as shown by the ^{14}C-PMMA autoradiographs (fig. 5.15). This assumption was confirmed by using the three-component model to account for the very low porosity and very high porosity zones present in this sample. The result for one of the components in the three-component fit had a similar porosity and effective diffusion coefficient as previously measured for the same sample type from that area. Information of the retarding effects happening in different time scales, which is relevant to real scenarios, was obtained, and cannot be obtained with more traditional through diffusion measurements that only give information on the transmissive behaviour of the rock. This shows that the heterogeneous structure of rock can have a much more significant effect on the breakthrough curve than has previously been anticipated. The ^{14}C-PMMA-autoradiography technique was instrumental in this discovery. Without these auto-radiographs it may have been impossible to interpret the breakthrough curve of the PGR sample. Based on this experiment, it can be concluded that knowledge of the mineralogy and structure of the investigated rock is vital in understanding the results of this type of an advection - matrix diffusion experiment.

6   Conclusions and outlook

The objectives of this Thesis were to improve the understanding of radionuclide transport in the geosphere by developing new methods for analysing geological structures, improving the existing methods, characterising water conducting fractures and producing usable data for the safety assessment of the used nuclear fuel repository. To this end, fracture samples from Olkiluoto were characterised using X-ray tomography, the ^{14}C-PMMA autoradiography technique and microscopy with polarised light to connect certain properties to certain fracture types. The porosity, diffusion coefficient and permeability were also measured for rock samples from Olkiluoto with Ar-pycnometry, through diffusion measurements, permeability measurements and advection - matrix diffusion measurements in gas phase. A method to convert local porosities obtained by the ^{14}C-PMMA autoradiography technique into fracture apertures was also developed.

3-d distributions of minerals and porosities were determined for samples with water conducting fractures. The minerals were identified using microscopy with polarised light, the porosity profiles adjacent to the fractures in 2-d were determined using the ^{14}C-PMMA autoradiography technique and the mineral distributions were determined using X-ray tomography. X-ray tomography is most useful when it is combined with other methods, and doing this requires very careful planning and sample preparation. This was successfully done for one veined gneiss sample with a clay fracture by combining the tomographic image with polarised light microscopy and thus identifying the mineral components in the tomographic image. It was found that the properties of rock around water conducting fractures depend on many uncorrelated factors and no clear pattern was found for the measured rock properties even for rock samples with a given type of fracture. Some ranges for various parameters, such as the depth of the alteration zone, were nevertheless acquired for various fracture types.

The methods used for the gas phase measurements of porosity, diffusion coefficient and permeability were found to be fast, reliable and non-destructive. The results obtained for the transport properties of the REPRO samples were of the same magnitude as those typical to the Olkiluoto area. They will be later compared with ones resulting from on-going in situ experiments [80] to gain knowledge of the possible influence of lithostatic pressure and its release and sample preparation. The obtained results were also compared with those of previous experiments to look for possible correlations between porosity, effective diffusion coefficient and permeability. Porosity was found to be only weakly correlated with the other two properties as expected, since a bulk porosity measurement completely ignores the structure of the pore space. The diffusion coefficients and permeabilities were found to be related by a power-law function, which was expected, as the pore space structure affects diffusion and permeability quite similarly. The relation is however not accurate enough to give more than an estimate and the exact values still need to be determined by direct measurement.

The measurement setup and mathematical model used for the advection - matrix diffusion measurements in gas phase were developed further during the measurements. The measurement setup was improved by analysing measurements done with an impermeable dam. Finally it was capable of measuring matrix diffusion with good accuracy in a well controlled system, as shown by the good repeatability of the measurements with various flow rates. The mathematical model was developed into a powerful tool in the interpretation and analysis of this kind of measurements and can now be used for several types of samples with different heterogeneities. The retarding effect of matrix diffu-

sion was detected and quantified from both measured samples. The diffusion coefficient obtained for the veined gneiss sample in the measurements was slightly smaller than that obtained by through diffusion measurements. The homogeneous model could not explain the results of the pegmatitic granite measuremet as the high porosity areas in pegmatitic granite are at the grain boundaries and thus very thin and porous. There are also non-porous grains (of mostly quartz) in the rock. These measurements required a more complex model that ultimately gave information on the retarding effects happening in different time-scales, which is unobtainable by through diffusion measurements. This also showed that the heterogeneous structure of rock can have a much more significant effect on the breakthrough curve than previously anticipated, meaning that the knowledge of the mineralogy and structure of the investigated rock is vital in understanding the results of this type of an experiment. The tools used here were concluded to be effective in studying matrix diffusion and the effect it has on radionuclide transport in the geosphere.

Finally a method for transforming local porosities obtained by the ^{14}C-PMMA autoradiography technique was developed. Simple Monte Carlo simulations were first performed to see the theoretical activity profiles produced by linear fractures perpendicular to the autoradiographic film. A connection between these profiles and the corresponding fracture apertures was then found and validated through measurements of artificial glass plate samples with perpendicular fractures. The fractures were divided into thick and thin by aperture and both types were converted in a different way. Fractures with thin apertures were converted by determining the activity at the peak of the profile and converting it to an aperture, whereas the fractures with thick apertures were converted by thresholding the activity profile at a determined value. Intermediate fractures needed to be dealt with by a combination of the two ways. The experiments successfully validated the method and produced improved parameters. While the method is not yet ready to be used on real geological samples, it was concluded to be promising and it can most likely be developed into a fully automatic method to obtain fracture aperture distributions from a local porosity map obtained by the ^{14}C-PMMA autoradiography technique.

In the future the results from articles in Appendices I, III and V will be used to aid and interpret in situ measurements and compared to the results obtained from them to learn more on the water phase processes taking place. The modelling tool developed for the advection - matrix diffusion measurement will be used to interpret in situ measurements. Use of X-ray tomography on the field of transport in geological samples will also be developed. A quite promising experiment where cesium transport is investigated in rock samples with X-ray tomography has already been conducted and is currently under analysis. Of the studies depicted in this work, the method developed in the article in Appendix II and verified in the article in Appendix IV has the most future work ahead. The method could be improved by using digital autoradiography or filmless autoradiography, made possible by the new Beaver devices developed by ai4r. The method also needs work on non-perpendicular fractures, boundary fractures (different density on either side of the fracture) and ultimately application to real geological samples, of course. This will require some advanced image analysis in addition to developing the method itself. One potential use will be the investigation of excavation disturbances, where grain boundaries have opened and new fractures have developed. The fractures in such cases should be ideal for this tool. I hope to be a part of this development.

References

[1] C. McCombie. Nuclear waste management worldwide. *Physics Today*, 50(6):56–62, 1997.

[2] N.T. Rempe. Permanent underground repositories for radioactive waste. *Progress in Nuclear Energy*, 49(5):365–374, 2007.

[3] J.-S. Kim, S.-K. Kwon, M. Sanchez, and G.-C. Cho. Geological storage of high level nucelar waste. *KSCE Journal of Civil Engineering*, 15(4):721–737, 2011.

[4] T. Labalette. The Cigeo project. *Realites Industrielles*, 3:92–97, 2012.

[5] G. Bäckblom. Progress towards a deep repository for spent nuclear fuel in Sweden. *Journal of Nuclear Science and Technology*, 35(9):623–630, 1998.

[6] T. McEven and T. Äikäs. The site selection process for a spent fuel repository in Finland - summary report. Posiva Report 2000-15, Posiva Oy, 2000.

[7] A.G. Milnes, M.B. Stephens, C.-H. Wahlgren, and L. Wikström. Geoscience and high-level nuclear waste disposal: the Nordic scene. *Episodes*, 31:168–175, 2008.

[8] Posiva Oy. Final disposal of spent nuclear fuel in the Finnish bedrock, technical research and development in the period 1993-1996. Posiva Report 1996-14, Posiva Oy, 1996. In Finnish.

[9] Posiva Oy. Safety case for the disposal of spent nuclear fuel at Olkiluoto - Models and data for the repository system 2012. Posiva Report 2013-01, Posiva Oy, 2013.

[10] L. Forsström. Future glaciation in Fennoscandia. Posiva Report 99-30, Posiva Oy, 1999.

[11] M.I. Sheppard, B.D. Amiro, P.A. Davis, and R. Zach. Continental glaciation and nuclear fuel waste disposal: Canada's approach and assessment of the impact on nuclide transport through the biosphere. *Ecological modelling*, 78(3):249–265, 1995.

[12] K.-L. Hutri and J. Antikainen. Modelling of the bedrock response to glacial loading at the Olkiluoto site. *Engineering Geology*, 61(1-2):39–39, 2002.

[13] T. Vieno and A. Ikonen. Plan for safety case of spent fuel repository at Olkiluoto. Posiva Report 2005-01, Posiva Oy, 2005.

[14] C. David. Geometry of flow paths for fluid transport in rocks. *Journal of Geophysical Research*, 98(B7):12267–12278, 1993.

[15] Y. Bernabé. The transport properties of networks of cracks and pores. *Journal of Geophysical Research*, 100(B3):4231–4241, 1995.

[16] P. Sardini, L. Caner, P. Mossler, A. Mazurier, K.-H. Hellmuth, R.C. Graham, A.M. Rossi, and M. Siitari-Kauppi. Calibration of digital autoradiograph technique for quantifying rock porosity using ^{14}C-PMMA method. *Journal of Radioanalytical and Nuclear Chemistry*, 303:11–23, 2015.

[17] A.M. Rossi and R.C. Graham. Weathering and porosity formation in subsoil granitic clasts, Bishop Creek moraines, California. *Soil Science Society of America Journal*, 74:172–185, 2010.

[18] T.F. Wong, J.T. Fredrich, and G.D. Gwanmesia. Crack aperture statistics and pore space fractal geometry of westerly granite and rutland quartzite: Implications for an elastic contact model of rock compressibility. *Journal of Geophysical Research*, 94(B8):10267–10278, 1989.

[19] M. Montoto, A. Martínez-Nistal, A. Rodríguez-Rey, N. Fernández-Merayo, and P. Soriano. Microfractography of granitic rocks under confocal scanning laser microscopy. *Journal of Microscopy*, 177(2):138–149, 1995.

[20] P. Sardini, S. Sammartino, A. Meunier, and E. Tévissen. Evolution of fluid pathways of Charroux-Civray tonalite (part II): Numerical study of microcrack networks. *Physics and Chemistry of the Earth, Part A: Solid Earth and Geodesy*, 24(7):621–625, 1999.

[21] V. Cnudde and M.N. Boone. High-resolution X-ray computed tomography in geosciences: A review of the current technology and applications. *Earth-Science Reviews*, 123:1–17, 2013.

[22] F. Fusseis, X. Xiao, C. Schrank, and F. De Carlo. A brief guide to synchrotron radiation-based microtomography in (structural) geology and rock mechanics. *Journal of Structural Geology*, 65:1–16, 2014.

[23] R.A. Ketcham, D.T. Slottke, and J.M. Sharp, Jr. Three-dimensional measurement of fractures in heterogeneous materials using high-resolution X-ray computed tomography. *Geosphere*, 6:499–514, 2010.

[24] B. Jamtveit, M. Krotkiewski, M. Kobchenko, F. Renard, and L. Angheluta. Pore-space distribution and transport properties of an andesitic intrusion. *Earth and Planetary Science Letters*, 400:123–129, 2014.

[25] K.-H. Hellmuth, M. Siitari-Kauppi, and A. Lindberg. Study of porosity and migration pathways in crystalline rock by impregnation with 14C-polymethylmethacrylate. *Journal of Contaminant Hydrology*, 13(1-4):403–418, 1993.

[26] K.-H. Hellmuth, S. Lukkarinen, and M. Siitari-Kauppi. Rock matrix studies with carbon-14-polymethylmethacrylate (PMMA): Method development and applications. *Isotopes in Environmental and Health Studies*, 30(1):47–60, 1994.

[27] K.-H. Hellmuth, M. Siitari-Kauppi, P. Klobes, K. Meyer, and J. Goebbels. Imaging and analyzing rock porosity by autoradiography and Hg-porosimetry/X-ray computertomography - Applications. *Physics and Chemistry of the Earth, Part A: Solid Earth and Geodesy*, 24(7):569–573, 1999.

[28] M. Siitari-Kauppi, A. Lindberg, J. Ikonen, and I. Kauppi. Investigation of porosity and pore structure by pmma method of samples taken from deep drill holes OL-KR38 and OL-KR39. Posiva Working Report 2009-03, Posiva Oy, 2009.

[29] M. Siitari-Kauppi. *Development of 14C-polymethylmethacrylate method for the characterisation of low porosity media: Application to rocks in geological barriers of nuclear waste storage.* PhD thesis, University of Helsinki, 2002. Report series in Radiochemistry 17.

[30] A. Blumstein. Polymerization of adsorbed monolayers. I. preparation of clay-polymer complex. *Journal of Polymer Science: Part A*, 3:2653–2664, 1965.

[31] I. Aaltonen, M. Lahti, J. Engström, J. Mattila, M. Paananen, M. Paulamäki, S. Gehör, A. Kärki, T. Ahokas, T. Torvela, and K. Front. Geological model of the Olkiluoto site - Version 2.0. Posiva Working Report 2010-70, Posiva Oy, 2010.

[32] A. Poteri. *Simplifying solute transport modelling of the geological multi-barrier disposal system.* PhD thesis, Aalto University, 2013. VTT Science 42.

[33] E. Maire and P.J. Withers. Quantitative X-ray tomography. *International Materials Reviews*, 59:1–43, 2014.

[34] A. Vallebona. A method of taking roentgenograms which makes it possible to eliminate shadows. *Fortschritte auf dem Gebiete der Röntgenstrahlen*, 48:599–605, 1933.

[35] A.G. Filler. The history, development, and impact of computed imaging in neurological diagnosis and neurosurgery: CT, MRI and DTI. *Nature Precedings*, 2009. doi:10.1038/npre.2009.3267.5.

[36] G.N. Hounsfield. Method and aparatus for measuring X- and γ-radiation absorption of transmission at plural angles and analyzing the data. *US Patent*, 3, 778, 614, 1970.

[37] G.N. Hounsfield. Computerized transverse axial scanning (tomography): Part 1. Description of the system. *British Journal of Radiology*, 46:1016–1022, 1973.

[38] R.A. Ketcham and W.D. Carlson. Acquisition, optimization and interpretation of X-ray computed tomographic imagery: Applications to the geosciences. *Computers & Geosciences*, 27(4):381–400, 2001.

[39] W.D. Carlson, T. Rowe, R.A. Ketcham, and M.W. Colbert. Applications of high-resolution X-ray computed tomography in petrology, meteoritics and palaentology. *Geological Society. London. Special Publications*, 215:7–22, 2003.

[40] V. Cnudde, B. Masschaele, M. Dierick, J. Vlassenbroeck, L. Van Hoorebeke, and P. Jacobs. Recent progress in X-ray CT as a geosciences tool. *Applied Geochemistry*, 21(5):826–832, 2006.

[41] B. Haubitz, M. Prokop, W. Dohring, J.H. Ostrom, and P. Wellnhofer. Computed tomography of Archaeoptreyx. *Paleobiology*, 14(2):206–213, 1988.

[42] R.S. Tykoski, T.B. Rowe, R.A. Ketcham, and M.W. Colbert. Calsoyasuchus valliceps, a new crocodyliform from the Early Jurassic Kayenta Formation of Arizona. *Journal of Vertebrate Paleontology*, 22(3):593–611, 2002.

[43] M. Van Geet, D. Lagrou, and R. Swennen. Porosity measurements of sedimentary rocks by means of microfocus X-ray computed tomography. *Geological Society. London. Special Publications*, 215:51–60, 2003.

[44] V. Cnudde, M. Boone, J. Dewanckele, M. Dierick, L. Van Hoorebeke, and P. Jacobs. 3D characterization of sandstone by means of X-ray computed tomography. *Geosphere*, 7:54–61, 2011.

[45] M. Van Geet, R. Swennen, and M. Wevers. Towards 3-D petrography: Application of microfocus computer tomography in geological science. *Computers & Geoscience*, 27(9):1091–1099, 2001.

[46] S. Crestana, S. Mascarenhas, and R.S. Pozzi-Mucelli. Static and dynamic three-dimensional studies of water in soil using computed tomographic scanning. *Soil Sciences*, 140(5):326–332, 1985.

[47] I.A. Taina, R.J. Heck, and T.R. Elliot. Application of X-ray computed tomography to soil science: A literature review. *Canadian Journal of Soil Science*, 88:1–19, 2008.

[48] S.Y. Wang, Y.B. Huang, V. Pereira, and C.C. Gryte. Application of computed tomography to oil recovery from porous media. *Applied Optics*, 24(23):4021–4027, 1985.

[49] S.L. Wellington and H.J. Vinegar. X-ray computerized tomography. *Journal of Petroleum Technology*, 39(8):885–898, 1987.

[50] S. Akin and A.R. Kovseck. Computed tomography in petroleum engineering research. *Geological Society. London. Special Publications*, 215:23–38, 2003.

[51] H.J. Vinegar and S.L. Wellington. Tomographic imaging of three-phase flow experiments. *Review of Scientific Instruments*, 58:96–107, 1987.

[52] A.C. Kak and M. Slaney. *Principles of computerized tomographic imaging.* IEEE Press, 1988.

[53] J.-F. Thovert, F. Yousefian, P. Spanne, C.G. Jacquin, and P.M. Adler. Grain reconstruction of porous media: Application to a low-porosity Fontainebleau sandstone. *Physical review E, Statistical physics, plasmas, fluids, and related interdisciplinary topics*, 63(6):061307, 2001.

[54] L. Farber, G. Tardos, and J.N. Michaels. Use of X-ray tomography to study the porosity and morphology of granules. *Powder Technology*, 132:57–63, 2003.

[55] C.J. Gommes, A.-J. Bons, S. Blacher, J.H. Dunsmuir, and A.H. Tsou. Practical methods for measuring the tortuosity of porous materials from binary of gray-tone tomographic reconstructions. *AlChE Journal*, 55(8):2000–2012, 2009.

[56] V. Cnudde, J. Dewanckele, M. Boone, T. de Kock, M. Boone, L. Brabant, M. Dusar, M. de Ceukelaire, H. de Clercq, R. Hayen, and P. Jacobs. High-resolution X-ray CT for 3D petrography of ferruginous sandstone for an investigation of building stone decay. *Microscopy research and technique*, 74(11):1006–1017, 2011.

[57] P. Gouze and L. Luquot. X-ray microtomography characterization of porosity, permeability and reactive surface changes during dissolution. *Journal of Contaminant Hydrology*, 120-121:45–55, 2011.

[58] M. Voutilainen, M. Siitari-Kauppi, P. Sardini, A. Lindberg, and J. Timonen. Pore-space characterization of an altered tonalite by X-ray computed microtomography and the ^{14}C-labeled-polymethylmethacrylate method. *Journal of Geophysical Research*, 117, 2012. B01201.

[59] M. Voutilainen. *Characterization of structure and diffusion in geological materials.* PhD thesis, University of Jyväskylä, 2012. Research Report No. 12/2012.

[60] K. Väätäinen, J. Timonen, and A. Hautojärvi. Development of a gas method for migration studies in fractured and porous media. In *MRS proceedings 294*, pages 851–856, Pittsburgh, 1993. MRS.

[61] K. Hartikainen, K. Väätäinen, , A. Hautojärvi, and J. Timonen. Further development and studies of gas methods in matrix diffusion. In *MRS proceedings 333*, pages 821–826, Pittsburgh, 1994. MRS.

[62] K. Hartikainen, A. Hautojärvi, H. Pietarila, and J. Timonen. Diffusion measurements on crystalline rock matrix. In T. Murakami and R. Ewing, editors, *MRS proceedings 353: Scientific Basis for Nuclear Waste Management XVIII*, pages 435–440, Pittsburgh, 1995. MRS.

[63] M. Laajalahti. *Through-Diffusion and Permeability Measurements of Rock and Havar Samples Using Helium Gas Methods.* PhD thesis, University of Jyväskylä, 2001. Thesis for the Degree of Licentiate of Philosophy.

[64] J. Hartikainen, K. Hartikainen, A. Hautojärvi, K. Kuoppamäki, and J. Timonen. Helium gas methods for rock characteristics and matrix diffusion. Posiva Report 96-22, Posiva Oy, 1996.

[65] I. Neretnieks. Diffusion in the rock matrix: An important factor in radionuclide retardation? *Journal of Geophysical Research*, 85(B8):4379–4397, 1980.

[66] C. Morrow and J. Byerlee. Permeability of rock samples from Cajon Pass, California. *Geophysical Research Letters*, 15:1033–1036, 1988.

[67] M. Siitari-Kauppi, K.-H. Hellmuth, A. Lindberg, and T. Huitti. Diffusion in homogeneous and heterogeneous rock matrices. A comparison of different experimental approaches. *Radiochimica Acta*, 66:409–414, 1994.

[68] H. Johansson, M. Siitari-Kauppi, M. Skålberg, and E. L. Tullborg. Diffusion pathways in crystalline rock-examples from äspö-diorite and fine-grained granite. *Journal of Contaminant Hydrology*, 35:41–53, 1998.

[69] M. Löfgren and I. Neretnieks. Through-electromigration: A new method of investigating pore connectivity and obtaining formation factors. *Journal of Contaminant Hydrology*, 87:237–252, 2006.

[70] E. I. Parkhomenko. *Electrical Properties of Rocks*. Plenum Press, New York, 1967.

[71] V. Havlová, P. Večerník, J. Najser, K. Sosna, and K. Breiter. Radionuclide diffusion into undistubed and altered crystalline rocks. *Mineralogical Magazine*, 76(8):3191–3201, 2012.

[72] J. Byegård, E. Selnert, and E. L. Tullborg. Bedrock transport properties. data evaluation and retardation model. site descriptive modelling. SDM-site Forsmark. SKB Rapport R-08-98, SKB AB, 2008.

[73] E. Selnert, J. Byegård, H. Widestrand, S. Carlsten, C. Döse, and E. L. Tullborg. Bedrock transport properties. data evaluation and retardation model. site descriptive modelling. SDM-site Laxemar. SKB Rapport R-08-100, SKB AB, 2009.

[74] K. Skagius and I. Neretnieks. Porosities and diffusivities of some nonsorbing species in crystalline rocks. *Water Resources Research*, 22(3):389–398, 1986.

[75] S. Peng, Q. Hu, and S. Hamamoto. Diffusivity of rocks: Gas diffusion measurements and correlation to porosity and pore size distribution. *Water Resources Research*, 48(W02507), 2012.

[76] M. Schild, S. Siegesmund, A. Vollbrecht, and M. Mazurek. Characterization of granite matrix porosity and pore-space geometry by in sity and laboratory methods. *Geophysical Journal International*, 146(1):111–125, 2001.

[77] A. Möri, M. Mazurek, M. Adler, M. Schild, S. Siegesmund, A. Vollbrecht, K. Ota, T. Ando, W.R. Alexander, P.A. Smith, P. Haag, and Ch. Bühler. Grimsel Test Site: The Nagra-JNC in situ study of safety relevant radionuclide retardation in fractured crystalline rock IV: The in situ study of matrix porosity in the vicinity of water conducting fracture. Technical Report NTB 00-08, Nagra, 2003.

[78] K. Ota, A. Möri, W.R. Alexander, B. Frieg, and M. Schild. Influence of the mode of matrix porosity determination on matrix diffusion calculations. *Journal of Contaminant Hydrology*, 61(1-4):131–145, 2003.

[79] J.M. Soler, J. Landa, V. Havlova, Y. Tachi, T. Ebina, P. Sardini, M. Siitari-Kauppi, and A.J. Martin. Modeling of an in-situ diffusion experiment in granite at the Grimsel Test Site. In *Symposium NW - Scientific Basis for Nuclear Waste Management XXXVII*, volume 1665 of *MRS Proceedings*, pages 85–91, 2014.

[80] M. Voutilainen, A. Poteri, K. Helariutta, M. Siitari-Kauppi, K. Nilsson, P. Andersson, J. Byegård, M. Skålberg, P. Kekäläinen, J. Timonen, A. Lindberg, P. Pitkänen, K. Kemppainen, J. Liimatainen, A. Hautojärvi, and L. Koskinen. In-situ experiments for investigating the retention properties of rock matrix in ONKALO, Olkiluoto, Finland. In *WM 2014 Conference Proceedings 40*. WM, 2014. 14258.

[81] P. Aalto, I. Aaltonen, H. Ahokas, J. Andersson, M. Hakala, P. Hellä, J. Hudson, E. Johansson, K. Kemppainen, L. Koskinen, M. Laaksoharju, M. Lahti, S. Lindgren, A. Mustonen, K. Pedersen, P. Pitkänen, A. Poteri, M. Snellman, and M. Ylä-Mella. Programme for repository host rock characterisation in the ONKALO (ReRoC). Working Report 2009-31, Posiva Oy, 2009.

[82] V. Toropainen. Core drilling of REPRO drillholes in ONKALO at Olkiluoto 2010-2011. Posiva Working Report 2012-26, Posiva Oy, 2012.

[83] P. Hölttä. *Radionuclide migration in crystalline rock fractures: Laboratory study of matrix diffusion*. PhD thesis, University of Helsinki, 2002. Report Series in Radiochemistry 20.

[84] J. Hadermann and W. Heer. The Grimsel (Switzerland) migration experiment: integrating field experiments, laboratory investigations and modelling. *Journal of Contaminant Hydrology*, 21(1-4):87–100, 1996.

[85] M. H. Bradbury and A. Green. Investigations into the factors influencing long range matrix diffusion rates and pore space accessibility at depth in granite. *Journal of Hydrology*, 89(1-2):123–139, 1986.

[86] A. M. Shapiro. Effective matrix diffusion in kilometer-scale transport in fractured crystalline rock. *Water Resources Research*, 37(3):507–522, 2001.

[87] M. Voutilainen, P. Kekäläinen, A. Hautojärvi, and J. Timonen. Validation of matrix diffusion modeling. *Physics and Chemistry of the Earth*, 35:259–264, 2010.

[88] P. Kekäläinen, M. Voutilainen, A. Poteri, P. Hölttä, A. Hautojärvi, and J. Timonen. Solutions to and validation of matrix-diffusion models. *Transport in Porous Media*, 87(1):125–149, 2011.

[89] P. Kekäläinen. Analytical solutions to matrix diffusion problems. In *International Conference of Computational Methods in Sciences and Engineering 2014, AIP Conference Proceedings 1618*, pages 513–516. ICCMSE, 2014.

[90] J.R. Sibert, J. Hampton, D.A. Fournier, and P.J. Bills. An advection-diffusion-reaction model for the estimation of fish movement parameters from tagging data, with application to skipjack tuna (Katsuwonus pelamis). *Canadian Journal of Fisheries and Aquatic Sciences*, 56(6):925–938, 1999.

[91] J. I. Toivanen, K. Mattila, J. Hyväluoma, P. Kekäläinen, T. Puurtinen, and J. Timonen. Simulation software for flow of fluid with suspended point particles in complex domains: Application to matrix diffusion. In Pekka Manninen and Per Öster, editors, *Applied Parallel and Scientific Computing*, volume 7782 of *Lecture Notes in Computer Science*, pages 434–445. Springer Berlin Heidelberg, 2013.

[92] S. Xu, A. Wörman, and B. Dverstorp. Heterogeneous matrix diffusion in crystalline rock - implications for geosphere retardation of migrating radionuclides. *Journal of Contaminant Hydrology*, 47(2-4):365–378, 2001.

[93] L.C. Hebel, E.L. Christensen, F.A. Donath, W.E. Falconer, L.J. Lidofsky, E.J. Moniz, T.H. Moss, R.L. Pigford, T.H. Pigford, G.I. Rochlin, R.H. Silsbee, M.E. Wrenn, H. Frauenfelder, T.L. Cairns, W.K.H. Panofsky, and M.G. Simmons. Report to the American Physical Society by the study group on nuclear fuel cycles and waste management. *Reviews of Modern Physics*, 50(1):S1–S176, 1978.

[94] National Research Council. *The disposal of radioactive waste on land*. The National Academies Press, Washington, DC, 1957.

[95] Swedish Nuclear Fuel Supply Co/Division KBS (SKBF/KBS. KBS-3 - Final storage of spent nuclear fuel - KBS-3, Summary. SKB report Art716 5, SKB, 1983.

[96] M. Nykyri, H. Nordman, N. Marcos, J. Löfman, A. Poteri, and A. Hautojärvi. Radionuclide release and transport - RNT-2008. Posiva Report 2008-06, Posiva Oy, 2008.

[97] T. Vieno and H. Nordman. Safety assessment of spent fuel in Hästholmen, Kivetty, Olkiluoto and Romuvaara - TILA-99. Posiva Report 99-07, Posiva Oy, 1999.

[98] T. Vieno and H. Nordman. Interim report on safety assessment of spent fuel disposal, TILA-96. Posiva Report 96-17, Posiva Oy, 1996.

[99] Andra. *Dossier 2005. Granite. Safety analysis of a geological repository. Agence natíonale pour la gestion des déchets radioactifs*. Number 287 VA in Andra Report Series. Andra, Châtenau-Malabry, France, 2005.

[100] SKB. Deep repository for spent nuclear fuel. SR 97 - Post-closure safety, Volumes I-II. SKB Technical Report TR-99-06, SKB, 1999.

[101] P. Gierszewski, J. Avis, N. Calder, A. D'Andrea, F. Garisto, C. Kitson, T. Melnyk, K. Wei, and L. Wojciechowski. Third case study - Postclosure safety assessment. Report No. 06819-REP-01200-10109-R00, Ontario Power Generation, 2004.

[102] SKB. Long-term safety for the final repository for spent nuclear fuel at Forsmark. Main report of the SR-Site project, Volumes I-III. SKB Technical Report TR-11-01, SKB, 2011.

[103] Nagra. Kristallin - I, Safety assessment report. Die Nationale Genossenschaft für die Lagerung radioaktiver Abfälle (Nagra). Report NAGRA NTB-93-22, Nagra, 1994.

[104] JNC. H12: Project to establish the scientific and technical basis for HWL disposal in Japan. Report JNC TN1410 2000-001, Japan Nuclear Cycle Development Institute (JNC), 2000.

[105] U.S. Nuclear Regulatory Commission. Radioactive waste: Production, storage, disposal. NUREG/BR-0216 Rev. 2, U.S. Nuclear Regulatory Commission, 2002.

[106] A. Schwenk-Ferrero. German spent nuclear fuel legacy: Characteristics and high-level waste management issues. *Science and Technology of Nuclear Installations*, 2013, 2012. Article ID 293792.

[107] H. Raiko. Disposal canister for spent nuclear fuel - design report. Posiva Report 2005-02, Posiva Oy, 2005.

[108] F. King, L. Ahonen, C. Taxén, U. Vuorinen, and L. Werme. Copper corrosion under expected conditions in a deep geological repository. SKB Technical Report TR-01-23, SKB, 2001.

[109] G.M. Kwong. Status of corrosion studies for copper used fuel containers under low salinity conditions. Report NWMO TR-2011-14, Nuclear Waste Management Organization (NWMO), 2011.

[110] P. Szakálos, G. Hultqvist, and G. Wikmark. Corrosion of copper by water. *Electrochemical and Solid-State letters*, 10(11):C63–C67, 2007.

[111] Swedish National Council for Nuclear Waste. Nuclear waste state-of-the-art report 2010 - challenges for the final repository programme. Official Reports SOU 2010:6, Swedish Government, 2010.

[112] B. Miller and N. Marcos. Process report - FEPs and scenarios for a spent fuel repository at olkiluoto. Posiva Report 2007-12, Posiva Oy, 2007.

[113] SKB. Fuel and canister process report for the safety assessment SR-Site. SKB Technical Report TR-10-46, SKB, 2010.

[114] M.V. Villar, M. Sánchez, and A. Gens. Behaviour of a bentonite barrier in the laboratory: Experimental results up to 8 years and numerical simulation. *Physics and Chemistry of the Earth*, 33:S476–S485, 2008.

[115] R. Pusch. Permeability of highly compacted bentonite. SKB Technical Report 80-16, SKB, 1980.

[116] H. Komine. Theoretical equations for evaluating hydraulic conductivities of bentonite based buffer and backfill. *Journal of Geotechnical and Geoenvironmental Engineering*, 134(4):497–508, 2008.

[117] Swedish Nuclear Fuel Supply Co/Division KBS (SKBF/KBS. KBS-3 - Final storage of spent nuclear fuel - KBS-3, III Barriers. SKB report Art716 3, SKB, 1983.

[118] L. Börgesson, D. Dixon, D. Gunnarsson, J. Hansin, E. Jonsson, and P. Keto. Assessment of backfill design for KBS-3V repository. Posiva Working Report 2009-115, Posiva Oy, 2009.

[119] L. Ahonen, V. Hakkarainen, Kaija. J., A. Kuivamäki, A. Lindberg, M. Paananen, S. Paulamäki, and T. Ruskeeniemi. Geological safety aspects of nuclear waste disposal in Finland. In K. Nenonen and P.A. Nurmi, editors, *125th Anniversary volume*, Geoscience for Society, pages 145–152. Geological Survey of Finland, 2011.

[120] P. Vidstrand, S. Follin, J.-O. Selroos, J.-O. Näslund, and I. Rhén. Modeling of groundwater flow at depth in crystalline rock beneath a moving ice-sheet margin, exemplified by the Fennoscandian Shield, Sweden. *Hydrogeology Journal*, 21(1):239–255, 2013.

[121] P. Pitkänen, A. Luukkonen, and A. Partamies. Buffering against intrusion of groundwater of undesirable composition. In *OECD/NEA Proceedings*, Manchester, United Kingdom, 2007. NEA. NEA No. 6362.

[122] J. Bear, C.-F. Tsang, and G. De Marsily. *Flow and Contaminant Transport in Fractured Rock*. Academic Press Inc., San Diego, CA, 1993.

[123] SKB. Buffer, backfill and closure process report for the safety assessment SR-Site. SKB Technical Report TR-10-47, SKB, 2010.

[124] C.W. Fetter. *Applied Hydrogeology, Second Edition*. Merrill Publishing Company, Columbus, OH, 1988.

[125] M. Stickler and G. Meyerhoff. The spontaneous thermal polymerization of methyl-methacrylate: 5. Experimental study and computer simulation of the high conversion reaction at 130 ^{o}C. *Polymer*, 22(7):928–933, 1981.

[126] J. Lingnau and G. Meyerhoff. The spontaneous polymerization of methyl-methacrylate: 6. Polymerization in solution: participation of transfer agents in the initiation reaction. *Polymer*, 24(11):1473–1478, 1983.

[127] J. Sammaljärvi, L. Jokelainen, J. Ikonen, and M. Siitari-Kauppi. Free radical polymerzation of MMA with thermal initiator in brick and Grimsel granodiorite. *Engineering Geology*, 135-136:52–59, 2012.

[128] S. Ma, G. Song, W. Li, P. Fan, and G. Tang. UV irradiation-initiated MMA polymerization to prepare microcapsules containing phase change paraffin. *Solar Energy Materials and Solar Cells*, 94:1643–1647, 2010.

[129] P. Leblans, D. Vandenbroucke, and P. Willems. Storage phosphor for medical imaging. *Materials*, 4:1034–1086, 2011.

[130] J.D.J. Ingle and S.R. Crouch. *Spectrochemical Analysis*. Prentice Hall, New Jersey, 1988.

[131] L.A. Feldkamp, L.C. Davis, and Kress J.W. Practical cone-beam algorithm. *Journal of the Optical Society of America A*, 1(6):612–619, 1984.

[132] L. J. Pyrak-Nolte, N.G.W. Cook, and D.N. Nolte. Fluid percolation through single fractures. *Geophysical Research Letters*, 15(11):1247–1250, 1988.

[133] S.Y.F. Chu, L.P. Ekström, and R.B. Firestone. The Lund/LBNL nuclear data search. http://nucleardata.nuclear.lu.se/toi/, 1999.

[134] K. Kanaya and S. Okayama. Penetration and energy-loss theory of electrons in solid targets. *Journal of Physics D: Applied Physics*, 5(1):43, 1972.

[135] E. Rädlein, R. Ambos, and G.H. Frischat. Surface analysis of sol-gel coatings on glass by secondary neutral mass spectrometry. *Fresenius' Journal of Analytical Chemistry*, 353:614–618, 1995.

[136] E. Rädlein and G.H. Frischat. Atomic force microscopy as a tool to correlate nanostructure to properties of glasses. *Journal of Non-Crystalline Solids*, 222:69–82, 1997.

[137] Posiva Oy. Olkiluoto site description 2011. Posiva Report 2011-02, Posiva Oy, 2011.

[138] G. Chinga-Carrasco, H. Kauko, M. Myllys, J. Timonen, B. Wang, M. Zhou, and J.O. Fossum. New advances in the 3D characterization of mineral coating layers on paper. *Journal of Microscopy*, 232:212, 2008.

[139] Posiva Oy. Core drilling of REPRO drillholes in ONKALO at Olkiluoto 2010-2011. Posiva Working Report 2012-26, Posiva Oy, 2012.

[140] J. Ikonen, J. Sammaljärvi, M. Siitari-Kauppi, M. Voutilainen, A. Lindberg, J. Kuva, and J. Timonen. Investigation of rock matrix retention properties. Supporting laboratory studies I: Mineralogy, porosity and pore structure. Posiva Working Report 2014-68, Posiva Oy, 2015.

[141] A. Kärki and S. Paulamäki. Petrology of Olkiluoto. Posiva Report 2006-02, Posiva Oy, 2006.

[142] B.A. Younglove. Thermophysical properties of fluids I. Argon, ethylene, parahydrogen, nitrogen, nitrogen trifluoride and oxygen. *Journal of Physical and Chemical Reference Data*, 11:1–356, 1982. Supplement 1.

[143] P. Klobes, M. Siitari-Kauppi, and K.-H. Hellmuth. Porosity characterization of selected nanoporous solids. STUK-YTO-TR 215, STUK, 2006.

[144] T. Kohout, R. Karlqvist, I. Lassila, J. Eskelinen, A. Hortling, L. J. Pesonen, and E. Hæggström. Ultrasonic determination of porosity in homogeneous ceramic samples. *Geophysica*, 49(1-2):25–32, 2013.

[145] H. S. Carslaw and J. C. Jaeger. *Conduction of Heat in Solids*. Clarendon Press, Oxford, 1959.

[146] F. A. L. Dullien. *Porous Media: Fluid Transport and Pore Structure*. Academic Press, San Diego, 1979.

[147] G. Taylor. Dispersion of soluble matter in solvent flowing slowly through a tube. *Proceedings of the Royal Society A: Mathematical, Physical & Engineering Sciences*, 219(1137):186–203, 1953.

[148] K. Hartikainen and J. Hartikainen. Posiva's site investigations in Olkiluoto, Kivetty, Romuvaara and Hästholmen by He-gas methods in 1997. Posiva Working Report 98-17e, Posiva Oy, 1998.

[149] L. J. Klinkenberg. The permeability of porous media to liquids and gases. *Drilling and Production Practice*, pages 200–236, 1941.

[150] W. Kast and C. R. Hohenthanner. Mass transfer within the gas-phase of porous media. *International Journal of Heat and Mass Transfer*, 43:807–823, 2000.

[151] S. M. Clifford and D. Hillel. Knudsen diffusion: The effect of small pore size and low gas pressure on gaseous transport in soil. *Soil Science*, 141(4):289–297, 1986.

[152] J. Autio. Characterization of the excavation disturbance caused by boring of the experimental full scale deposition holes at TVO-research tunnel. Posiva Report A-96-09, Posiva Oy, 1996.

[153] J. Autio, T. Hjerpe, and M. Siitari-Kauppi. The effect of EDZ on the migration of radionuclides in a KBS-3 type repository. In V.M. Oversby and L.O. Werme, editors, *MRS proceedings 807: Scientific Basis for Nuclear Waste Management XXVII*, pages 627–632. MRS, 2004.

[154] J. Maaranen, J. Lehtioksa, and J. Timonen. Determination of porosity, permeability and diffusivity of rock samples from Äspö hrl using the helium gas method. Äspö Hard Rock Laboratory International Progress Report IPR-02-17, Svensk Kärnbränslehantering AB, 2001.

[155] S. Seager, L. Geertson, and J. Giddings. Temperature dependence of gas and vapor diffusion coefficients. *Journal of Chemical and Engineering Data*, 8:168–169, 1963.

[156] J. Sammaljärvi, A. Lindberg, J. Ikonen, M. Voutilainen, M. Siitari-Kauppi, and L. Koskinen. Investigation of mineralogy, porosity and pore structure of Olkiluoto bedrock. In *MRS proceedings 1665: Scientific Basis for Nuclear Waste Management XXVIII*, pages 31–37. MRS, 2014.